Master's thesis

NTNU
Norwegian University of Science and Technology
Faculty of Information Technology and Electrical Engineering
Department of Electric Power Engineering

Mari Lund Øvstebø

The Impact of Offshore Wind Power Variations on Continuous-time Scheduling of a Hydrothermal System

Models and Case Studies

Master's thesis in Energy and Environmental Engineering
Supervisor: Hossein Farahmand
June 2020

NTNU
Norwegian University of Science and Technology

Mari Lund Øvstebø

The Impact of Offshore Wind Power Variations on Continuous-time Scheduling of a Hydrothermal System

Models and Case Studies

Master's thesis in Energy and Environmental Engineering
Supervisor: Hossein Farahmand
June 2020

Norwegian University of Science and Technology
Faculty of Information Technology and Electrical Engineering
Department of Electric Power Engineering

NTNU
Norwegian University of
Science and Technology

Preface

This master thesis contains my final work as a master student at the Department of Electric Power Engineering at the Norwegian University of Science and Technology.

The master thesis builds on the specialization project that I delivered in December 2019 [1], and therefore, Chapter 2, 3 and 4 have been re-used. However, all three chapters have been modified to fit into the master thesis. In Chapter 2, some sections have been added or modified, and figures have been redrawn to provide better explanations. The literature review in Chapter 3 has been updated to provide a better overview of the topic than what was presented in the specialization project. The mathematical formulations of the Unit Commitment (UC) models presented in Chapter 3 and 4 have been re-used, but the explanations have been updated to provide a clearer understanding.

Through the work that is presented, I have been given the opportunity to submit an abstract and a paper to the International Conference on the European Energy Market (EEM) 2020 in Stockholm, Sweden, September 16th to 18th. The abstract was accepted in March 2020, and the full paper was submitted June 15th. Due to the restrictions imposed by SARS-CoV-2, the presentation of the paper will be held on a virtual conference. The submitted paper can be found in Appendix A.

Acknowledgment

My supervisors for both the specialization project and the master thesis have been Associate Professor Hossein Farahmand and PhD candidate Christian Øyn Naversen from NTNU. Their guidance and support have played an essential role in my work with both the specialization project and the master thesis. Hossein has been available for quick questions and meetings, and has encouraged and helped me to submit the abstract and writing the paper for EEM. Christian have been my day-to-day supervisor and has always been available for meetings and questions. The weekly web-meetings with Christian have motivated me to continue working on the thesis during this extraordinary spring. I have to thank him for spending numerous of hours helping me to understand the continuous-time optimization framework, teaching me coding in Python, and finally helping me with writing the paper. A massive thanks goes to both Hossein and Christian. I also have to thank Arild Helseth from SINTEF Energy Research for running the water-value calculations for me and for helping out on the finalization of the paper.

I would also like to thank my parents and my two brothers for supporting me and believing in me through my five years at Energy and Environmental Engineering. Finally, I would like to thank my boyfriend for the support, good discussions, and for being patient with me through these last months of master writing.

Abstract

As a part of the climate policy, a significant amount of offshore wind power is expected to be integrated into the Northern European power system in the coming years. The variable nature of wind power generation challenges the security of the power supply as the flexibility of conventional generators are pushed to their limits. Larger shares of offshore wind power result in more frequent and unpredicted changes in the power flow between connected areas, amplifying the structural imbalances in the system. Hence, large-scale offshore wind power will increase the structural imbalances and the need for balancing reserves. Cascaded hydropower is an existing energy storage technology that can provide energy and flexibility on a system scale. The Nordic power system is dominated by flexible, fast-ramping, and relatively cheap hydropower production. In contrast, a large portion of the generation mix in Central Europe still consists of conventional thermal generation with limited ramping capabilities and higher operating costs. The increasing cross-border capacity between Norway and continental Europe enables the hydropower to help balance the interconnected system when fast variations in demand and generation occur due to the integration of variable and uncertain wind power in the Northern European power system.

The discrete structure of the European day-ahead electricity markets is mainly designed for power systems with low variability in load and generation within the hour. The discrete-time resolution does not fully account for sub-hourly variations, which leads to larger structural imbalances when variable power sources are integrated into the power system. The continuous-time optimization framework directly models such sub-hourly variations by representing all time-varying data and variables as continuous curves, with the resulting optimization problem defined in terms of the coefficients of the chosen base polynomials. This allows for ramping and other inter-temporal constraints to be enforced continuously, resulting in a more realistic representation of the power system operation.

In this thesis, a stylized three-area power system representing parts of Northern Europe is considered. The power system consists of a hydro dominated Norwegian area, a thermal dominated German and Dutch area, and an offshore wind area in the North Sea, connected through High Voltage Direct Current (HVDC) cables. A continuous-time UC formulation is used to model the Northern European system operation. The cost of covering the structural imbalances in the system is quantified by a cost comparison to an analogous discrete-time model for different cases. If the discrete-time unit commitment is implemented for real-time operation, load shedding will be introduced since the demand in periods with high net-load ramping cannot be met. The simulation results demonstrate that the proposed framework reduces system balancing costs and the events of ramping scarcity in real-time balancing of the power system.

Sammendrag

Som en del av klimapolitikken, forventes et betydelig omfang av offshore vindkraft å bli integrert i det nordeuropeiske kraftsystemet de kommende årene. Den varierende og i stor grad uforutsigbare kraftproduksjonen fra offshore vindkraft utfordrer kraftsystemets sikkerhet ettersom egenskapene til de konvensjonelle kraftverkene ikke er tilstrekkelig for å sikre balanse og fleksibilitet i kraftsystemet. Større andeler av offshore vindkraft resulterer i hyppigere endringer i kraftflyten mellom tilkoblede områder i kraftsystemet, og vil forsterker de strukturelle ubalansene i systemet. Dermed vil storskala offshore vindkraft øke de strukturelle ubalansene og behovet for balanserende reserver. Kaskadekoblede vannkraftverk er en eksisterende energilagringsteknologi som kan sørge for energi og fleksibilitet på systemskala. Det nordiske kraftsystemet domineres av fleksibel, regulerbar og relativt billig vannkraftproduksjon. I Sentral-Europa består imidlertid en stor del av kraftproduksjonen fremdeles av produksjon fra konvensjonelle termiske generatorer med begrenset justerbarhet og relativt dyr kraftproduksjon. Den økende overføringskapasiteten mellom Norge og Kontinental-Europa gjør at vannkraft i større grad kan bidra til å balansere det sammenkoblede systemet i møte med raske variasjoner i etterspørsel og produksjon som følge av integrering av variabel og usikker vindkraft i det nordeuropeiske kraftsystemet.

Den diskrete strukturen i de europeiske elektrisitetsmarkedene er designet for kraftsystemer med relativt liten variasjon i etterspørsel og produksjon i løpet av timen. Markedsoppløsningen tar i liten grad hensyn til variasjoner innenfor timen, noe som fører til større strukturelle ubalanser når variable og mer uforutsigbare kraftkilder integreres i kraftsystemet. Den kontinuerlige optimeringsmodellen modellerer direkte slike variasjoner innenfor timen ved å representere alle tidsvarierende variabler og data som kontinuerlige kurver, med det resulterende optimaliseringsproblemet definert i form av koeffisientene til de valgte basispolynomene. Dette gjør at reguleringen og andre intertemporale begrensninger kan håndheves kontinuerlig, noe som resulterer i en mer realistisk representasjon av systemdriften.

I denne oppgaven vurderes et stilisert system bestående av tre områder som representerer deler av Nord-Europa. Systemet inneholder et vannkraftdominert norsk område, et termisk dominert tysk og nederlandsk område og et offshore vindområde i Nordsjøen, sammenkoblet med HVDC kabler. En kontinuerlig unit commitment (UC) formulering brukes til å modellere den nordeuropeiske systemdriften. Kostnaden for å dekke strukturelle ubalanser i systemet blir kvantifisert ved en kostnadssammenligning med en analog diskret UC modell for forskjellige tilfeller. Hvis forpliktelsene fra den diskret UC modellen blir implementert for systemdriften, må belastningsfrakobling innføres ettersom etterspørselen i perioder med store netto lastvariasjoner ikke kan oppfylles. Simuleringsresultatene viser at det foreslåtte kontinuerlige rammeverket reduserer systembalanseringskostnadene og perioder med stor knapphet i balanseringen av kraftsystemet.

Table of Contents

List of Tables

List of Figures

Nomenclature

Sets and indices

$\mathcal{A}$	Areas in the system, index a	
$\mathcal{I}$	Thermal generators, index i	
$\mathcal{J}_m^{d/b/o}$	Reservoirs that discharge/bypass/spill into m, index j	
$\mathcal{K}$	Water value cuts, index k	
$\mathcal{L}$	HVDC cables, index l	
$\mathcal{M}$	Hydropower plants and reservoirs, index m	
$\mathcal{N}_m$	Discharge segments in plant m, index n	
$\mathcal{R}$	Number of time intervals in h, index r	
$\mathcal{T}$	Time intervals, index h	

Parameters

δ_h	Length of time interval	s
$\eta_{m,n}$	Energy conversion factor	MWs/m^3
C^b	Penalty for bypassing water	€/m^3
C^c	Penalty for wind curtailment	€/MW
C^o	Penalty for spilling water	€/m^3
C^s	Penalty for load shedding	€/MW
C_i	Marginal cost of thermal generation	€/MW
$C_i^{start/stop}$	Cost of starting/stopping thermal generators	€

D_k	Water value cut constant	€
F_l^{max}	Maximal flow limit on HVDC cable	MW
$G_i^{min/max}$	Minimal/Maximal thermal unit capacity	MW
$G_{l,a}$	Grid coefficient determining cable flow direction	
$I_m(t)$	Natural inflow into reservoir	m^3/s
$I_m^u(t)$	Natural inflow from creek intakes	m^3/s
$L_a(t)$	Area load	MW
N	Number of time intervals in $\mathcal{T}$	
$P_m^{min/max}$	Minimal/Maximal hydropower capacity	MW
$Q_{m,n}^d$	Maximal flow through discharge segment	m^3/s
Q_m^b	Maximal flow through bypass gate	m^3/s
$R_i^{u/d}$	Ramping limits of running thermal unit	MW/s
V_m	Maximal reservoir capacity	m^3
V_m^0	Initial reservoir volume	m^3
$W_a(t)$	Maximal wind power capacity	MW
$WV_{m,k}$	Water value cut coefficient	€/m^3
Variables		
α	Future expected system cost	€
$\rho_a^c(t)$	Wind curtailment	MW
$\rho_a^s(t)$	Load shedding	MW
$f_l(t)$	Flow on HVDC cable	MW
$g_i(t)$	Generated thermal power	MW
$p_m(t)$	Generated hydropower	MW
$q_m^b(t)$	Flow through bypass gate	m^3/s
$q_m^d(t)$	Flow through turbine	m^3/s
$q_m^{in}(t)$	Total controlled flow into reservoir	m^3/s
$q_m^{net}(t)$	Net flow into reservoir	m^3/s
$q_m^{out}(t)$	Total controlled flow out of reservoir	m^3/s

$q_m^o(t)$	Flow through spill gate	m^3/s
$q_m^{rel}(t)$	Total flow released out of reservoir	m^3/s
$s_a(t)$	Generated wind power	MW
$SD_{i/m}(t)$	Shutdown of thermal/hydro unit	
$SU_{i/m}(t)$	Startup of thermal/hydro unit	
$u_i(t)$	Thermal unit commitment decision	
$v_m(t)$	Reservoir volume	m^3
$w_{m,n}(t)$	Discharge segment commitment decision	
Z	Objective value	€
$z_m(t)$	Hydropower unit commitment decision	

Abbreviations

ES	Energy Storage
EU	The European Union
HVDC	High Voltage Direct Current
IRES	Intermittent Renewable Energy Sources
MILP	Mixed Integer Linear Programming
NSL	North Sea Link
NVE	The Norwegian Water Resources and Energy Directorate
PSH	Pumped Storage Hydropower
RES	Renewable Energy Sources
TSO	Transmission System Operator
UC	Unit Commitment
VRE	Variable Renewable Energy

Chapter 1

Introduction

1.1 Background and Perspective

The European Union (EU) has set the ambitious goal of reducing greenhouse gas emissions by more than 40% within 2030, compared to the 1990 level, and thereby increase the total share of renewable energy to 32% [2]. To achieve this goal, member states must significantly increase the share of Variable Renewable Energy (VRE) in their energy mix within the next decade. This may cause a challenge for the existing power systems, as today's grids and their capacities were established for less or non-variable energy sources, dispatchable power generation, and a predictable peak load [3]. VRE sources such as wind power and solar power are defined as intermittent energy sources, which indicate that these power sources are not continuously available. Therefore, wind power will be defined as an Intermittent Renewable Energy Sources (IRES) in this thesis. In order to reduce and successfully handle the regional differences arising from the integration of IRES, the future electricity grid should not only be flexible but also maintain sufficient back-up capacity. A flexible power system is an essential factor when handling network constraints caused by IRES during peak hours of consumption [3].

In order to achieve EU renewable energy and greenhouse gas emission targets, a significant amount of wind power is expected to be integrated into the European power system in the coming years. The variable nature of wind power generation challenges the security of the power systems as the flexibility of conventional generators are pushed to their limits. This will lead to a need for new flexible technologies. Battery storage is an example of a new flexible technology that has gathered much attention in the field of power system research lately. However, battery storage technology is still in the very early phases of large-scale deployment, so flexibility provided by other technologies are still an essential factor to keep the power system balanced. Cascaded hydropower is an existing flexible energy storage technology that can provide energy and flexibility on a system scale, albeit only in regions with suitable weather and topography. The Nordic countries of Norway, Sweden, and Finland have considerable amounts of hydropower installed in their respective power systems. In recent years, several HVDC cables between Norway and continental Europe

have been constructed, and new interconnectors to Germany and Great Britain are under construction. Hydrothermal coordination in the presence of uncertain wind power generation has been studied in the literature for years, which includes both models with long time horizons [4–7] and short-term studies [8]. These studies conclude that an increase in transmission capacity will enable the use of Norwegian hydropower resources to help balancing the wind power in Continental European power systems at a low cost.

The discrete structure of the European day-ahead electricity markets cannot prevent the occurrence of a mismatch between the market cleared volumes and the net-load variations, hence structural imbalances occur. Structural (or deterministic) imbalances are caused by the lack of coherence between on the one hand continuously varying net-load and, on the other hand, scheduled changes of generation at the hour shifts. These structural imbalances must therefore be balanced in real-time by activating procured reserve capacity. As wind power can vary quickly and unpredictably within the span of a few minutes, the structural imbalances and the need for balancing can be worsened by a high wind power penetration. Continuous-time optimization is a way of formulating the standard unit commitment and economic dispatch problem with continuously varying time-dependent variables and input data. The continuous-time optimization framework was initially formulated for a purely thermal system, in [9]. This method of optimization has since been extended to incorporate energy storage technology in [10], and multi-stage stochastic unit commitment and reserve scheduling models are developed in [11] and [12].

This master thesis continues the work that was done in the specialization project [1], where a discrete-time UC model and a continuous-time UC model were formulated. The mathematical formulations are based on the hydrothermal continuous-time implementation done in [13] and extended to include offshore wind power generation. In the master thesis, these UC models are simulated for different cases. The system cost, offshore wind power utilization, and power flow characteristics for different hydrological states and wind conditions are compared. Moreover, the differences between the discrete-time UC model and the continuous-time UC model are explored.

1.2 Objectives

In this master thesis the main objective is to identify the research question:

> *"How can continuous-time scheduling of a hydrothermal system help balancing offshore wind power variations?"*

In order to answer this research question, the following primary objectives will be presented and discussed in this thesis.

- Present the characteristics of IRES and how the variable nature of wind power generation will challenge the security of the power supply.
- Present the characteristics of thermal and hydropower units, and how these power sources can contribute to a stable power system together with increased interconnection capacity when large-scale IRES are integrated.

- Present the state of the art Unit Commitment and discuss why the current discrete structure of the electricity market can cause problems when large-scale IRES are implemented.
- Present the continuous-time optimization framework and extend the hydrothermal continuous-time implementation in [13] to include offshore wind power generation.
- Evaluate the performance of a continuous-time UC model compared to an analogous discrete-time UC model and quantify the cost of structural imbalances in a three-area test system resembling the Northern European power system by comparing the costs obtained by the two UC models.
- Identify specific periods where the discrete-time UC model overestimates the flexibility of the system.

1.3 Report Outline

The master thesis is divided into eight chapters, where the first chapter is the introduction. In Chapter 2, an overview of a hydrothermal system with integration of offshore wind power is provided. The chapter presents the essential characteristics of offshore wind power, thermal power and hydropower generation. It is also presented how thermal and hydropower generation together with an increased interconnection capacity, can provide a stable power supply when the share of offshore wind power is increased. In the last part of the chapter, methods to reduce structural imbalances that occur due to IRES are presented.

At the beginning of Chapter 3, the state of the art Unit Commitment is presented and discussed. In addition, the fundamentals of a discrete market structure are presented together with a mathematical formulation of a discrete-time UC problem. In Chapter 4, the continuous-time optimization framework is presented and explained. The fundamentals of a continuous-time model and theory on Bernstein polynomials are presented as a foundation for the mathematical formulation of the continuous-time UC model presented in the last part of the chapter.

In Chapter 5, the three-area test system is presented together with simplifications and all input data used for the simulations. Chapter 6 presents the different cases used to compare the discrete-time and the continuous-time UC models.

In Chapter 7, the results of the different cases are shown and discussed for both UC models. The chapter also presents the results when the continuous-time model is used as a simulator for real-time operation of the power system. In the last part of the chapter, the results are summarized and discussed.

Finally, in Chapter 8, the conclusions from the thesis are drawn. In addition, suggestions for future work based on the findings in the thesis are given. Appendix A includes the paper presenting the outcomes of the thesis. The paper is submitted to the European Energy Market (EEM) 2020 conference.

Chapter 2

Hydrothermal System with Integration of Offshore Wind Power

This chapter aims to present the essential characteristics of offshore wind power, thermal power and hydropower generation, and how thermal and hydropower generation together with an increased interconnection capacity, can provide a stable power supply when the share of offshore wind power is increased. In addition, the current installed capacities are presented to provide perspective and a background for the values used in the simulations.

2.1 Today's Power System

In the late 19^{th} and the early 20^{th} century some of the first power systems in Europe were developed. These power systems were not meant to transmit electricity over a long distance and were mostly centralized systems with large fossil-fueled power plants close to the demand centers. As the areas of supply increased in size and capacity, the interconnection capacity was not increased accordingly, meaning that the European countries' power systems were not necessarily well-connected.

At the beginning of the power system development, countries used resources within their borders and transported them over short distances to the power plants. This resulted in a varied composition of power plant technologies among the European countries due to different geographical aspects and regional availability of primary energy resources. For example, the German power system is traditionally built on coal and lignite deposits mined in both the west and east part of Germany. In contrast, Nordic countries have traditionally based their power system on hydropower by taking advantage of their topography. The fossil fuel-fired power plants have shaped the existing Central European power systems [14].

The figure presented in **Fig. 2.1** illustrates the share of both fossil-fueled energy production and hydropower energy production in total national energy production within the European countries in 2016. From the figure it can be seen that the electrical energy pro-

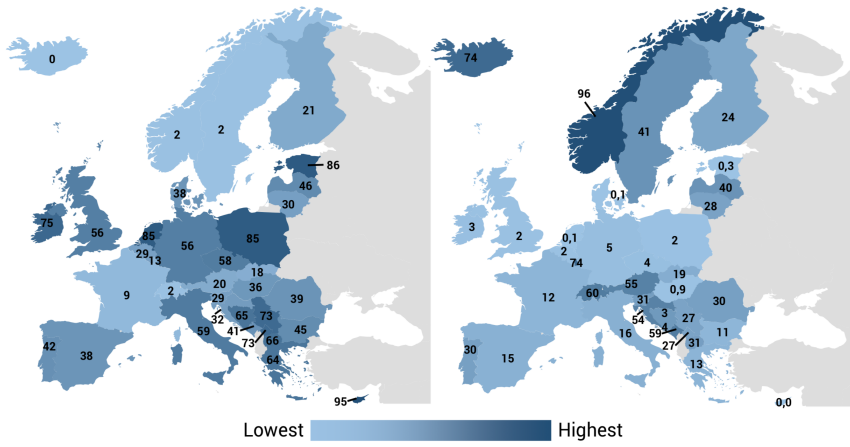

Figure 2.1: Share of fossil-fueled power (left) and hydropower (right) in total national electrical energy production (2016) [14]

duction from fossil fuels still accounts for most of the energy production in Germany and adjacent countries. By 2016, the share was 56% in Germany and 85% in the Netherlands, while in Norway it was 2%. On the other hand, when looking at the electrical energy production from hydropower, the share in Norway is over 95%, while for Germany and the Netherlands the shares are 5% and 0.1%, respectively. When looking at Europe in total, nuclear and fossil-fueled power plants account for around 70% of the total electrical energy production in 2018 [15]. From **Fig. 2.2**, it can be seen that the remaining energy production comes from wind power, hydropower, solar power, and power from biofuels. It is therefore evident that fossil-fueled power plants still play an essential role in the European power system.

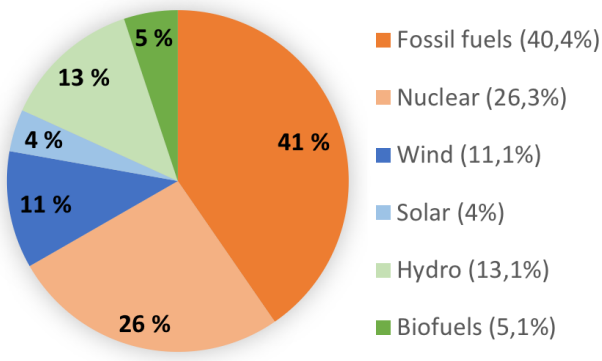

Figure 2.2: Electricity production by source within Europe in 2018 [15]

Although the European countries mostly had individual power systems, cross-boarder transmission lines were established where it was reasonable regionally. Over the years,

European countries built more transmission lines, connecting almost all countries in Continental Europe. Transmission lines between countries are often called interconnectors, and these links were possible to establish since all the different power systems had the same standard frequency of 50 Hz. The frequency is a measure of the balance between the amount of energy that is generated and demanded, where the frequency is an important tool since the power system in itself is not able to store energy in large amounts. When the demand is higher than the generation, the frequency will drop, and vice versa. This will cause imbalance in the power system. Maintaining a continuous balance between generation and load is crucial for the safeguarding of the power system, and therefore flexibility options, such as hydropower plants, are essential. The term flexibility describes the potential to balance production and demand by adjusting the electrical power generation or demand when there is a deviation from the usual amount of energy in the power system [14]. When today's power system was designed, fossil-fueled power and hydropower plants mostly ensured for the electrical power generation. Electrical power output from these power plants is defined as dispatchable, where dispatchable generators can be turned on or off, or adjust their power output to meet the demand. The need for flexibility in the future power system, and how this flexibility can be ensured, will be further discussed later in this chapter.

2.2 Intermittent Renewable Energy Sources

In the past years, the European countries have agreed on limiting global warming by decreasing their environmental emissions. As a result of these agreements, each country has introduced policies to increase the amount of emission-free IRES considerably and strategies on how to integrate them into the power system. IRES are characterized by variable and unpredictable electricity production [16]. In this master thesis, IRES are defined as:

> *"Any source of electrical energy that is not continuously available due to external factors that cannot be controlled, produced by electricity generating sources that vary in their conditions on a fairly short time scales."* [17]

Solar, wind, tidal, and wave power are some of the most known IRES, and the variable nature of these energy sources challenges the security of the power supply [16]. Intermittent renewable generation makes the generation profile more volatile and uncertain because the IRES are not continuously available due to external factors like wind and sun. If there is no wind or sun available, there will be no generation of power. But if there is, IRES has the ability to produce electricity without consuming natural resources and causing greenhouse gas emissions. These reasons are why converting IRES to electricity is more climate friendly than burning fossil fuels and why their share and importance will increase in the future to achieve climate goals.

To make the power system more sustainable and environmentally friendly, many European countries have agreed on laws to prioritise the feed-in of IRES. The electrical power output from IRES will be implemented into the power system first, then other power plants have to follow their lead and adjust their electrical power output. Therefore, IRES power plants mostly operate at their maximum production even though it limits their flexibility [14]. Restrictions that hinder the flexibility, such as minimum production and start-up

time, do not apply for IRES, and therefore, dispatch of IRES are easier than for conventional generators.

In order to efficiently integrate a large share of IRES, the system should be designed with a high degree of flexibility. This can be achieved through a combination of flexible generating units, availability of interconnection capacity, balancing reserves, and flexible back-up capacity [18]. The back-up capacity is normally procured through market based mechanisms, but the Transmission System Operator (TSO) may also dispose back-up reserves. On a yearly basis, additional back-up capacity can essentially be maintained by flexible hydropower or conventional thermal power plants. On a daily basis it will be required that the dynamic management of the power system is able to handle higher ramping rates due to sudden variations in IRES.

In this master thesis, the primary focus is on how flexibility through dispatchable generation, energy storage with the use of hydro reservoirs and increasing interconnection capacity can provide a secure and balanced power system in the future when the share of offshore wind power increases. These types of flexibility will be further discussed in Section 2.3, 2.4 and 2.5, respectively.

2.2.1 Offshore Wind Power Generation

Offshore wind power is one of the most unpredictable and varying IRES, where the production is characterized by variations on all time scales, from seconds to years. This is the main reason why large-scale offshore wind power production will bring significant challenges to the power system operation. The amount of offshore wind power produced will have a significant impact on the scheduling of conventional generators. The unit commitment decision of the conventional units will face uncertainty in absence of a perfect forecast when large amounts of offshore wind power capacity are integrated. The degree of uncertainty the wind power will bring to the power system is dependent on the way the power system operates regarding the leading time between forecast scheduling and consumption. This will indirectly determine the amount of additional balancing reserves required to achieve a stable power system [18].

The power production from a wind turbine depends upon the wind speed. In **Fig. 2.3**, a typical power curve for a pitch regulated wind turbine is shown [19]. The graph shows the electrical power output from the wind turbine at different wind speeds and provides a convenient way to model the performance of a wind turbine. The power curve can be divided into different regions based on the wind speed, shown in **Fig. 2.3**. In the first region, where the wind speed is below a minimum limit, known as the cut-in speed, the power output will be zero. In this region it will be inefficient to operate the turbine, hence the wind turbine will be off. In the second region, the wind speed is between the cut-in speed and the rated speed, and here the power trajectory goes from zero to the turbine rated power output. In the third region, constant rated power output is produced until the cut-off speed is attained. If the wind speed exceeds the cut-off speed, the turbine will be turned off to protect its components. This region is referred to as region four in **Fig. 2.3**, and here the power output is zero. The power curve will be different for each wind turbine, but the shape of the curve will remain similar. An accurate model of the power curves is an important tool for forecasting the electrical power output from wind turbines.

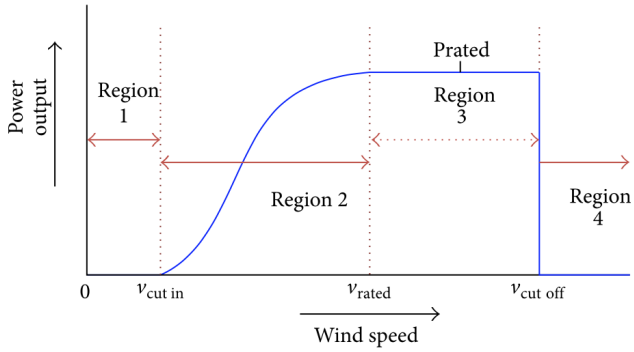

Figure 2.3: Typical power curve of a pitch regulated wind turbine [19].

2.2.2 Offshore Wind Power Developments in the North Sea

By the end of 2019, Europe had a total installed offshore wind power capacity of 22,072 MW. During 2019, 99% of new wind farm installations happened in the North Sea, which now accounts for 77% of all offshore wind power capacity in Europe. The UK has the largest amount of installed offshore wind power capacity in Europe, with 45%. Germany has the second largest amount, with 34%, followed by Denmark (8%), Belgium (7%) and the Netherlands (5%) [20]. The development of offshore wind power in Europe will continue to increase in the future, and the European Commission estimates that the offshore wind power capacity across Europe could reach 450 GW by 2050 [21]. When looking at the North Sea, it is estimated a cumulative installed capacity of 70 GW by 2030, where the dominant markets still will be the UK, with 40 GW, and Germany with 20 GW [22] [23] [24].

A map showing built, in construction, and projected wind farms in the North Sea is presented in **Fig. 2.4** [25]. The development of the world's biggest offshore wind farm at Dogger Bank in the North Sea is now under construction. This wind farm is a project between SSE and Equinor, and when operation begins in 2023, the wind farm generation is projected to cover the electricity demand of around 4.5 million households [26].

The installed capacity for each wind turbine is an essential factor when looking at the increase in offshore wind power capacity. Between 2014 and 2018, the average rated capacity of newly installed wind turbines has increased at an annual rate of 16%, where the average rated capacity of newly installed turbines was 6.8 MW at the end of 2018. The rise in average rated capacity for each wind turbine will affect the wind farm size, and from 2007 to 2018, the average size has grown from 79.6 MW to 561 MW [20].

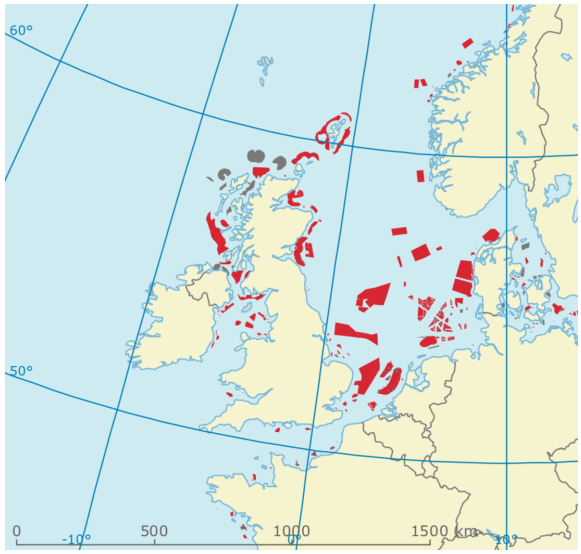

Figure 2.4: Map showing offshore wind farms (built, in construction or projected) in the North Sea [25]

2.3 Thermal Generation

Fossil-fueled and nuclear generators, also called thermal generators, provide dispatchable power, meaning that these generators can be turned on or off, or adjust their power output to meet the demand. Therefore, large-scale thermal power plants are traditionally a primary source of flexibility. The flexibility of thermal power plants is hindered by four characteristics of the generator; the minimum and maximum point of operation, the ramp rate, and the start-up time. These characteristics can vary for each individual power plant, where more recently built power plants often are more dynamic [14]. These characteristics are illustrated in **Fig. 2.5**, where the horizontal axis represents time, and the vertical axis represents the production in percent of maximum capacity, often referred to as the installed capacity of the power plant.

The amount of time the power plant needs to reach a stable point in operation is defined as the start-up time, where the stable point of operation is defined as the minimum production in **Fig. 2.5**. This time is associated with the time the generator elements need to reach a certain operating temperature. Power plants operating at minimum production avoids long start-up phases, which enables them to react quickly to changes in the power system. With a high amount of electrical power generation by IRES in the power system, the option of dispatching thermal generation as low as necessary will provide flexibility to the power system. Therefore, power plants with a low minimum production will be desirable when there are large amounts of IRES in the power system. The ramp rate, illustrated in **Fig. 2.5**, is the rate at which the production level can be adjusted. The ramp rate is often expressed as the potential change in production in proportion to the installed capacity of the power plant. A power plant with a high ramp rate is able to react quickly

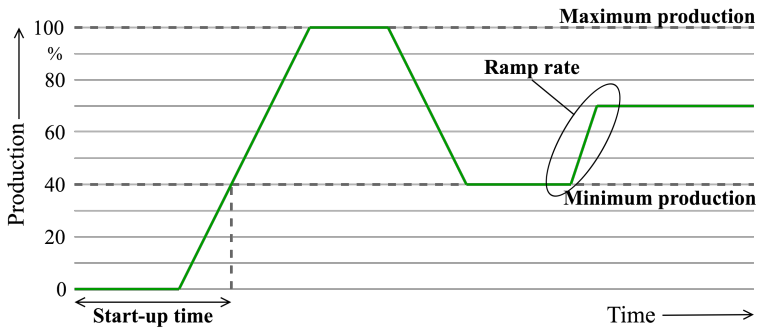

Figure 2.5: Exemplary illustration of characteristics of fossil-fueled and nuclear power plants.

to changes in the power system, hence providing important flexibility when the share of IRES is increased.

The thermal power plants can be divided into three categories; baseload power plants, medium load power plants, and peak load power plants. These categories are based on the different demand categories; base, medium, and peak load, shown in **Fig. 2.6** alongside a generic load curve over a period of 24 hours.

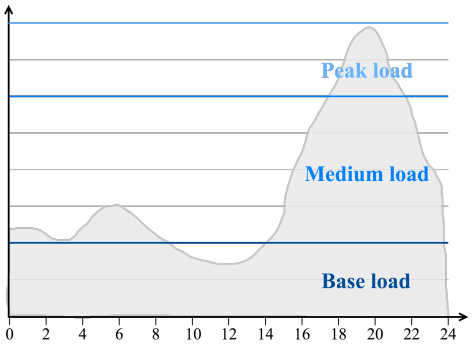

Figure 2.6: Generic load curve expressing the different load categories.

The baseload is defined as a near constant demand over a time period. If demand exceeds this base level, the expression medium load is used. The term peak load is used if the demand levels exceed the medium load within a shorter time period. From **Fig. 2.6**, it can be seen that the peak load occurs during a short time interval and to a lower extent than the baseload and medium load.

The characteristics of the different thermal power plants decide which category they belong to, where the three different categories are described in Section 2.3.1 to 2.3.3. The fossil-fueled power plants that will be discussed in this master thesis are fossil gas, fossil hard coal, and lignite power plants. The characteristics of these power plants, together with nuclear power plants, are summarized in **Tab. 2.1**.

2.3.1 Baseload Power Plants

As explained before, it can take several hours for a power plant to reach a stable point of operation after a shutdown. Lignite power plants require a start-up time of two to six hours [14]. Because of this long start-up phase, lignite power plants often do not entirely disconnect from the power system but operates at minimum production instead. The minimum production level for lignite power plants is about 30 to 50% of installed capacity, and this point of operation limits the flexibility of the lignite power plants [27]. The ramp rate for lignite power plants is between one to four percent per minute when they operate between the minimum and maximum production level [14]. For nuclear power plants, the start-up time varies between three to 50 hours, depending on how long the generator has been off. Because it can take several days for a nuclear power plant to reach a stable point of operation, they are often operating at a production level of 50% or higher, even though the minimum production level is between 20 and 30% of installed capacity. Above this minimum production level, the ramp rate is around 10% of installed capacity per minute [14]. Both lignite and nuclear power plants have high investment costs. On the other hand, the operational costs are often low which makes them cost-effective over a longer period of operation. The lengthy start-up phase and the high minimum production level of the baseload power plants make these generators unsuitable for balancing a power system with a large amount of IRES.

2.3.2 Medium Load Power Plants

Power plants that are designed to cover medium load are similar to the baseload power plants, but they are often able to adjust their production more quickly. Fossil hard coal power plants are one type of power plants that are defined as a medium load power plant. They share many characteristics with lignite power plants, but they are able to adjust their production more efficiently with a shorter start-up phase and a higher ramp rate. After a shutdown, fossil hard coal power plants need two to three hours to reach a stable point of operation. For newly built fossil hard coal power plants, the start-up time can be as short as one hour. Their minimum production level is between 25 and 40% of installed capacity, and they have the possibility to change their production by two to six percent per minute [14]. Therefore, fossil hard coal power plants are better suited to provide flexibility to the power system than baseload power plants.

2.3.3 Peak Load Power Plants

Peak load power plants mainly cover the load under high demand periods, where gas-fired power plants often are best suited. Power plants equipped with a gas turbine are flexible, and has a start-up time around six to 20 minutes. The minimum production is approximately 20 to 50% of installed capacity, and the power plants can change their production with a speed of eight to fifteen percent per minute when operating between the minimum and maximum production [14]. Although fossil gas power plants show a high degree of flexibility, the operating costs are very high, limiting their appeal as a flexibility option.

Characteristic	Nuclear	Lignite	Fossil Hard Coal	Fossil Gas
Ramp rate	10 %/min	1-4 %/min	2-6 %/min	8-15 %/min
Minimum production	20-30 %	30-50 %	25-40 %	20-50 %
Start-up time	3-50 h	2-6 h	1-3 h	6-20 min

Table 2.1: Fossil-fueled and nuclear power plant characteristics [14]

Even though some of the thermal power plants show a high degree of flexibility, they are still not flexible enough to balance short-term variations of IRES. Additionally, European countries will have to decrease the energy production from fossil-fueled power plants to reach their climate goals. Eventually, other options for flexibility have to be integrated into the power system.

2.3.4 The Role of Thermal Power in a Power System with a Large Share of IRES

The behavior of thermal power plants in a power system with a high degree of IRES varies depending on the net-load. The net-load is defined as the actual power demand minus renewable power output, hence the total demand that is left for nonrenewable power plants to cover [28]. This term has been introduced since the electrical energy from IRES must be prioritized in the power system to reach climate goals in most of the European countries. How the thermal power plants will react depends on whether the net-load is increasing or decreasing. When the net-load is decreasing, meaning generation from IRES is increasing, thermal power plants can reduce or shut down their production in order to balance the feed-in from IRES. This requires that there are enough thermal power plants in operation at an adequate level, otherwise it will be necessary to curtail the IRES. On the other hand, when the net-load increases, thermal power plants can ramp up their production to meet the net-load when the electrical power generation from IRES is decreasing [29].

In a power system with a large share of IRES, the base load will be provided by must-run generation from IRES, while thermal power plants will cover the remaining net-load. So in a power system with an increasing degree of electrical power production from IRES, the distinction between baseload, medium load and peak load power plants no longer apply in the same way as before. The overall production from thermal power will decrease as the share of IRES generation increases. This does not automatically mean that the required installed capacity of thermal power decrease by the same amount. With the integration of IRES, the net-load will change more rapidly and more often, so thermal power plants will be required to provide flexible back-up and balancing. Therefore, thermal capacity and availability will remain relevant in the future power system as well [29].

2.4 Hydropower

While thermal power generation might not necessarily provide the required flexibility and balancing capacity, the large hydro reservoirs in Norway are, on the other hand, ideally suited for such balancing [30]. Hydropower has been integrated into the power system for many years, and especially in the Nordics has hydropower been an important source for electricity production. The main advantages of hydropower are that it is renewable, it has close to zero green house gas emissions, it is reliable and it can be a highly flexible energy source since water can be stored in hydro reservoirs until needed [31]. More specifically, the flexibility of hydropower provide advantages such as [32]:

1. Minimizing variations in energy prices during the day and year.
2. Reducing the need for reserve generation in continental Europe.
3. Limiting the seasonal differences in the European load and generation.

Both the variation in energy prices and the need for reserve generation occurs due to uncertainty and variations in intermittent renewable generation. There can be periods when the imbalance between renewable generation and the load is significant, and in some situations, an extensive wind power generation combined with low demand, leads to negative energy prices. In these situations the flexible hydropower production is essential to balance the power system [32].

2.4.1 Norwegian Hydropower Production

Norway has the highest share of hydropower within the power system in Europe, and stands for half of Europe's reservoir capacity with a total reservoir capacity of 82 TWh [33]. Today there are 1660 hydropower plants in Norway, which accounts for 96% of the total installed capacity [34]. The installed capacity of hydropower was 32,257 MW at the beginning of 2019 [35].

The Norwegian Water Resources and Energy Directorate (NVE) measures the water levels in the Norwegian reservoirs each week, and generally, the water levels will be highest in the spring and then decline towards the end of summer. During the autumn, the water levels will again increase, but in the winter months, the water levels are generally low. **Fig. 2.7** shows the minimum, the median and the maximum water level of the Norwegian reservoirs during a year, where the vertical axis is in percent of a 100% full reservoir. The data series used to make the charts are based on measurements from 1993 to 2019, and are found in [33]. When looking at the median value, it is seen that the minimum water level occurs in week 17, while the maximum water level occurs in week 41. The value of the water levels in these weeks are 31.6% and 85.3% of full reservoir capacity, respectively.

More than 75% of the Norwegian production capacity is today flexible, which means that the production can be rapidly regulated up or down at a relatively low cost [34]. Because of the large integration of offshore wind power in the power system, the flexibility of the thermal generators is pushed to their limits. This makes the Norwegian hydropower plants with storage capacity useful to balance the power system.

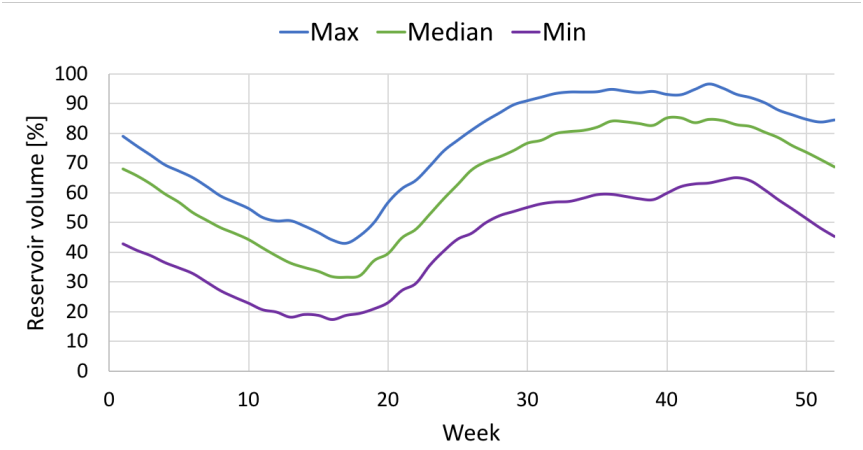

Figure 2.7: Water levels in Norwegian reservoirs during a year [33].

2.4.2 The Role of Hydropower in a Power System with a Large Share of IRES

Large share of offshore wind power will in the future represent a significant challenge to the stability of the transmission system and the security of supply to the consumer. There will be a need for back-up capacity in order to generate power when there is low wind and high demand, and storage capacity when there is high wind and low demand. New Pumped Storage Hydropower (PSH) plants in connection with already existing reservoirs will be a part of the solution of securing a reliable power system.

Storage hydropower is currently the most used storage technology worldwide, with a total installed capacity of over 127 GW [14]. In the storage hydropower plants, water from natural sources can be stored in reservoirs and then released to generate electricity. After the water is used to generate electricity it flows back into the rivers. Water can be stored for days or months, and in the Nordics, the water can even be stored for years. The possibility to store water and then produce electricity when needed, makes the storage hydropower flexible.

PSH will add even more flexibility to storage hydropower. PSH plants consist of at least two water reservoirs; upstream and downstream reservoirs. Then, to produce electricity, water can flow downstream into a turbine. Unlike storage hydropower, the released water from the turbine will flow into the lower reservoir instead of flowing back into the rivers. At a later point, this water can be pumped upwards into the highest reservoir, and then again be used to generate electricity. The PSH plants provide an electricity conversion efficiency rate between 80 and 95%, and can provide their maximum pump power within 75 to 110 seconds, even after a shutdown. While in operation, some highly flexible PSH plants can produce their full amount of power in just a few seconds [14]. The PSH plants uses pumps to transfer water from the lower reservoir to a higher one, and this pump use electricity, so these power plants have the ability to function as both a generation and demand unit. With this in mind, the PSH plants can balance variations on both sides of

the power system. On windy days, surplus power can be used to pump water from low reservoirs to higher reservoirs. This water can be released in days when the demand is high and the wind power is low.

Both storage hydropower and PSH plants require large areas for their reservoirs together with a significant difference in altitude. This means that the hydropower plants cause a large interference with the local nature. The investment costs are also high, so the number of new storage hydropower and PSH plants will not be significant in the upcoming years. Instead, upgrading already existing storage hydropower to PSH or installing more capacity in existing power plants may be an option to provide more flexibility without additionally interfering with nature. Including these storage possibilities into the European power system could allow for balancing electrical power generation from wind power in the Northern European countries [14]. In order to use hydropower reservoirs as back-up capacity and storage capacity, more transmission capacity between the European countries must be developed. This will be further discussed in **Sec. 2.5**.

2.5 Interconnection Capacity

The flexibility in the power system is dependent on the number of interconnectors and the interconnection capacity available for power exchange between countries. A large interconnection capacity will result in a more flexible power system. Interconnection between countries and their respective power systems will ensure energy trading and the opportunity to import energy from a system with a lower marginal cost of production. The marginal cost of production affects the power prices within each country, and in turn the amount of power flow between each country. Countries will have the opportunity to make agreements on reserve sharing, where the provision of emergency support can be shared, minimizing the spare capacity that each country has to maintain [36]. Another benefit of interconnections between countries is the opportunity to import green energy. Consequently, this decreases hydro energy spillage and renewable sources curtailment that cannot be used locally, and improves the energy mix of the importing country [16].

2.5.1 Interconnectors Between European Countries

Offshore wind power plants are often located far from load centers, which represents a challenge for the future power system because it will be necessary to transport electricity over long distances. The increase in offshore wind farm development in Europe will require a higher level of cooperation between the European countries and their respective TSO. An example of an on-going international cooperation is the North Seas Countries' Offshore Grid Initiative (NSCOGI) [37]. This cooperation is between 10 European countries where the main objective is to develop an offshore electricity grid in the North Sea area that enables efficient and economic use of the wind energy resources. This initiative will require massive investments and a complex coordinated planning phase, where the transmission networks for all the North Sea states have to be expanded both onshore and offshore [38]. The figures presented in **Fig. 2.8** shows an estimate of how the European integrated power system will expand from 2020 to 2050 [39]. The dark blue areas and lines in both **Fig. 2.8a** and **Fig. 2.8b** shows the wind energy production areas. It can

be seen that the transmission network around the North Sea region is expected to expand significantly, both onshore and offshore, in the next decades.

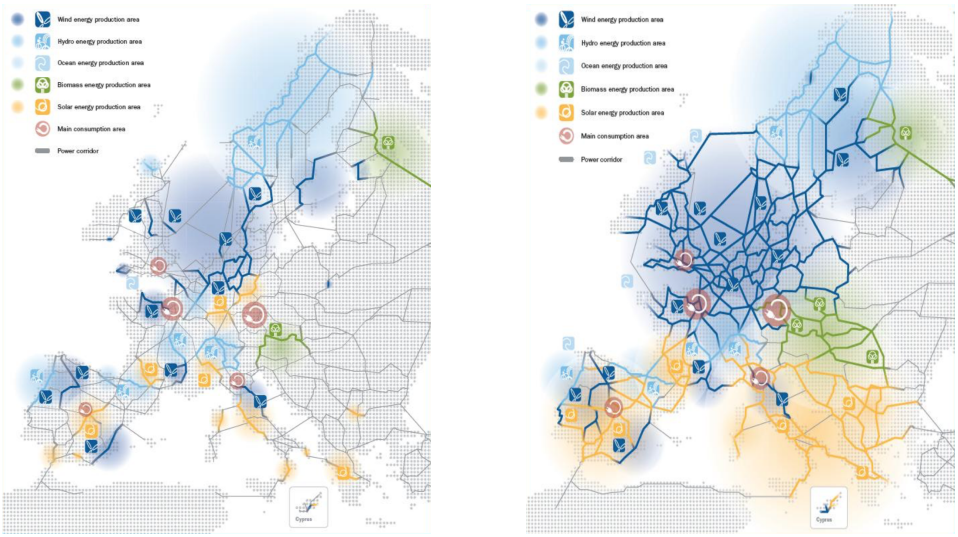

(a) Integrated Grid 2020 **(b)** Integrated Grid 2050

Figure 2.8: The European Integrated Grid for both 2020 and 2050 [39].

Today, two interconnectors connect the Norwegian power system to the rest of the European power system. Skagerrak is a HVDC submarine cable interconnecting Norway and Denmark. The interconnector has a total capacity of 1700 MW and contributes to increased availability of renewable energy [40]. The second interconnector is called NorNed, and is a 580 km long HVDC submarine cable, with a total capacity of 700 MW, that connects the hydropower based Norwegian power grid with the fossil-fueled system in the Netherlands [41]. In the next years, two new interconnectors will be installed, connecting the Norwegian power system to a larger part of Europe. During 2020, the Nordlink cable will be installed between Norway and Germany. This interconnector will be the first direct connection between the Norwegian and German electricity grids. The interconnector will be 623 km long and have an installed capacity of 1400 MW [42]. The second interconnector that is under construction is the North Sea Link (NSL). The NSL, with an installed capacity of 1400 MW, will link the Norwegian and British markets and is expected to be completed in 2021 [43].

2.5.2 Ramping of Power Flow in HVDC Cables

The TSO is imposing ramping restrictions on HVDC cables to ensure security of supply. Frequent large changes in generation and power flow in the grid will make it more difficult to control the frequency of the system, which is an important tool to control the security. Without an upper limit on the ramping of power flow on the HVDC cables, very large ancillary services and operational reserves would be needed to counteract imbalances within

operating hours. Today this ramping restrictions are sat to 600 MW, which implies that power flow on all HVDC cables cannot be changed by more than 600 MW from one hour to another [44]. The power flow on the interconnectors are normally ramped up or down during a 20 minute period around the hour shifts [45].

2.6 Structural Imbalances

Structural imbalances are caused by a mismatch between the continuously varying demand and the scheduled production [45]. Today, the Nordic power market is designed based on an hourly time resolution, meaning changes in the production and power flow happen in the hour shifts. Meanwhile, changes in consumption happen continuously, which will result in structural imbalances. There are several reasons why structural imbalances occur. One reason is the outage of generation units because of unforeseeable failures in the power plants, which results in a deviation between the scheduled production and the actual production. Other reasons for imbalance between demand and production are forecasting errors and load fluctuations. The demand side of the power system has always been volatile because it consists of a large amount of differing components, e.g., multitudes of small households. Outage of generation units and load fluctuations do not need to be within gigawatts to disturb the power system, even minor outage can cause a deviation in frequency outside the normal operating band of 49.9-50.1 Hz [14] [46].

2.6.1 How to Decrease Structural Imbalances

Structural imbalances have been an increasing problem in the European power system as larger shares of IRES have been integrated. To maintain a secure and stable system, the TSO must facilitate for more balancing reserves, flexible consumption and storage capacity. Balancing reserves are power production that can be ramped up or down quickly. So with an increasing amount of structural imbalances, the Norwegian hydropower production will be even more essential to function as a balancing reserve.

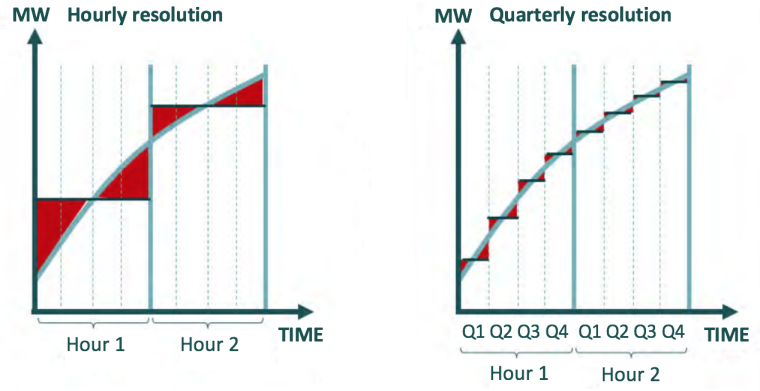

Figure 2.9: Structural imbalance with different time resolutions in the market design [47].

The need for balancing reserves to prevent structural imbalances in the power system is linked to the market design and the time resolution. One approach to reduce structural imbalances within the operating hour is to use smaller time resolutions, meaning that changes in production and power flow can happen more often than just in the hour shifts [46]. This will reduce the structural imbalances in the planning phase and consequently reduce the need for balancing reserves in the operational phase. A quarterly resolution is already a part of the market design in some continental European countries, and will be implemented within the Nordic markets in the upcoming years.

Fig. 2.9 shows the reduction in structural imbalances in the planning phase due to a finer time resolution. In both figures, the black and piece-wise constant curve represents the day-ahead scheduled consumption and thereby production. The light blue and continuous curve represents the actual consumption. The difference between the black and the light blue curves will be the structural imbalance, and are shown as red areas in the figures. It can be seen that the red area is relatively large in the figure representing an hourly resolution, compared to the figure representing a quarterly resolution.

The method of using finer time resolution in the market design shows that the structural imbalances decrease. Hence the need for balancing reserves decreases. With this in mind, a continuous-time representation of the market design will be investigated in this master thesis, where changes in the scheduling of demand and production will happen continuously within each hour. The continuous-time framework will be further discussed in Chapter 4, and a mathematical representation of a continuous-time UC model is presented in Section 4.4.

Chapter 3

Unit Commitment

Unit Commitment (UC) models are of great interest for power grid operation scheduling. This chapter presents the state of the art unit commitment, where both research on the current discrete structure and the continuous-time structure are presented. In addition, the fundamentals of the discrete-time optimization framework is explained together with a mathematical formulation of a discrete-time UC model for a three-area test system.

3.1 State of the Art Unit Commitment

UC formulations have been an important area of research over the last years due to their practical importance in power grid operation. Optimization techniques are used to determine an operating schedule which specifies generators commitment and corresponding production level to meet forecasted load at a minimum operating cost. The UC problem is a non-linear, mathematical problem that consists of several operational constraints, e.g., power balance, maximum and minimum power generation, and ramping limits constraints. The UC model is often formulated as a Mixed Integer Linear Programming (MILP) problem with a set of real variables and binary variables. The binary variables determine the commitment of the generators, and it is typically an aim to minimize the number of binary variables in order to reduce computational time and costs. The MILP problem can be solved with the use of commercial branch-and-cut engines such as CPLEX and Gurobi [48].

The discrete structure of the Nordic hourly day-ahead electricity markets is designed for power systems with low variability in load and generation within the hour. Unit commitment problems based on the discrete structure has been studied for different types of systems. In the recent years, the importance of studying hydrothermal systems with integration of variable power sources has increased due to the penetration of IRES in the energy mix.

A unit commitment model that coordinates hydro and thermal power generation to support secure and economical wind power integration has been proposed in [49]. The paper identifies and considers several reserves in the UC model to counteract the inherent

variability and uncertainty of wind power. It was seen that hydro capacity reserve properly dealt with the uncertainty in wind power generation by ensuring sufficient system power under dry seasons and preventing spillage under wet seasons. The proposed UC model was simulated on an actual large-scale power system in China, and the results showed that the UC model guaranteed for sufficient power generation under peak load demand while maintaining a high utilization rate of the generators in operation. The proposed model in [50] presents a security-constrained UC algorithm, where the effects of intermittency and volatility of wind power generation are discussed. It was seen that the physical limitations of generation units, such as ramping, are crucial for accommodating the volatility of wind power generation. Current electricity markets cannot fully counteract the essential characteristics of non-dispatchable generation sources, like unpredictability and variability of production. This will result in problems for the future power system when large shares of IRES are integrated. This problem is addressed in [51], where a day-ahead UC model with stochastic security is formulated to be able to counteract for the non-dispatchable and variable nature of IRES.

Several UC models have been designed to better incorporate the effects of high penetration of IRES and ramping constraints in the day-ahead generation scheduling. Continuous-time optimization is a way of formulating the standard UC and economic dispatch problem with continuously varying time-dependent variables and input data. The continuous-time optimization framework was initially formulated for a purely thermal system in [9]. Here the problem of the increasing shortage of ramping resources in the real-time operation of power systems were examined by looking at the way the day-ahead UC problem represent load, generation and ramping constraints. It was seen that the current practice could be presented by approximating the load, generation and ramping trajectories with linear splines. Then the paper presents a new way of formulating the day-ahead UC problem, a continuous-time UC problem, by the use of cubic splines to represent the load, generation and ramping constraints. It was seen that this representation provided a feasible schedule and increased the accuracy of the scheduled forecast by capturing sub-hourly variations in the real-time load. Numerical results showed that the continuous-time UC model reduced the total day-ahead and real-time cost of operation by reducing the number of ramping scarcity events in the real-time operation of the power system.

The continuous-time framework has since been extended to incorporate Energy Storage (ES) technologies. This has been done in [10], where a continuous-time scheduling and marginal pricing of energy generation and storage in the day-ahead power systems operation is proposed. The solution captures the ES devices ultimate flexibility to supply the continuous-time load variations. The integration of ES in the power system would reduce the operation costs as well as ramping and number of startups and shutdowns of the generating units. In addition, the need for committing expensive peak load units in the system is eliminated.

In [12], a stochastic optimization model is proposed to optimize the energy and flexibility reserve in day-ahead power system operation. Bernstein polynomials are used to model the day-ahead trajectories, day-ahead flexibility reserve capacity trajectories and the real-time flexibility reserve deployment trajectories. The degree of the polynomials are chosen based on the variability of the load and the renewable power generation in both day-ahead and real-time operation. Generation from solar power was used in this paper

to examine the effects of Renewable Energy Sources (RES). It was observed from the numerical results that the proposed model scheduled generation and reserve capacity more accurately meet the real-time energy and ramping requirements of the real-time net-load. In addition, the total operation cost of the system was reduced.

Cascaded hydropower is an existing flexible energy storage technology which can provide flexibility to the power system. In [13], the continuous-time framework was adapted to model flexible hydropower resources interacting with slow-ramping thermal generators to minimize the cost of the system operation. The formulation of the cascaded hydropower constraints in the continuous-time framework differs from the standard hydropower constraints used in the discrete-time model. The presented paper derived these new constraints, and it was seen that the linarization of the hydropower production curve require integer variables to ensure correct uploading of the discharge segments. In addition, to model the forbidden production zone of the hydropower units, it was required to relax the continuity constraints applied in the continuous-time model.

The above-mentioned research has made a significant contribution to efficiently solving UC models with the use of the continuous-time framework. However, these studies did not consider hydrothermal coordination when offshore wind power is integrated into the continuous-time framework. This will be investigated in this thesis, where the continuous-time UC model for the three-area system will be further explained in Chapter 4, and then be compared to the discrete-time UC model through a three-area test system in Chapter 7.

3.2 Binary UC Variables

The discrete structure of the UC problem is based on hourly intervals where startups, shutdowns and commitment status of the generators are decided in the hour shifts. Startups, shutdowns and the commitment status are all defined as binary variables in the UC models, but their meanings vary between the discrete-time UC model and the continuous-time UC model. **Fig.3.1** is used to describe the meaning of these binary variables, where $u_i(t)$ is the commitment status of generator i at time t, and $SU_i(t)$ and $SD_i(t)$ denotes a startup and a shutdown of generator i, respectively.

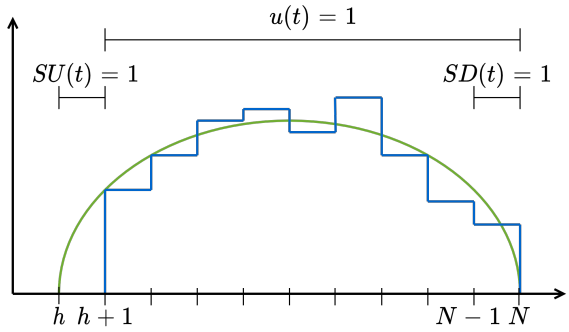

Figure 3.1: Binary UC variables

The discrete-time generating curve, presented as a blue curve in the figure, is piece-

wise constant within each time interval h. The discrete-time model does not contain any continuity constraints, so when there is a startup of generator i in time interval h, a production level of minimum production or higher is obtained from the start of the time interval $h+1$. The same holds if there is a shutdown, $SD(t) = 1$, in hour h, where the production level will be zero at the beginning of time interval $h+1$. In the continuous-time UC model, continuity constraints are required to obtain a continuous-time generation curve, presented as a green curve in **Fig. 3.1**. In this model, $SU_i(t)$ and $SD_i(t)$ initiate startup and shutdown intervals, where the generation will increase to a production level of minimum production or higher if there is a startup, or decrease to a production level of zero if there is a shutdown continuously throughout time interval h.

3.3 Fundamentals of a Discrete-time Optimization Framework

The traditional day-ahead UC problem, in this thesis referred to as a discrete-time UC problem, models the load forecast as a piece-wise constant curve, often with an hourly time resolution. This UC problem schedules the commitment of the generators and corresponding production level on an hourly basis to meet the forecasted load, where the goal is to minimize the total costs of the system.

The discrete structure, today used in the Nordic hourly day-ahead electricity markets, is designed for power systems with low variability in load and generation within the hour. The discrete-time resolution of the market does not take into account sub-hourly variations, which leads to larger structural imbalances when variable power sources are integrated into the power system. This problem can be improved by reducing the step size of the time intervals used in the discrete-time optimization framework sufficiently, or ideally, to use a continuous-time UC formulation. This approach will improve the accuracy of the UC model, but there will also be some limitations. Using smaller time-steps for the scheduling intervals will increase the number of UC decision variables exponentially which will lead to higher computational time [52].

3.4 Mathematical Formulation of the Discrete-time UC Model

A mathematical formulation of the discrete-time UC model for the three-area test system is presented below. The constraints and the objective function are based on the model presented in [13], but is extended to include offshore wind power and reformulated to a discrete-time structure. The discrete-time model will be formulated with the use of six binary variables; $u_i(t)$, $z_m(t)$, $SU_i(t)$, $SD_i(t)$, $SU_m(t)$ and $SD_m(t)$. The first two binary variables describes the commitment status of a thermal unit and a hydropower plant respectively, while the four last describes startup and shutdown of a thermal unit and a hydropower plant. The commitment of the generators can only be decided in the hour shifts, hence startups and shutdowns of generators will only occur in between hours. Even though the commitment of the units only can be decided in the hour shifts, the generators

will have the possibility to change their production each quarter. The same holds for the power flow on the cables. For an explanation of all symbols used in the mathematical formulation, the reader is referred to the nomenclature shown at the beginning of the thesis.

Objective function

The objective function of the proposed model is presented in (3.1), where the goal is to minimize the total cost of the system. The total cost of the system includes the future cost of the hydro system, the penalty of wind power curtailment and load shedding, the cost of spilling and bypassing water, and the operational, start and stop costs for the thermal generators. It is assumed that start and stop costs of the hydropower plants and the operational cost of the wind power plant are negligible.

$$Z = \alpha + \int_0^{t^{end}} \Big(C^c \rho^c(t) + C^s \rho^s(t) \Big) dt + \sum_{m \in \mathcal{M}} \int_0^{t^{end}} \Big(C^b q_m^b(t) + C^o q_m^o(t) \Big) dt + \sum_{i \in \mathcal{I}} \int_0^{t^{end}} C_i g_i(t) dt + \sum_{i \in \mathcal{I}} \sum_{h \in \mathcal{T}} \Big(C_i^{start} SU_{i,h} + C_i^{stop} SD_{i,h} \Big) \tag{3.1}$$

By dividing the time horizon into h intervals of length δ_h, the integrals in (3.1) can be simplified to sums. In the discrete-time model a quarterly resolution will be used, hence the length of one time interval will be $\delta_h = \frac{1}{4}$.

$$Z = \alpha + \sum_{h \in \mathcal{T}} \sum_{r \in \mathcal{R}} \delta_h \Big(C^c \rho_{h,r}^c + C^s \rho_{h,r}^s \Big) + \sum_{m \in \mathcal{M}} \sum_{h \in \mathcal{T}} \sum_{r \in \mathcal{R}} \delta_h \Big(C^b q_{m,h,r}^b + C^o q_{m,h,r}^o \Big) + \sum_{i \in \mathcal{I}} \sum_{h \in \mathcal{T}} \Big(\Big(\sum_{r \in \mathcal{R}} \delta_h C_i g_{i,h,r} \Big) + C_i^{start} SU_{i,h} + C_i^{stop} SD_{i,h} \Big) \tag{3.2}$$

Thermal generation constraints

The constraints describing the thermal generation are presented in (3.3) to (3.6), and are formulated with the use of the binary commitment variable $u_i(t)$. The constraint given in (3.3) describes the power output of the given thermal generator i. If the commitment variable is zero, the power output will be forced to zero, but if the commitment variable is one, the power output will vary between the minimum and the maximum production limit. Constraint (3.4) and (3.5) ensures correct commitment of the generators. (3.5) ensures that there can only be a startup or shutdown for each hour. (3.4) ensures that if there is a startup in the given hour h, the commitment variable for the next hour $h+1$ must be one. If there is a shutdown in the given hour h, the commitment variable for hour h must be one. This means that the commitment variable of the given thermal unit must be one in hour h if there is going to be a shutdown in the next hour $h+1$, and the commitment variable must be zero in hour h if there is going to be a startup in the next hour $h+1$. The number of startups and shutdowns for each thermal generator is used in the objective function to calculate the total costs for starting and stopping thermal generators.

$$u_{i,h}G_i^{min} \leq g_{i,h,r} \leq G_i^{max}u_{i,h} \qquad \forall i,h,r \in \mathcal{I},\mathcal{T},\mathcal{R} \tag{3.3}$$
$$SU_{i,h} - SD_{i,h} = u_{i,h+1} - u_{i,h} \qquad \forall i,h \in \mathcal{I},\mathcal{T} \tag{3.4}$$
$$SU_{i,h} + SD_{i,h} \leq 1 \qquad \forall i,h \in \mathcal{I},\mathcal{T} \tag{3.5}$$
$$SU_{i,h}, SD_{i,h} \in \{0,1\} \qquad \forall i,h \in \mathcal{I},\mathcal{T} \tag{3.6}$$

Thermal generators can be slow to change their output power and therefore constraints for maximum, (3.7), and minimum, (3.8), ramping limits are added to the UC problem. These limits restrict the change in power production between each time interval. Change in power production when there is a shutdown or a startup is also accounted for in these constraints with the use of the binary variables $SU_{i,h}$ and $SD_{i,h}$. If $SD_{i,h}$ or $SU_{i,h}$ is one, the thermal generator will have the opportunity to change its production from G_i^{max} to zero, or from zero to G_i^{max}, in hour h.

$$(g_{i,h,r+1} - g_{i,h,r}) \leq R_i^u\delta_h + (G_i^{max} - R_i^u\delta_h)SU_{i,h} \qquad \forall i,h,r \in \mathcal{I},\mathcal{T},\mathcal{R} \tag{3.7}$$
$$(g_{i,h,r+1} - g_{i,h,r}) \geq -(R_i^d\delta_h + (G_i^{max} - R_i^d\delta_h)SD_{i,h}) \qquad \forall i,h,r \in \mathcal{I},\mathcal{T},\mathcal{R} \tag{3.8}$$

Reservoir volume constraints

It is important to keep the reservoir volume within its limits during the time horizon of the model. The reservoir volume constraints, (3.9) to (3.11), ensure this. The first constraint sets the initial volume of each reservoir m, at the beginning of the time horizon, equal to a value V_m^0. The second constraint calculates the change in volume between two time intervals by taking into account the net inflow into the reservoir at the given time interval. The last constraint ensures that the total volume in the given reservoir is between an upper and lower limit for the given time interval.

$$v_{m,0,0} = V_m^0 \qquad \forall m \in \mathcal{M} \tag{3.9}$$
$$v_{m,h,r+1} = v_{m,h,r} + \delta_h q_{m,h,r}^{net} \qquad \forall m,h,r \in \mathcal{M},\mathcal{T},\mathcal{R} \tag{3.10}$$
$$0 \leq v_{m,h,r} + \delta_h q_{m,h,r}^{net} \leq V_m \qquad \forall m,h,r \in \mathcal{M},\mathcal{T},\mathcal{R} \tag{3.11}$$

Future cost bounds

$$\alpha > \sum_{m \in \mathcal{M}} WV_{m,k}v_{m,N+1} + D_k \qquad \forall k \in \mathcal{K} \tag{3.12}$$

The future expected operating cost of the hydro system is presented in (3.12). The cost is constrained by a set of Benders cuts, here called water value cuts D_k. These cuts are created by looking at a long-term hydrothermal model, which has been done in [53]. The cuts are dependent on the value of the water in each reservoir at the end of the last time interval N. In the proposed model, the same constraint as in [53] is used, but the water value cut coefficients and the water value cuts are created by looking at a long-term hydrothermal model with integration of offshore wind power. Constraint (3.12) calculates the future expected cost, which is directly added to the objective function in (3.2).

Hydropower topology constraints

The best way to utilize the available power in a waterway is to use a setup referred to as a cascaded hydro system. In this configuration, several hydropower plants are built on the same river, and the cascaded topology constraints impose how water flows between the reservoirs. A simple illustration of a cascaded hydro system is presented in **Fig. 3.2**, where m denotes the hydropower plant and $I_m(t)$ is the total inflow to each reservoir. The figure is based on an illustration in [49].

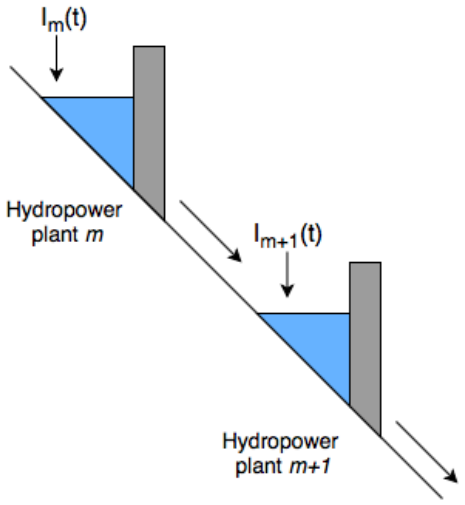

Figure 3.2: Simple illustration of a cascaded hydro system

There are three main waterways that connect two reservoirs: the spill gate, the bypass gate, and the discharge through the turbine. Water that flows through the spill gate goes directly from one reservoir to another reservoir. This occurs when the volume of the upper reservoir has exceeded the maximum capacity. Water that goes through the bypass gate flows from the tunnel between the reservoir and the turbine directly to the next reservoir without being used for power production. The discharged water from a turbine has already been used to produce power, and will then flow into the next reservoir. These waterways, together with the regulated and unregulated natural inflow, are presented in **Fig. 3.3**. The layout of the figure is inspired by a figure in [13]. A presentation of the total cascaded hydro system used in the three-area test system, with the three waterways connecting two reservoirs, can be found in Appendix B. The hydropower topology constraints are presented in (3.13) to (3.19).

The first constraint describes the net inflow into the given reservoir m, where the net inflow is dependent on the natural inflow and the total controlled flow into and out of the reservoir. The second and third constraint describe the total controlled flow into and out of the reservoir respectively. The controlled flow out of the reservoir is dependent on the total flow released from the reservoir, expressed in (3.16), and the flow through the spill gate. The total controlled flow into the reservoir is the sum of water that is discharged from overlaying turbines, water that has passed through the bypass gates and the water that has

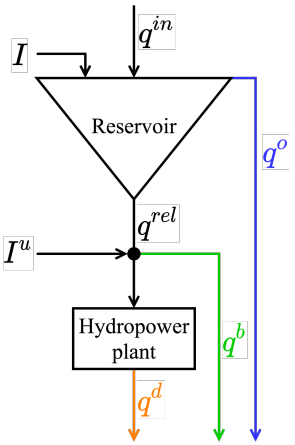

Figure 3.3: Waterways and natural inflow

passed through the spill gates. The constraints presented in (3.17) to (3.19) sets an upper and lower limitation on the water flows.

$$q^{net}_{m,h,r} = I_{m,h,r} + q^{in}_{m,h,r} - q^{out}_{m,h,r} \qquad \forall m,h,r \in \mathcal{M},\mathcal{T},\mathcal{R} \quad (3.13)$$

$$q^{out}_{m,h,r} = q^{rel}_{m,h,r} + q^{o}_{m,h,r} \qquad \forall m,h,r \in \mathcal{M},\mathcal{T},\mathcal{R} \quad (3.14)$$

$$q^{in}_{m,h,r} = \sum_{j \in \mathcal{J}^{d}_{m}} q^{d}_{j,h,r} + \sum_{j \in \mathcal{J}^{b}_{m}} q^{b}_{j,h,r} + \sum_{j \in \mathcal{J}^{o}_{m}} q^{o}_{j,h,r} \qquad \forall m,h,r \in \mathcal{M},\mathcal{T},\mathcal{R} \quad (3.15)$$

$$q^{rel}_{m,h,r} = q^{d}_{m,h,r} + q^{b}_{m,h,r} - I^{u}_{m,h,r} \qquad \forall m,h,r \in \mathcal{M},\mathcal{T},\mathcal{R} \quad (3.16)$$

$$0 \leq q^{d}_{m,h,r} \leq Q^{d}_{m} \qquad \forall m,h,r \in \mathcal{M},\mathcal{T},\mathcal{R} \quad (3.17)$$

$$0 \leq q^{b}_{m,h,r} \leq Q^{b}_{m} \qquad \forall m,h,r \in \mathcal{M},\mathcal{T},\mathcal{R} \quad (3.18)$$

$$0 \leq q^{rel}_{m,h,r} \qquad \forall m,h,r \in \mathcal{M},\mathcal{T},\mathcal{R} \quad (3.19)$$

Hydropower production

When water flows through the turbine, power will be generated. The conversion from discharge through the turbine to generated power is a non-linear function that depends on the plant head and the efficiency curves of the generator and turbine. In this model, it is assumed that this non-linear function is a piece-wise linear curve, where the discharge variable is divided into $n \in \mathcal{N}_m$ segments with a constant efficiency η_n. This simplification is presented in **Fig. 3.4**, where the blue line is the piece-wise linear curve and η_n will be the slope of the curve for discharge segment n.

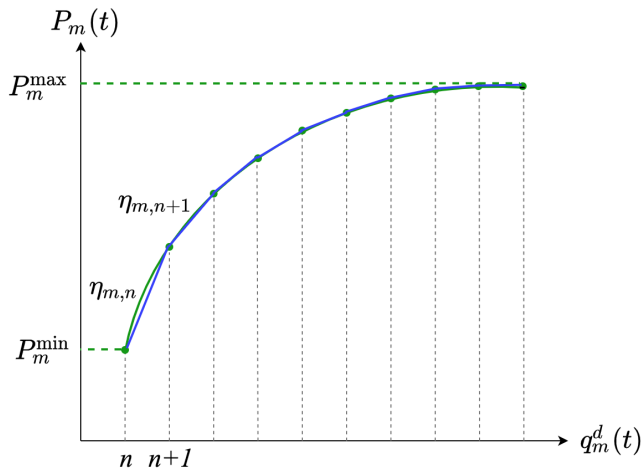

Figure 3.4: Generated hydropower versus discharge through turbine for hydropower plant m

For the discrete-time model, it can be assumed that the discharge segments will be uploaded in the correct order if η_n decreases for each segment. Hence, the segment with the highest η_n will be uploaded first. For the simplified model presented here, this will be fulfilled as **Fig. 3.4** shows that $\eta_{m,n+1} \leq \eta_{m,n}$ for each discharge segment n. The constraints for hydropower production can then be expressed as in (3.20) and (3.21).

$$q^d_{m,h,r} = \sum_{n \in \mathcal{N}_m} q^d_{m,n,h,r} \qquad \forall m, h, r \in \mathcal{M}, \mathcal{T}, \mathcal{R} \tag{3.20}$$

$$p_{m,h,r} = \sum_{n \in \mathcal{N}_m} \eta_{m,n} q^d_{m,n,h,r} \qquad \forall m, h, r \in \mathcal{M}, \mathcal{T}, \mathcal{R} \tag{3.21}$$

Hydropower generation constraints

Hydropower turbines have a forbidden production region between 0 and P_m^{min}. The generation constraints ensure that the hydropower production will be outside of this region with the use of a binary commitment variable $z_m(t)$. The constraint presented in (3.22) limits the hydropower production within an upper and lower limit when the hydropower plant is on, hence the commitment variable is one. When the commitment variable is zero, the hydropower production will be forced to zero. As for the thermal generation constraints, the constraints in (3.23) and (3.24) ensure correct startups and shutdowns of the hydropower plants in each hour shift. Hydropower plants can change their production rapidly, therefore, a ramping constraint for the hydropower production is not included in this model.

$$P_m^{min} z_{m,h} \leq p_{m,h,r} \leq P_m^{max} z_{m,h} \qquad \forall m,h,r \in \mathcal{M},\mathcal{T},\mathcal{R} \tag{3.22}$$
$$SU_{m,h} - SD_{m,h} = z_{m,h+1} - z_{m,h} \qquad \forall m,h \in \mathcal{M},\mathcal{T} \tag{3.23}$$
$$SU_{m,h} - SD_{m,h} \leq 1 \qquad \forall m,h \in \mathcal{M},\mathcal{T} \tag{3.24}$$
$$z_{m,h}, SU_{m,h}, SD_{m,h} \in \{0,1\} \qquad \forall m,h \in \mathcal{M},\mathcal{T} \tag{3.25}$$

Wind power generation and curtailment

The constraint in (3.26) limits the offshore wind power production within an upper and lower limit. The upper limit is a discrete wind series curve, $W_a(t)$, which is the maximal wind power that can be produced for each time interval. Wind curtailment is defined as the difference between the maximum wind power that the wind farm is capable of producing and the actual produced wind power. The wind curtailment is defined in constraint (3.27). The utilization of offshore wind power is maximized if the produced wind power, $s_a(t)$, is equal to the wind series, $W_a(t)$, for each time step during the scheduling period. The amount of wind power curtailment is added to the objective function to calculate the total cost of wind power curtailment.

$$0 \leq s_{a,h,r} \leq W_{a,h,r} \qquad \forall a,h,r \in \mathcal{A},\mathcal{T},\mathcal{R} \tag{3.26}$$
$$\rho^c_{a,h,r} = W_{a,h,r} - s_{a,h,r} \qquad \forall a,h,r \in \mathcal{A},\mathcal{T},\mathcal{R} \tag{3.27}$$

HVDC constraint

For the three-area system, the power flow on the interconnecting HVDC cables is constrained by a maximum value. This constraint is presented in (3.28), where the power flow on the cables are constrained for each time interval.

$$-F_l^{max} \leq f_{l,h,r} \leq F_l^{max} \qquad \forall l,h,r \in \mathcal{L},\mathcal{T},\mathcal{R} \tag{3.28}$$

Power balance

The last constraint added to the discrete-time UC model is the power balance. The power balance must be satisfied for the total system during each time interval, hence the total generated power in the system plus/minus power flow in the HVDC cables must be equal to the total load minus the amount of load shedding. Load shedding is an act to prevent failure of the system when the demand strains the system capacity. Ideally, the amount of load shedding will be zero. The coefficient $G_{l,a}$ dictates the positive and negative direction of the power flow on each cable by taking the value ± 1, and zero if cable l is not connected to area a. $\mathcal{M}^a$ and $\mathcal{I}^a$ are the sets of hydropower units and thermal units located in area a.

$$\sum_{m \in \mathcal{M}^a} p_{m,h,r} + \sum_{i \in \mathcal{I}^a} g_{i,h,r} + s_{a,h,r} - \sum_{l \in \mathcal{L}} G_{l,a} f_{l,h,r} = L_{a,h,r} - \rho^s_{a,h,r} \qquad \forall a,h,r \in \mathcal{A},\mathcal{T},\mathcal{R} \tag{3.29}$$

Chapter 4

Continuous-time Unit Commitment

This chapter presents the fundamentals of a continuous-time optimization framework together with the characteristics of Bernstein polynomials and how these polynomials can be used to express different continuous-time trajectories. In the end, a mathematical formulation of the continuous-time UC model representing a three-area system will be presented. The mathematical formulation of the continuous-time model is based on a paper that was accepted for publication in The Power Systems Computation Conference (PSCC) later in 2020. The accepted preprint of the paper is available online, see [13]. In this master thesis, the model is extended to include offshore wind power, hence constraints for wind power generation and wind curtailment are added to the model.

4.1 Fundamentals of a Continuous-time Model

The continuous-time optimization framework directly models sub-hourly variations by representing all time-varying data and variables as smooth curves in time. The resulting optimization problem is then defined in terms of the coefficients of the chosen base polynomials. This allows ramping and other inter-temporal constraints to be enforced continuously within and between time intervals.

The continuous-time framework presents time-varying data and variables as polynomials of time instead of piece-wise constant functions. Several spline models can be used to approximate the continuous-time trajectory curve of a data set, where the accuracy of the spline model is dependent on the order of the basis. A high order will lead to a more accurate continuous-time trajectory. A convenient spline model is the Bernstein polynomials, where the time dependent decision variables will be defined by using the Bernstein polynomials of degree n. More about the Bernstein polynomials will be explained in **Sec. 4.2**.

By dividing the time horizon of the model into N intervals, $h \in \mathcal{T}$, of length δ_h, the time-dependent decision variables can be expressed as polynomials of the form as in (4.1), where $x(t)$ will be the equation for the continuous-time trajectory [13].

$$x(t) = \sum_{h \in \mathcal{T}} \mathbf{x}_h^T \cdot \mathbf{B}_n(\tau_h)\beta(\tau_h) \tag{4.1}$$

$\mathbf{x}_h$ will be the decision variables, containing $n+1$ Bernstein polynomial coefficients for each time interval h, and $\mathbf{B}_n$ is the vector of Bernstein polynomials of degree n. The equations for τ_h and $\beta(\tau_h)$ are expressed in (4.2) and (4.3), respectively.

$$\tau_h = \frac{1}{\delta_h}\left(t - \sum_{i<h} \delta_i\right) \qquad \forall h \in \mathcal{T} \tag{4.2}$$

$$\beta(\tau_h) = \begin{cases} 1, & 0 \leq \tau_h \leq 1 \\ 0, & \text{otherwise} \end{cases} \qquad \forall h \in \mathcal{T} \tag{4.3}$$

The value of τ_h together with the value of the $\beta(\tau_h)$-function will ensure that the decision variables in (4.1) will be zero for all other time intervals except the one that is investigated. This is an important factor because the Bernstein polynomials of degree n are defined on the interval $t \in [0, 1]$.

A numerical example is provided below to explain the meaning of the equations expressed in (4.2) and (4.3).

Hour $[h]$	**Time interval** [sec]	$\boldsymbol{\tau_0 = \frac{t}{3600}}$	$\boldsymbol{\tau_1 = \frac{t}{3600} - 1}$	$\boldsymbol{\tau_2 = \frac{t}{3600} - 2}$
0	$t \in [0, 3600]$	$\tau_0 \in [0, 1]$	$\tau_1 \in [-1, 0]$	$\tau_2 \in [-2, -1]$
1	$t \in [3600, 7200]$	$\tau_0 \in [1, 2]$	$\tau_1 \in [0, 1]$	$\tau_2 \in [-1, 0]$
2	$t \in [7200, 10800]$	$\tau_0 \in [2, 3]$	$\tau_1 \in [1, 2]$	$\tau_2 \in [0, 1]$

Table 4.1: Numerical values for τ_h, expressed in (4.2).

For the example, it is assumed that the time horizon is divided into three intervals of length $\delta_h = 3600\,\text{sec}$. **Table 4.1** shows the range of t together with the range of τ_h for the different time intervals. When inserting the values of τ_h into (4.3), it can be seen that $\beta(\tau_0)$ is one for hour 0 and for the first second in hour 1. For the rest of the time steps, $\beta(\tau_0)$ will be 0. The same holds for $\beta(\tau_1)$, where $\beta(\tau_1)$ will be one for the last second in hour 0, for hour 1 and for the first second in hour 2, while for the rest of the time steps, $\beta(\tau_1)$ will be zero. This ensures continuity of the trajectory between the time intervals, which is an important factor in the continuous-time framework. In the standard continuous-time optimization framework, C^1 continuity is defined for all decision variables $x(t)$. This means that both the value $x(t)$ and the value of the derivative, $\dot{x}(t)$, are required to be continuous over the change of time intervals.

4.2 Bernstein Polynomials

The Bernstein polynomial of degree n is defined by (4.4).

$$B_{i,n}(t) = \binom{n}{i} t^i (1-t)^{n-i}, \quad i \in [0, n],\ t \in [0, 1] \tag{4.4}$$

The binomial coefficient $\binom{n}{i}$ in (4.4) can be found by the expression in (4.5). The exponent on the t term increase by one as i increases, and the exponent on the $(1-t)$ term decrease by one as i increases.

$$\binom{n}{i} = \frac{n!}{i!(n-i)!} \tag{4.5}$$

In this thesis, the Bernstein polynomials of degree three will be used as a basis for each time interval h. This degree of freedom allows the application of C^1 continuity constraints between time intervals without drastically increasing the number of decision variables in the model. The Bernstein polynomials of degree three are expressed in (4.6). A linear combination of these polynomials can be used to create an infinite number of trajectories. The trajectory curve of each respective polynomial for $0 \leq t \leq 1$ is shown in **Fig. 4.1**.

$$\begin{aligned} \mathbf{B}_3(t) &= [B_{0,3}(t),\ B_{1,3}(t),\ B_{2,3}(t),\ B_{3,3}(t)] \\ &= [(1-t)^3,\ 3t(1-t)^2,\ 3t^2(1-t),\ t^3] \end{aligned} \tag{4.6}$$

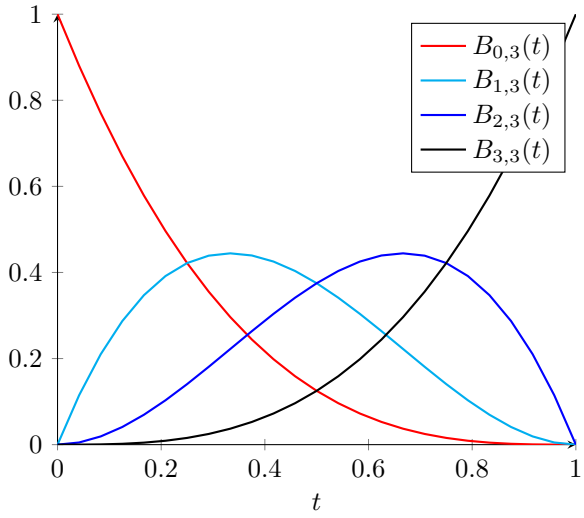

Figure 4.1: Bernstein polynomials of degree 3

The trajectory curves in **Fig. 4.1** show that when $t = 0$, $B_{0,3}(0)$ is one, while the rest of the polynomials will be zero. The same holds for $t = 1$, where $B_{3,3}(1)$ is one, while

the rest of the polynomials will be zero. This property is useful for applying C^1 continuity constraints for the decision variables.

The motivation for modeling the continuous-time trajectories using the Bernstein polynomials will be explained in the following sections, where different properties of the Bernstein polynomials are shown.

4.2.1 Derivative of Bernstein Polynomials

The derivatives of the Bernstein polynomials of degree n are polynomials of degree $n-1$. With the use of the definition of the Bernstein polynomials in (4.4), it can be shown that the derivative can be expressed as a linear combination of Bernstein polynomials for $0 \leq i \leq n$. The definition of the derivative is shown in (4.7).

$$\dot{B}_{i,n}(t) = \frac{d}{dt}\binom{n}{i} t^i (1-t)^{n-i} \tag{4.7}$$

By omitting the mathematical steps well described in [54], the derivative can be expressed as in (4.8).

$$\dot{B}_{i,n}(t) = n(B_{i-1,n-1}(t) - B_{i,n-1}(t)) \tag{4.8}$$

As can be seen, the derivative of the Bernstein polynomials can be expressed as the degree of the polynomial, n, multiplied by the difference between two Bernstein polynomials of degree $n-1$. This applies because the Bernstein polynomials of degree n form a basis for any polynomials of degree equal or less than n on the interval $t \in [0, 1]$.

In matrix, the derivative can be expressed as in (4.9)

$$\dot{\mathbf{B}}_n(t) = \mathbf{K} \cdot \mathbf{B}_{n-1}(t), \tag{4.9}$$

where $\mathbf{K}$ is a linear matrix that relates the derivative of $\mathbf{B}_n(t)$ to $\mathbf{B}_{n-1}(t)$. With this in mind, the derivative of Bernstein polynomials of degree three can be represented by Bernstein polynomials of degree two and a 4×3 $\mathbf{K}$ matrix, shown in (4.10).

$$\dot{\mathbf{B}}_3(t) = \mathbf{K} \cdot \mathbf{B}_2(t) = 3 \begin{bmatrix} -1 & 0 & 0 \\ 1 & -1 & 0 \\ 0 & 1 & -1 \\ 0 & 0 & 1 \end{bmatrix} \cdot \mathbf{B}_2(t) \tag{4.10}$$

4.2.2 Integral of Bernstein Polynomials

The indefinite integral of the Bernstein polynomials of degree n can be defined as in (4.11) [55].

$$\int B_{i,n}(t)dt = \frac{1}{n+1} \sum_{j=i+1}^{n+1} B_{j,n+1}(t) \tag{4.11}$$

From the definition, it can be seen that the integral of the Bernstein polynomials of degree n are related to the Bernstein polynomials of degree $n+1$. In matrix form, this

definition can be expressed as in (4.12), where $\mathbf{N}$ is a linear matrix that relates $\mathbf{B}_n(t)$ to $\mathbf{B}_{n+1}(t)$.

$$\int \mathbf{B}_n(t)dt = \mathbf{N} \cdot \mathbf{B}_{n+1}(t) \tag{4.12}$$

For Bernstein polynomials of degree three, the indefinite integral is expressed as in (4.13), where matrix $\mathbf{N}$ will be a 4×5 matrix.

$$\int \mathbf{B}_3(t)dt = \frac{1}{4}\begin{bmatrix} 0 & 1 & 1 & 1 & 1 \\ 0 & 0 & 1 & 1 & 1 \\ 0 & 0 & 0 & 1 & 1 \\ 0 & 0 & 0 & 0 & 1 \end{bmatrix} \cdot \mathbf{B}_4(t) \tag{4.13}$$

Another important property of the Bernstein polynomials is that all Bernstein polynomials of the same degree will have equal definite integrals over the time interval $t \in [0, 1]$, as shown in (4.14).

$$\int_0^1 B_{i,n}(t)dt = \frac{1}{n+1} \tag{4.14}$$

Hence, the definite integral of all Bernstein polynomials of degree three is given by (4.15),

$$\int_0^1 \mathbf{B}_3(t)dt = \frac{1}{4} \cdot \mathbf{1} \tag{4.15}$$

where $\mathbf{1}$ is a vector of ones. All of these properties will be used when formulating the constraints in the continuous-time UC model in Section 4.4.

4.2.3 The Bernstein Convex Hull Property

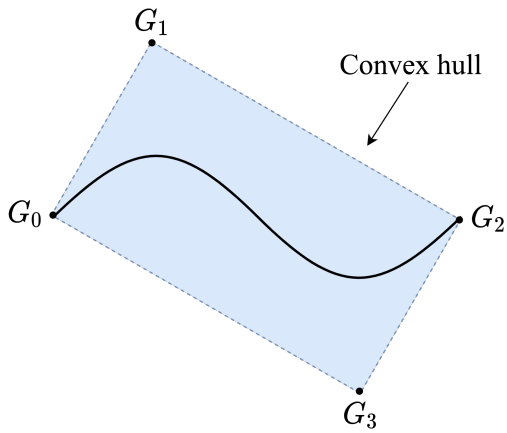

Figure 4.2: The Bernstein Convex Hull

The Bernstein convex hull property is an important tool when formulating the continuous-time UC model. This property ensures that the continuous-time trajectories are never outside the convex hull defined by the Bernstein polynomial coefficients. The maximum and the minimum coefficient will bound the value of the polynomial, which makes it possible to impose inequality constraints on the decision variable $x(t)$ for all times t by directly bounding the coefficients. **Fig. 4.2** shows an example of a Bernstein convex hull. As can be seen from the figure, the continuous-time trajectory is contained within the convex hull defined by the four Bernstein coefficients.

4.3 Continuous-time Trajectories

4.3.1 Generation and Ramping Trajectories

In the discrete-time optimization framework, the generation profile for each generator unit is modeled as a piece-wise constant curve. In the continuous-time framework, the continuous-time generation trajectory will be a smooth and continuous curve, expressed with the use of Bernstein polynomials of degree n and the Bernstein polynomial coefficients. A continuous-time generation trajectory can be expressed as in (4.16),

$$G(t) = \sum_{h \in \mathcal{T}} \mathbf{G}_h^T \cdot \mathbf{B}_n(t), \tag{4.16}$$

where $\mathbf{G}_h^T = \left[G_0^h, G_1^h, \ldots, G_{n-1}^h, G_n^h\right]$ is the vector of Bernstein polynomial coefficients for the time interval h. The coefficient vector will contain $n+1$ elements, and these coefficients will be the time dependent decision variables in the continuous-time UC model.

The continuous-time ramping trajectory can be found by taking the derivative of the continuous-time generation trajectory in (4.16). The ramping trajectory can then be expressed as in (4.17), where the property of (4.9) is applied.

$$R(t) = \dot{G}(t) = \sum_{h \in \mathcal{T}} \mathbf{R}_h^T \cdot \mathbf{B}_{n-1}(t) \tag{4.17}$$

The vector of Bernstein polynomial coefficients for the continuous-time ramping trajectory is here introduced as $\mathbf{R}_h$. These coefficients can be expressed as a combination of $\mathbf{G}_h$, decided by the $\mathbf{K}$ matrix.

$$\mathbf{R}_h = \mathbf{K}^T \cdot \mathbf{G}_h \tag{4.18}$$

For a generation trajectory expressed with Bernstein polynomials of degree three, the coefficients for the ramping trajectory can be expressed with use of the linear matrix $\mathbf{K}$ expressed in (4.10). By inserting this matrix in (4.18), the ramping coefficients can be expressed as in (4.19).

$$\begin{aligned} R_0^h &= 3\left(G_1^h - G_0^h\right) \\ R_1^h &= 3\left(G_2^h - G_1^h\right) \\ R_2^h &= 3\left(G_3^h - G_2^h\right) \end{aligned} \tag{4.19}$$

4.3.2 Load and Wind Series Trajectories

In the discrete-time optimization framework, the load profile is modeled as a piece-wise constant curve over a specified time interval. This piece-wise constant load profile can be used to approximate the continuous-time load with the use of Bernstein polynomials. The approximation of the continuous-time load profile with the use of Bernstein polynomials of degree n, can be expressed as in (4.20).

$$L(t) = \sum_{h \in \mathcal{T}} \mathbf{L}_h^T \cdot \mathbf{B}_n(t) \tag{4.20}$$

$\mathbf{L}_h^T = \left[L_0^h,\, L_1^h,\, \ldots,\, L_{n-1}^h,\, L_n^h\right]$ is the Bernstein polynomial coefficient vector for the load variable in time interval h. The dimension of the coefficient vector is $(n+1) \times 1$. The load trajectory for a given time interval h, with the continuous-time sub-interval $t \in [0, 1]$, can be expressed as in (4.21) when Bernstein polynomials of degree three are used.

$$L(h,t) = L_0^h B_{0,3}(t) + L_1^h B_{1,3}(t) + L_2^h B_{2,3}(t) + L_3^h B_{3,3}(t) \tag{4.21}$$

To approximate the continuous-time load trajectory, the coefficient vector $\mathbf{L}_h$ must be found for each time interval h. The same holds for the approximated continuous-time wind series. In this thesis, the continuous-time load and wind series are calculated from the discrete time data by a least-squares error fit to the Bernstein polynomials. This will be further explained in the next section.

4.3.3 Polynomials Least Square Fitting by Using Bernstein Polynomials

The least squares method is a statistical procedure to determine the line of best fit for a set of data points by minimizing the sum of the square error between the fitted line and the data points [56]. When using Bernstein polynomials, the fitted line will be on the form expressed in (4.22), where c_i will be the coefficient for each Bernstein polynomial $B_{i,n}$ of degree n.

$$L(x) = \sum_{i \in n} c_i B_{i,n}(x) \tag{4.22}$$

Given $\{x_j\}_{1 \leq j \leq l+1} \in (0, 1)$, a set of points such that $0 < x_1 < \cdots < x_{l+1} < 1$, the goal of polynomials least square fitting is to find the polynomial $L(x)$ on the interval $[0, 1]$, for each time interval h, that minimizes the sum of the squares of the deviations from the data $\{f_j\}_{1 \leq j \leq l+1} \in \mathbb{R}$. The sum of the square errors is expressed in (4.23).

$$\sum_{j=1}^{l+1} |f_j - L(x_j)|^2 \tag{4.23}$$

For approximating the continuous-time load curve for all time intervals h, the coefficients $\mathbf{L}_h$ of the polynomial $L(t)$ in (4.20) must be found. In the least squares sense, this can be done by solving the linear system $\mathbf{A}^T\mathbf{c} = \mathbf{f}$, where $\mathbf{A}$ is the $((n-1)N+2) \times (l+1)$ Bernstein-Vandermonde matrix [57]. N is the number of time intervals, while $(l+1)$ is the

number of data points. **f** and **c** are a $(l+1)\times 1$ data vector and a $((n-1)N+2)\times 1$ Bernstein coefficient vector for all time intervals h, respectively. The **A** matrix will have full rank $l+1$, so the linear system will have a unique solution given by the *normal equations* in (4.24) [57].

$$\mathbf{A}\mathbf{A}^T\mathbf{c} = \mathbf{A}\mathbf{f} \rightarrow \mathbf{c} = \left(\mathbf{A}\mathbf{A}^T\right)^{-1}\mathbf{A}\mathbf{f} \tag{4.24}$$

The number of data points $l+1$ is related to the number of time intervals N and the length of each time interval δ_h, where $l+1 = N\delta_h$. An example of how the Bernstein-Vandermonde matrix **A** is implemented and how the coefficients $\mathbf{L}_h$ in (4.20) are found with the use of the unique solution in (4.24), are shown below.

Implementation of matrix A and solving the normal equations for the load coefficients

For this example, it is assumed that the number of time intervals are equal to $N = 3$ and that the degree of the Bernstein polynomials is $n = 3$. When implementing the Bernstein-Vandermonde matrix, it is important to ensure continuity between the time intervals such that the resulting continuous-time trajectory will be continuous. The polynomial for the load trajectory for three time intervals can be expressed as in (4.25), where (4.22) have been written out for three time intervals.

$$\begin{aligned} L(t) = {} & c_0^0 B_{0,3}^0(t) + c_1^0 B_{1,3}^0(t) + c_2^0 B_{2,3}^0(t) + c_3^0 B_{3,3}^0(t) \\ & + c_0^1 B_{0,3}^1(t) + c_1^1 B_{1,3}^1(t) + c_2^1 B_{2,3}^1(t) + c_3^1 B_{3,3}^1(t) \\ & + c_0^2 B_{0,3}^2(t) + c_1^2 B_{1,3}^2(t) + c_2^2 B_{2,3}^2(t) + c_3^2 B_{3,3}^2(t) \end{aligned} \tag{4.25}$$

To ensure C^1 continuity between time intervals, the load at the end of the time interval h will be equal to the load at the beginning of the time interval $h+1$. The same applies for the derivative of the load. Hence, $c_0^h = c_3^{h+1}$ and $c_1^h - c_0^h = c_3^{h+1} - c_2^{h+1}$. For the last time interval, these constraints will not apply. By implementing these two equality constraints into (4.25), the load trajectory can be rewritten to the expression in (4.26).

$$\begin{aligned} L(t) = {} & c_0^0 B_{0,3}^0 + c_1^0 B_{1,3}^0 \\ & + c_0^1 \left(B_{0,3}^1 + B_{3,3}^0 + 2B_{2,3}^0\right) + c_1^1 \left(B_{1,3}^1 - B_{2,3}^0\right) \\ & + c_0^2 \left(B_{0,3}^2 + B_{3,3}^1 + 2B_{2,3}^1\right) + c_1^2 \left(B_{1,3}^2 - B_{2,3}^1\right) + c_2^2 B_{2,3}^2 + c_3^2 B_{3,3}^2 \end{aligned} \tag{4.26}$$

For this example, it can be seen that there will be $(n-1)N + 2 = 8$ Bernstein coefficients, where the coefficients will be the decision variables. From (4.26), the **A** matrix and the coefficient vector **c** can be expressed as in (4.27). Each column in the **A** matrix represents one time interval h and each row is related to the respective coefficient c_i^h.

$$\mathbf{A} = \begin{bmatrix} B_{0,3}^0 & 0 & 0 \\ B_{1,3}^0 & 0 & 0 \\ B_{3,3}^0 + B_{2,3}^0 & B_{0,3}^1 & 0 \\ -B_{2,3}^0 & B_{1,3}^1 & 0 \\ 0 & B_{3,3}^1 + B_{2,3}^1 & B_{0,3}^2 \\ 0 & -B_{2,3}^1 & B_{1,3}^2 \\ 0 & 0 & B_{2,3}^2 \\ 0 & 0 & B_{3,3}^2 \end{bmatrix}, \mathbf{c} = \begin{bmatrix} c_0^0 \\ c_1^0 \\ c_0^1 \\ c_1^1 \\ c_0^2 \\ c_1^2 \\ c_2^2 \\ c_3^2 \end{bmatrix} \tag{4.27}$$

The number of columns in the **A** matrix are dependent on the length of each time interval, δ_h. If δ_h is $3600\,\text{sec}$, each column in the presented **A** matrix will actually contain 3600 columns. This means that the dimension of the **A** matrix will be $8 \times (3 \cdot 3600)$, where each column will contain the value of the Bernstein polynomial when the correct time step is inserted. The time steps for each time interval h will range between 0 and 1.

After solving the normal equations in (4.24) for the **c** vector, the coefficient vector **c** is used to express the load coefficient vector $\mathbf{L}_h$, which contains $n+1$ coefficients for each time interval h. This is done for all time intervals, except the last one, by the equations in (4.28). The $\mathbf{L}_h$ vector for the last time step $N-1$ will be equal to the $n+1$ last coefficients in the **c** vector.

$$\begin{aligned} L_0^h &= c_0^h \\ L_1^h &= c_1^h \\ &\vdots \\ L_{n-2}^h &= c_{n-2}^h \\ L_{n-1}^h &= 2c_0^{h+1} - c_1^{h+1} \\ L_n^h &= c_0^{h+1} \end{aligned} \tag{4.28}$$

The coefficient vector $\mathbf{L}_h$ will be applied to (4.20) to express the continuous-time load trajectory. This approach of implementing the **A** matrix can be done for any degree of the Bernstein polynomials and for an arbitrary number of time intervals.

4.4 Mathematical Formulation of the Continuous-time UC Model

One fundamental difference between the discrete-time representation and the continuous-time representation is that the decision variables will now be a vector containing four Bernstein polynomial coefficients instead of one variable. This difference requires a new formulation of the objective function and the constraints in the continuous-time UC model. A number of new constraints will be added to the model to ensure continuity and smoothness between time intervals. The continuous-time model will be formulated with the use of seven binary variables; $u_i(t)$, $z_m(t)$, $SU_i(t)$, $SD_i(t)$, $SU_m(t)$, $Sm_i(t)$ and $w_m(t)$. The

first six binary variables are the same as in the discrete-time model, while the last one, $w_m(t)$, will be added to the model to ensure correct uploading of the discharge segments. As for the discrete-time model, commitment, startups and shutdowns of the generators will only be decided in the hour shifts, but the production can change throughout the entire time interval. The same applies for the power flow on the HVDC cables. For an explanation of all symbols used in the mathematical formulation, the reader is referred to the nomenclature shown at the beginning of the thesis.

Objective function

The objective function from the discrete-time formulation, (3.1), can be presented in continuous-time by utilizing the property of (4.15) to simplify the integrals into sums. The continuous-time objective function is presented in (4.29) and the objective will still be to minimize the total cost of the system. The different costs are the same as in the discrete-time model.

$$Z = \alpha + \frac{1}{4}\sum_{h\in\mathcal{T}} \delta_h \mathbf{1}^T \cdot \left(C^c \boldsymbol{\rho}^c_h + C^s \boldsymbol{\rho}^s_h\right) + \frac{1}{4}\sum_{m\in\mathcal{M}}\sum_{h\in\mathcal{T}} \delta_h \mathbf{1}^T \cdot \left(C^b \mathbf{q}^b_{m,h} + C^o \mathbf{q}^o_{m,h}\right) + \sum_{i\in\mathcal{I}}\sum_{h\in\mathcal{T}} \left(\frac{1}{4}\delta_h C_i \mathbf{1}^T \cdot \mathbf{g}_{i,h} + C_i^{start} SU_{i,h} + C_i^{stop} SD_{i,h}\right) \tag{4.29}$$

Thermal generation constraints

The constraints describing the thermal generation in the continuous-time model are presented in (4.30) to (**??**), and are formulated with the use of the binary commitment variable $u_i(t)$. Since the decision variable $g_i(t)$ is now a vector of four Bernstein polynomial coefficients, the commitment variable will be a vector, expressed in (4.31). It can be seen that the first two Bernstein polynomial coefficients in $\mathbf{g}_{i,h}$ for hour h are related to the commitment of the generator in hour h, while the two last coefficients are related to the commitment of the generator in hour $h+1$. This ensures that the thermal generator can ramp up the production from zero to above G_i^{min}, or ramp down the production to zero, during time interval h. This smooth ramping of the production is necessary when the continuity constrains for the thermal production variable will be applied. Constraint (4.30) uses the convex hull property to directly bound the thermal production variable by an upper and lower limit. Constraint (4.32) to (4.34) will be the same as for the discrete-time UC model, and will ensure the correct commitment of the thermal generators.

$$G_i^{min}\mathbf{u}_{i,h} \leq \mathbf{g}_{i,h} \leq G_i^{max}\mathbf{u}_{i,h} \qquad \forall i,h \in \mathcal{I},\mathcal{T} \tag{4.30}$$

$$\mathbf{u}_{i,h} = [u_{i,h},\ u_{i,h},\ u_{i,h+1},\ u_{i,h+1}]^T \qquad \forall i,h \in \mathcal{I},\mathcal{T} \tag{4.31}$$

$$SU_{i,h} - SD_{i,h} = u_{i,h+1} - u_{i,h} \qquad \forall i,h \in \mathcal{I},\mathcal{T} \tag{4.32}$$

$$SU_{i,h} + SD_{i,h} \leq 1 \qquad \forall i,h \in \mathcal{I},\mathcal{T} \tag{4.33}$$

$$u_{i,h}, SU_{i,h}, SD_{i,h} \in \{0,1\} \qquad \forall i,h \in \mathcal{I},\mathcal{T} \tag{4.34}$$

Thermal generators can be slow to change their production, and the ramping capabilities is often a limiting factor for the flexibility of the thermal units. Therefore, limitations on the derivative $\dot{g}_i(t)$ are imposed in (4.35) and (4.36) to ensure that the ramping of the thermal production stays within specified limits, R_i^{up} and R_i^{down}, by utilizing the property of (4.10). When there is a startup or a shutdown, the ramping limit is increased to G_i^{max}.

$$\frac{1}{\delta_h}\mathbf{g}_{i,h}^T \cdot \mathbf{K} \leq (R_i^{up} + (G_i^{max} - R_i^{up})SU_{i,h})\mathbf{1}^T \qquad \forall i,h \in \mathcal{I},\mathcal{T} \qquad (4.35)$$

$$\frac{1}{\delta_h}\mathbf{g}_{i,h}^T \cdot \mathbf{K} \geq -(R_i^{down} + (G_i^{max} - R_i^{down})SD_{i,h})\mathbf{1}^T \qquad \forall i,h \in \mathcal{I},\mathcal{T} \qquad (4.36)$$

Reservoir volume constraints

The constraints for reservoir volume of the continuous-time model are presented in (4.37) to (4.39). Constraint (4.37) sets the initial volume of each reservoir at the beginning of the time horizon equal to a value V_m^0, where v_{mh} is the instantaneous volume at the beginning of interval h for reservoir m. Constraint (4.38) calculates the change in volume between two time intervals by integrating the net flow, $q_m^{net}(t)$, over the entire time interval by the use of property (4.15). Constraint (4.39) bounds the reservoir volume within the time interval between zero and the maximum reservoir volume. The reservoir volume within the time interval is found by using the property of (4.13).

$$v_{m0} = V_m^0 \qquad \forall m \in \mathcal{M} \qquad (4.37)$$

$$v_{m,h+1} - v_{m,h} = \frac{1}{4}\delta_h \mathbf{1}^T \cdot \mathbf{q}_{m,h}^{net} \qquad \forall m,h \in \mathcal{M},\mathcal{T} \qquad (4.38)$$

$$\mathbf{0} \leq v_{m,h}\mathbf{1} + \delta_h \mathbf{N}^T \cdot \mathbf{q}_{m,h}^{net} \leq V_m \mathbf{1} \qquad \forall m,h \in \mathcal{M},\mathcal{T} \qquad (4.39)$$

Future cost bounds

As for the discrete-time UC model, the future expected cost of the hydro system is bound by a set of linear Benders cuts and are dependent on the end volume of water in each reservoir. For the proposed model, $WV_{m,k}$ and D_k are calculated by looking at a long-term hydrothermal model with the integration of wind power in the same way as done in [53] for a hydrothermal system. Constraint (4.40) calculates the future expected cost α, which is directly added to the objective function in (4.29).

$$\alpha > \sum_{m \in \mathcal{M}} WV_{m,k} v_{m,N+1} + D_k \qquad \forall k \in \mathcal{K} \qquad (4.40)$$

Hydropower topology constraints

The waterways of the cascaded system are modelled by three separate routes: the spill gate, the bypass gate and the discharge through each turbine segment. An illustration of the three main waterways together with the regulated and unregulated natural inflow can

be seen in **Fig. 3.3** in the mathematical discrete-time UC formulation. The hydropower topology constraints (4.41) to (4.44) are equality constraints. By equating the polynomial coefficients, the constraints will be satisfied in the continuous-time model. Constraint (4.41) calculates the net inflow into each reservoir m, while constraint (4.42) calculates the total controlled flow out of each reservoir. The sum of the controlled flow into each reservoir from the upstream system is calculated in (4.43), while constraint (4.44) expresses the total released flow out of each reservoir. The constraints presented in (4.45) to (4.47) sets an upper and lower limitation on the water flows with the use of the convex hull property to bound the variables.

$$\mathbf{q}^{net}_{m,h} = \mathbf{I}_{m,h} + \mathbf{q}^{in}_{m,h} - \mathbf{q}^{out}_{m,h} \qquad \forall m,h \in \mathcal{M},\mathcal{T} \qquad (4.41)$$

$$\mathbf{q}^{out}_{m,h} = \mathbf{q}^{rel}_{m,h} + \mathbf{q}^{o}_{m,h} \qquad \forall m,h \in \mathcal{M},\mathcal{T} \qquad (4.42)$$

$$\mathbf{q}^{in}_{m,h} = \sum_{j \in \mathcal{J}^d_m} \mathbf{q}^{d}_{j,h} + \sum_{j \in \mathcal{J}^b_m} \mathbf{q}^{b}_{j,h} + \sum_{j \in \mathcal{J}^o_m} \mathbf{q}^{o}_{j,h} \qquad \forall m,h \in \mathcal{M},\mathcal{T} \qquad (4.43)$$

$$\mathbf{q}^{rel}_{m,h} = \mathbf{q}^{d}_{m,h} + \mathbf{q}^{b}_{m,h} - \mathbf{I}^{u}_{m,h} \qquad \forall m,h \in \mathcal{M},\mathcal{T} \qquad (4.44)$$

$$\mathbf{0} \leq \mathbf{q}^{d}_{m,h} \leq Q^{d}_{m} \cdot \mathbf{1} \qquad \forall m,h \in \mathcal{M},\mathcal{T} \qquad (4.45)$$

$$\mathbf{0} \leq \mathbf{q}^{b}_{m,h} \leq Q^{b}_{m} \cdot \mathbf{1} \qquad \forall m,h \in \mathcal{M},\mathcal{T} \qquad (4.46)$$

$$\mathbf{0} \leq \mathbf{q}^{rel}_{m,h} \qquad \forall m,h \in \mathcal{M},\mathcal{T} \qquad (4.47)$$

Hydropower production

The assumption that the discharge segments will be uploaded in correct order is not valid in the continuous-time UC model. The segment with the highest efficiency will still be uploaded first, but there is now no guarantee that segment n will be at its maximum capacity all the time segment $n+1$ is used. To ensure that segment $n+1$ will not be used before segment n is at its maximum capacity, the binary variable $w_{m,n}(t)$ is introduced.

$$w_{m,n,h} = \begin{cases} 1, & \text{segment } n \text{ is at maximum capacity} \\ 0, & \text{otherwise} \end{cases} \qquad \forall m,h,n \in \mathcal{M},\mathcal{T},\mathcal{N}_m \qquad (4.48)$$

This binary variable will force segment n to be at maximum capacity before segment $n+1$ can be used. The constraints for hydropower production are expressed in (4.49) to (4.52), where the two last constraints added ensure correct uploading of the discharge segments. If the binary variable is zero for discharge segment $n-1$, the constraint expressed in (4.52) will ensure that the flow through discharge segment n is zero. If the binary variable is one for discharge segment $n-1$ and zero for discharge segment n, the constraints expressed in (4.51) and (4.52) will ensure that the flow through discharge segment n is between zero and maximum flow. When the binary variable is one for discharge segment n, the flow through the discharge segment, $q^{d}_{m,n}(t)$, will be at maximum flow, $Q^{d}_{m,n}$. The flow through the discharge segments are bound with an upper and lower limit with the use of the convex hull property.

$$\mathbf{q}^d_{m,h} = \sum_{n \in \mathcal{N}_m} \mathbf{q}^d_{m,n,h} \qquad \forall m, h \in \mathcal{M}, \mathcal{T} \tag{4.49}$$

$$\mathbf{p}_{m,h} = \sum_{n \in \mathcal{N}_m} \eta_{m,n} \mathbf{q}^d_{m,n,h} \qquad \forall m, h \in \mathcal{M}, \mathcal{T} \tag{4.50}$$

$$Q^d_{m,n} w_{m,n,h} \mathbf{1} \leq \mathbf{q}^d_{m,n,h} \leq Q^d_{m,n} \mathbf{1} \qquad \forall m, h, n \in \mathcal{M}, \mathcal{T}, \mathcal{N}_m \tag{4.51}$$

$$\mathbf{q}^d_{m,n,h} \leq Q^d_{m,n} w_{m,n-1,h} \mathbf{1} \qquad \forall m, h, n \in \mathcal{M}, \mathcal{T}, \mathcal{N}_m \backslash \{0\} \tag{4.52}$$

Hydropower generation constraints

The hydropower generation constraints for the continuous-time model will be expressed with the use of the binary commitment variable $z_m(t)$, which now will be a vector of four elements. For the hydropower generation constraint (4.53), it can be seen that all the Bernstein polynomial coefficients in the decision variable $\mathbf{p}_{m,h}$ for hour h are related to the commitment of the generator in hour h. This forces the hydropower unit commitment decision to be constant during a time interval h, and ensures that the production never is between zero and P^{min}_m, which often is a forbidden production area for hydropower units. Unlike the smooth operation enforced on the thermal generators, discontinuous jumps in the hydropower production curve when there are startups and shutdowns are therefore permitted. If this was not taken into account, the hydropower plants would never be able to start and stop. Constraint (4.53) limits the hydropower production within an upper and lower limit with the use of the convex hull property. As in the discrete-time model, (4.55) and (4.56) ensure correct startup and shutdown of the hydropower plants.

$$P^{min}_m \mathbf{z}_{m,h} \leq \mathbf{p}_{m,h} \leq P^{max}_m \mathbf{z}_{m,h} \qquad \forall m, h \in \mathcal{M}, \mathcal{T} \tag{4.53}$$

$$\mathbf{z}_{m,h} = z_{m,h} \cdot \mathbf{1} \qquad \forall m, h \in \mathcal{M}, \mathcal{T} \tag{4.54}$$

$$SU_{m,h} - SD_{m,h} = z_{m,h+1} - z_{m,h} \qquad \forall m, h \in \mathcal{M}, \mathcal{T} \tag{4.55}$$

$$SU_{m,h} - SD_{m,h} \leq 1 \qquad \forall m, h \in \mathcal{M}, \mathcal{T} \tag{4.56}$$

$$z_{m,h}, SU_{m,h}, SD_{m,h} \in \{0, 1\} \qquad \forall m, h \in \mathcal{M}, \mathcal{T} \tag{4.57}$$

Wind power generation and curtailment

For the wind power generation constraint in (4.58), the convex hull property is again used to bound the Bernstein polynomial coefficients in the decision variable $s(t)$ within an upper and lower limit. The maximum wind power series, $\mathbf{W}_h$, is now containing four Bernstein polynomial coefficients for each time interval h, and is converted to a continuous curve by the same method as for the load curve, explained in **Sec. 4.3.3**. The wind curtailment will also be a vector containing four Bernstein polynomial coefficients, and is calculated in (4.59) as the difference between the maximum wind power curve and the actual produced wind power.

$$\mathbf{0} \leq \mathbf{s}_h \leq \mathbf{W}_h \qquad \forall h \in \mathcal{T} \tag{4.58}$$
$$\boldsymbol{\rho}^c_h = \mathbf{W}_h - \mathbf{s}_h \qquad \forall h \in \mathcal{T} \tag{4.59}$$

HVDC constraint

The power flow on the HVDC cables is bound by a maximum flow limit with the use of the convex hull property to bound the coefficients in $f_{l,h}$ for all time intervals.

$$-F^{max}_l \mathbf{1} \leq \mathbf{f}_{l,h} \leq F^{max}_l \mathbf{1} \qquad \forall l, h \in \mathcal{L}, \mathcal{T} \tag{4.60}$$

Power balance

Constraint (4.61) shows the power balance, which needs to be satisfied for each area over all time intervals. Hence, the total generated power in the system plus/minus the power flow on the HVDC cables must be equal to the total load in the system minus the amount of load shedding. If the amount of load shedding is zero for all areas, the power balance will preserve a continuous total production curve. But if load shedding occurs, discontinuous jumps will occur in the total generation profile because C^1 continuity constraints are not applied for the load shedding curve. The coefficient $G_{l,a}$ dictates the positive and negative direction of power flow on the HVDC cables, and $\mathcal{M}_a$ and $\mathcal{I}_a$ are the sets of hydropower and thermal units located in the area a.

$$\sum_{m \in \mathcal{M}_a} \mathbf{p}_{m,h} + \sum_{i \in \mathcal{I}_a} \mathbf{g}_{i,h} + \mathbf{s}_{a,h} - \sum_{l \in \mathcal{L}} G_{l,a} \mathbf{f}_{l,h} = \mathbf{L}_{a,h} - \boldsymbol{\rho}^s_{a,h} \qquad \forall a, h \in \mathcal{A}, \mathcal{T} \tag{4.61}$$

Continuity constraints

One important aspect of the continuous-time optimization framework is that the value of the decision variable and its derivative can be continuous over time interval shifts. C^1 continuity constraints will be added in the continuous-time model to ensure continuity and smoothness between time intervals. The C^1 continuity constraints can be expressed with the use of the Bernstein polynomial coefficients of the decision vector **x**, where the coefficients can be labelled as $\mathbf{x}^i$ for $i \in \{0, 1, 2, 3\}$. With this in mind, the continuity constraints are expressed as in (4.62) and (4.63).

$$\mathbf{x}^3_h = \mathbf{x}^0_{h+1} \qquad \forall h \in \mathcal{T} \backslash \{N\} \tag{4.62}$$
$$\mathbf{x}^3_h - \mathbf{x}^2_h = \mathbf{x}^1_{h+1} - \mathbf{x}^0_{h+1} \qquad \forall h \in \mathcal{T} \backslash \{N\} \tag{4.63}$$

The continuity constraint (4.62) ensures C^0 continuity between time intervals. Hence, the value of the decision variable at the end of time interval h is equal to the value of the decision variable at the beginning of time interval $h + 1$. By applying the constraint expressed in (4.63), C^1 continuity is ensured between the time interval shifts. Hence, also

the value of the derivative of the decision variable at the end of time interval h is equal to the value of the derivative of the decision variable at the beginning of time interval $h+1$. The continuity constraints in (4.62) and (4.63) are added to the optimization problem for the thermal production decision variable $\mathbf{g}_{i,h}$, the offshore wind production decision variable $\mathbf{s}_{a,h}$ and the power flow decision variable $\mathbf{f}_{l,h}$ for all times h in constraint (4.64) to (4.69). This enforces C^1 continuity, meaning that the curves have continuous values and derivatives for all points in time.

$$\mathbf{g}^3_{i,h} = \mathbf{g}^0_{i,h+1} \qquad \forall i, h \in \mathcal{I}, \mathcal{T}\backslash\{N\} \tag{4.64}$$
$$\mathbf{g}^3_{i,h} - \mathbf{g}^2_{i,h} = \mathbf{g}^1_{i,h+1} - \mathbf{g}^0_{i,h+1} \qquad \forall i, h \in \mathcal{I}, \mathcal{T}\backslash\{N\} \tag{4.65}$$
$$\mathbf{s}^3_{a,h} = \mathbf{s}^0_{a,h+1} \qquad \forall a, h \in \mathcal{A}, \mathcal{T}\backslash\{N\} \tag{4.66}$$
$$\mathbf{s}^3_{a,h} - \mathbf{s}^2_{a,h} = \mathbf{s}^1_{a,h+1} - \mathbf{s}^0_{a,h+1} \qquad \forall a, h \in \mathcal{A}, \mathcal{T}\backslash\{N\} \tag{4.67}$$
$$\mathbf{f}^3_{l,h} = \mathbf{f}^0_{l,h+1} \qquad \forall l, h \in \mathcal{L}, \mathcal{T}\backslash\{N\} \tag{4.68}$$
$$\mathbf{f}^3_{l,h} - \mathbf{f}^2_{l,h} = \mathbf{f}^1_{l,h+1} - \mathbf{f}^0_{l,h+1} \qquad \forall l, h \in \mathcal{L}, \mathcal{T}\backslash\{N\} \tag{4.69}$$

Less strict continuity constraints are added to the variables connected to the hydropower units. Because of the discontinuous jumps in the hydropower production between time intervals when there is a startup or a shutdown, enforcing C^1 continuity constraints on the variables related to the hydropower units will not be possible. The C^0 continuity constraint in (4.62) is applied to the flow through the bypass gate and the spill gate in (4.70) and (4.71), respectively.

$$\mathbf{q}^{b,3}_{m,h} = \mathbf{q}^{b,0}_{m,h+1} \qquad \forall m, h \in \mathcal{M}, \mathcal{T}\backslash\{N\} \tag{4.70}$$
$$\mathbf{q}^{o,3}_{m,h} = \mathbf{q}^{o,0}_{m,h+1} \qquad \forall m, h \in \mathcal{M}, \mathcal{T}\backslash\{N\} \tag{4.71}$$

As there is a need for discontinuous jumps in the hydropower production during startups and shutdowns, enforcing C^0 continuity on $\mathbf{p}_{m,h}$ will not be possible. Instead, constraint (4.62) is replaced with the inequality constraints in (4.72) and (4.73), which makes the hydropower production C^0 continuous over time interval changes except if a startup or shutdown occurs. Even though the individual hydropower plants may have discontinuous jumps between time intervals, the overall production trajectory will be continuous if the amount of load shedding is zero. This is enforced in the power balance, (4.61), because all other variables in that equation has continuous derivatives between the time intervals. However, if load shedding takes place, discontinuous jumps in the overall production trajectory will occur.

$$\mathbf{p}^3_{m,h} - \mathbf{p}^0_{m,h+1} \leq P^{max}_m SD_{m,h} \qquad \forall m, h \in \mathcal{M}, \mathcal{T}\backslash\{N\} \tag{4.72}$$
$$\mathbf{p}^0_{m,h+1} - \mathbf{p}^3_{m,h} \leq P^{max}_m SU_{m,h} \qquad \forall m, h \in \mathcal{M}, \mathcal{T}\backslash\{N\} \tag{4.73}$$

Chapter 5

Three-area Test System

5.1 Method

A three-area test system with simplified representation of a hydro area, a thermal area and an offshore wind area has been applied to investigate the interactions between a hydro dominated system and a thermal dominated system when offshore wind power is integrated. In this chapter the input data for the stylized three-area test system will be presented. All data used in the case study is scaled down with a system scaling rate, which is the rate between the cascaded hydropower system and the actual hydropower capacity in Norway. The continuous-time UC formulation of the system will be used to model the system operation while implicitly minimizing the structural imbalances and accounting for the ramping limitations of the thermal generators. The system costs, wind power utilization and power flow characteristics for different hydrological states and wind conditions will be compared, and the differences to the standard discrete-time model formulation will be investigated.

The time horizon is set to 24 hours in both models, with hourly time intervals in the continuous-time model. The discrete-time model will have quarterly time intervals, but commitment, shutdown and startup of generators can only occur in the hour shifts.

5.1.1 Simplifications and Definitions

The UC models in this thesis will operate under the following assumptions and simplifications:

1. There will be no internal power limits on the power flow within each area.
2. The unit commitment status of all the generators are not decided initially, but will be selected at the beginning of the first time interval.
3. The continuous-time model will be implemented with the use of Bernstein polynomials of degree three. This will keep the number of variables in the model to an acceptable number without sacrificing accuracy.

4. Both the continuous-time load profile and wind series will be approximated with the use of Bernstein polynomials of degree three.

5. The installed capacity of the generating units, the load and the wind series are scaled down by a system scaling rate.

6. Constraints for start-up time for thermal generators will not be included in the UC models.

5.1.2 Approximating the Continuous-time Trajectory Using Different Degrees of Bernstein Polynomials

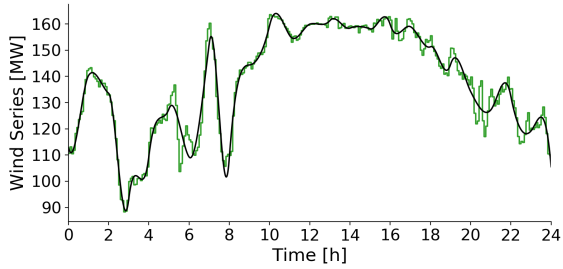

(a) Bernstein polynomials of degree 3

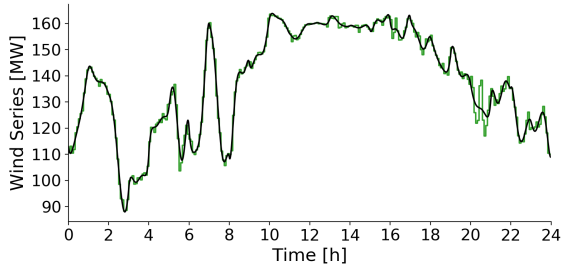

(b) Bernstein polynomials of degree 5

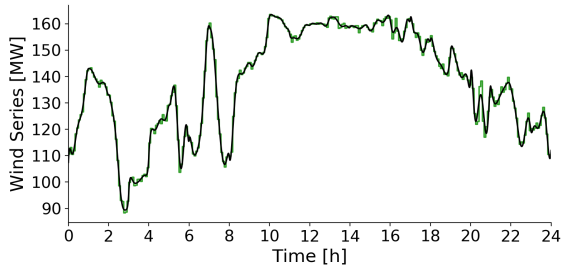

(c) Bernstein polynomials of degree 7

Figure 5.1: Continuous-time trajectory using different degrees of Bernstein polynomials.

The accuracy of the approximation of continuous-time trajectories depends on the degree of the Bernstein polynomials. A higher degree of the Bernstein polynomials will result in a more accurate approximation of the continuous-time trajectory. This can be seen from the figures in **Fig. 5.1**, where the approximated continuous-time wind profiles for three different degrees of Bernstein polynomials are presented. The green curve is the discrete-time wind profile with a 5-min resolution, and the black curve is the approximated continuous-time trajectory. The wind profile data is from January 1st, 2018, available in [58].

Fig. 5.1a shows the approximated trajectory when using Bernstein polynomials of degree three. It can be seen that the deviation between the black and the green curve is large in periods when there are large and rapid changes in the wind profile. This deviation is reduced in **Fig. 5.1b**, where the continuous-time trajectory is approximated with the use of Bernstein polynomials of degree five. In **Fig. 5.1c**, Bernstein polynomials of degree seven is used to approximate the continuous-time trajectory. Here it can be seen that the continuous-time curve almost perfectly follows the discrete-time curve, even in periods with rapid changes in the wind profile.

So, a higher degree of the Bernstein polynomials will result in a more accurate approximated continuous-time trajectory. On the other hand, it will increase the number of decision variables and binary commitment variables in the model, which will result in a more complex model with a higher computational time. In this case study, the continuous-time model is implemented with the use of Bernstein polynomials of degree three. This will minimize the complexity of the total model and at the same time allowing the application of C^1 continuity constraints.

5.2 The Over All Test System

The stylized three-area system contains a hydro dominated Norwegian area, a thermal dominated Northern European area and an offshore wind area in the North Sea, connected through HVDC cables. The schematic of the test system is shown in **Fig. 5.2**, where the total capacity of each area and HVDC cables are shown. The actual installed capacity of each area together with the scaled installed capacity is presented in **Table. 5.1**. How and where the values are found will be further explained in the following sections.

Area	**Capacity [MW]**	**Scaled capacity [MW]**
Thermal area	55,510.80	921.19
Hydro area	32,257.00	535.30
Offshore wind area	10,373.84	172.15
TOTAL	**98,141.64**	**1,628.64**

Table 5.1: Installed capacity vs scaled installed capacity for each area in the three-area test system.

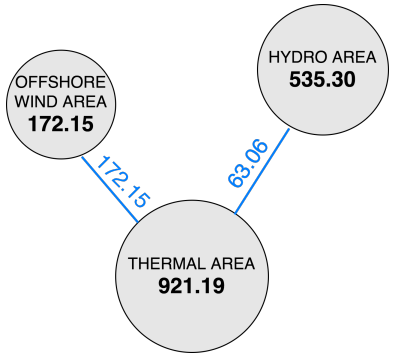

Figure 5.2: Illustration of the three-area test system

5.2.1 System Scaling Rate

The cascaded hydropower system, used as a representation of the total Norwegian hydropower system, is used as a basis for the values of the input data in the case study. To achieve a realistic system where all input data in the case study are based on real values, all data are scaled down by the system scaling rate. This scaling rate is defined as the rate between the installed capacity of the cascaded hydropower system and the total installed hydropower capacity in Norway. As written in Section 2.4.1, the total installed hydropower capacity in Norway was 32,257 MW at the end of 2019. The system scaling rate was therefore found to be:

$$SystemScalingRate = \frac{535.3\,MW}{32,257\,MW} = 0.0166. \tag{5.1}$$

This rate will be used to scale down the installed capacity of each area, as well as the net load and wind series.

5.3 Generating Units

5.3.1 Thermal Area

The Netherlands and parts of Germany, shown in **Fig. 5.3**, will in this test system represent the thermal area. The area over the red line will be used as a basis for the thermal area data. Germany is divided into two sub-systems because it is assumed that thermal power produced below the red line will be used/exported to southern parts of Europe, and not to Norway and other Northern countries. This means that only 61% of the operating thermal generators in Germany will be used for test system. Denmark was not included in the thermal area as it was difficult to find data of the thermal generators with the required resolution. This limitation should not interfere with the results as the thermal installed capacity in Denmark is relatively small compared to that of Germany and the Netherlands.

A map over the operating units for the area analysed is shown in **Fig. 5.4**, where the thermal units are divided into different categories based on their primary fuel. The orange

Figure 5.3: Picture of the thermal area used for the three-area system, which includes the Netherlands and parts of Germany (area over the read line) [27]

boxes represent fossil gas, the red boxes represent nuclear, the black boxes represent fossil hard coal, dark brown boxes represent fossil oil and the light brown boxes represent lignite/fossil brown coal [27]. Both Germany and the Netherlands have thermal generators with biomass and waste as their primary fuel. However, the production from these generators are relatively small compared to the other primary fuel categories, and were therefore neglected in the test system.

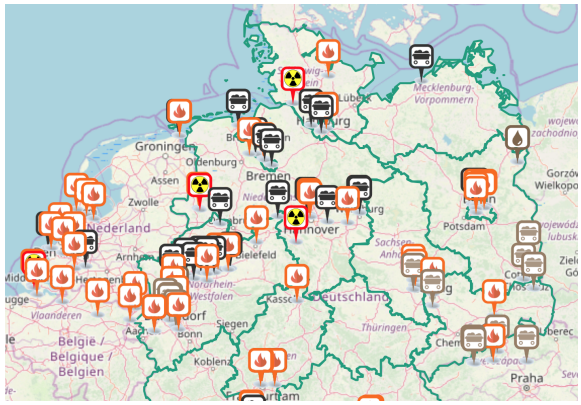

Figure 5.4: Thermal generators in Germany and Netherlands [27]

The thermal generators are defined by different technical characteristics. The parameters used for the thermal generators in the test system are installed capacity, G^{max}, minimum production, G^{min}, and the ramp rate, $R^{up/down}$. It was assumed that the ramp rate for ramping the production up and down was equal. Both the minimum production and the ramp rate will be a percentage of the installed capacity. In addition to these parameters, each thermal generator is defined by a marginal cost and costs for startup and shutdown.

The cost for a startup or a shutdown was assumed to be equal for all the thermal generators. In addition, the cost of a warm startup was used. Values for installed capacity, minimum production and the ramp rate of each thermal unit was based on values from [27] [59]. Both the minimum production and the ramp rate were found by analysing the electricity production charts. If the value of the ramp rate was found to be larger than the installed capacity, the ramp rate was assumed to be equal to the installed capacity. This means that the generator has the possibility to change its production from zero to G^{max} during one hour. The marginal cost and the costs for startup and shutdown were based on values from [6]. Data for some of the thermal generators were missing, but median values based on the other generators were used to account for this.

The installed capacity for some of the thermal generators is relatively small compared to the rest of the generators. This is typical for generators that are connected to a thermal power plant with two or more generators. In this case, as a general rule, generators with the same primary fuel and with installed capacity under 100 MW were clustered together with generators connected to the same power plant or to generators in the same geographical area. This was done in order to reduce the number of binary commitment variables and thereby reduce the problem size and corresponding run time. When two or more generators were clustered together, the value of the installed capacity was set as the sum of the installed capacities of the cluster members. For the different costs, minimum production and the ramp rate, the average value of the cluster members was used.

After clustering, the thermal area contained 104 thermal generators in total. **Table. 5.2** shows the number of units of each primary fuel category presented together with the original and the scaled installed capacity. A total list of all the thermal generators with data can be found in Appendix C.

Primary Fuel	**Number of generators**	**Installed capacity [MW]**	**Scaled installed capacity [MW]**
Fossil Gas	53	19,907.60	330.36
Fossil Hard Coal	28	17,338.00	287.72
Lignite	16	13,229.00	219.53
Nuclear	4	4,591.00	76.19
Fossil Oil	3	445.20	7.39
TOTAL	**104**	**55,510.80**	**921.19**

Table 5.2: Number of thermal generators together with original and scaled installed capacity

5.3.2 Hydropower Area

The hydropower area was based on a real Norwegian cascaded system located around Trondheim, within the pricing area NO3. The system contains 12 reservoirs and power plants with a total hydropower capacity of 535.3 MW. A detailed description of the hydropower topology can be seen in [60]. The hydropower plants are defined by different

technical characteristics, and the values for installed capacity, P^{max}, minimum production, P^{min}, and maximal reservoir capacity, V^{max}, are shown in **Table. 5.3**.

Hydropower plant	$\mathbf{P}^{max}$ [MW]	$\mathbf{P}^{min}$ [MW]	$\mathbf{V}^{max}$ [m^3]
1	26.30	10.52	0.20
2	17.95	7.18	0.10
3	37.89	15.16	0.10
4	119.60	47.84	366.70
5	19.67	7.87	43.70
6	6.78	2.71	65.00
7	27.50	11.00	4.30
8	18.40	7.36	1.20
9	36.80	14.72	94.30
10	162.00	43.90	37.30
11	37.50	15.00	582.00
12	24.90	9.96	187.00

Table 5.3: Hydropower plants characteristics

A schematic of the cascaded hydropower system can be found in Appendix B, alongside the numerical data.

5.3.3 Offshore Wind Power Area

The offshore wind area located in the North Sea was assumed to have an installed capacity equal to the installed offshore wind power capacity of Denmark, Germany and the Netherlands. The data used for the offshore wind area was based on wind data from Denmark, available in [58]. The values for the price area DK1 was used since this area borders the North Sea. There are six regions with installed offshore wind power capacity within DK1, and these regions together with the installed capacity and the number of offshore wind power generators are presented in **Table. 5.4**.

Municipality number	City	Capacity [MW]	Number of generators
813	Frederikshavn	7.60	3
741	Samsø	23.00	10
727	Odder	5.00	10
707	Norddjurs	399.60	111
665	Lemvig	45.20	12
561	Esbjerg	776.00	220
Total		**1,256.40**	**366**

Table 5.4: Offshore wind power installed capacity and number of wind turbines (January 2019)

These offshore wind power plants are clustered together as one big wind farm, with a total installed capacity of 1,256.4 MW. This installed capacity was scaled up to match the total installed offshore wind power capacity provided by Denmark, Germany and the Netherlands in the North Sea; 10,373.84 MW [20]. This rate was calculated to be 8.2568, and was used to scale the wind series. To match the installed capacity of the offshore wind area to the rest of the system, the installed capacity was scaled down with the system scaling rate in (5.1). Hence, the installed capacity of the offshore wind area was calculated be 172.15 MW.

5.4 HVDC Cables Capacities

The three-area system is connected through two HVDC cables, one between the hydro and thermal area, and one between the offshore wind and thermal area, as can be seen from **Fig. 5.2**. The capacity of the cable connecting the hydro and the thermal area was based on the total installed capacity of the two interconnectors between Norway and mainland Europe as of May 2020 and the 1400 MW Nordlink cable, which will be installed during 2020. These interconnectors were clustered together as one HVDC cable, with a total installed capacity of 3800 MW. By scaling the capacity with the system scaling rate, (5.1), the HVDC cable connecting the hydro and the thermal area was calculated to have a installed capacity of 63.06 MW. The cable between the offshore wind and the thermal area was assumed to be equal to the installed capacity of the offshore wind area. This was done to ensure no limitations on the utilization of the possible offshore wind power production. As discussed before, ramping of the power flow on the HVDC cables were not taken into account.

5.5 Load Data

Both the thermal area and the hydropower area are demand areas in the three-area test system. The load profile of the thermal area was based on real load data from ENTSO-E, where the total load profile is the sum of the load profiles in Germany and the Netherlands, available in [61]. In both Germany and the Netherlands, the is load measured on a quarterly basis. The load profile of the hydropower area was based on real load data from Nord Pool, available in [62], where the load is measured on an hourly basis.

For the hydropower area, a peak load of 75% of installed capacity was assumed. This results in a peak load of 400 MW. Since the total installed capacity of the thermal area was found by using 61% of the thermal generators in Germany, and that the total load profile for the thermal area was based on data from all of Germany, there will be a significant mismatch between the total load and the total installed capacity of the thermal area. Therefore, a peak load of 85% was assumed for the thermal area, which resulted in a peak load of 783 MW.

5.6 Wind Series

The wind series will be used as an upper limit for the offshore wind power production in the models. The data used for the wind series were based on the total real-time electricity production from offshore wind power plants within pricing area DK1 in Denmark [58]. Here the electricity production is measured every 5 minuets. The wind series were scaled by a rate of 8.2568, found in Section 5.3.3, and the system scaling rate to match the rest of the test system. After scaling the wind series, the max hourly wind production was found to be around 95% of the installed capacity of the offshore wind area. Hence, the peak offshore wind power production was assumed to be 163.54 MW. The continuous-time wind series was calculated from the data by a standard least-squares error fit to the Bernstein polynomials, explained in Section 4.3.3. For the piece-wise discrete wind series, the average quarterly values were used.

5.7 Penalty Costs

In both the discrete-time UC model and the continuous-time UC model, costs for load shedding, wind power curtailment, bypassing and spilling water are added in the objective function. The values for these costs are equal for both models, and are presented in **Table 5.5**. These values were based on an educated guess made by the author and the supervisor Christian.

Penalty	**Cost**
Wind curtailment [€/MW]	0.1
Load shedding [€/MW]	3000.0
Spilling water [€/m^3]	200.0
Bypassing water [€/m^3]	100.0

Table 5.5: Penalty costs

5.8 Water value calculations

The values used in the equation for the future cost of the hydro system was found by running a long-term hydrothermal model with the integration of offshore wind power. This simulation was done by Arild Helseth from SINTEF Energy Research.

Chapter 6

Case Studies

The proposed UC models were assessed through a case study, where two different days during 2019 were explored. One case was selected to represent the day when the water level in the reservoirs were at its minimum compared to the maximum capacity. This occurred on April 22nd, 2019. For this case, the initial reservoir volumes were set to 31.6% of the maximum reservoir volume. The second case was selected to represent the day when the water levels in the reservoirs were at its highest compared to the maximum capacity. This occurred on October 7th, 2019, and for this case, the initial reservoir volumes were set to 85.3% of maximum reservoir volume. The values for the water levels were based on measurements done by NVE, and has been shown in **Fig. 2.7**. In this thesis, the median water level measurement was used. The load data used for the two different cases were also from April 22nd, 2019 and October 7th, 2019.

For each of the two cases, the UC simulations were solved for two different sub-cases, where two different wind series were used to highlight possible UC scheduling scenarios and their impact on scheduling costs and power flows. Each case was simulated using the continuous-time UC model, and compared to the analogous discrete-time UC model simulated of the same case. In addition, the continuous-time model was used as a simulator for real-time operation to examine the specific times where the discrete-time model overestimates the flexibility of the system. This was done by fixing the binary commitment decisions in the continuous-time model to be equal to the discrete-time solution.

The two wind series used in the simulations are from January 1st, 2019, and April 22nd, 2019. The January data set was selected due to large variations in the wind series, where the possible wind power production changes rapidly between low and high production. The wind series from April was selected to investigate the impact of a more stable wind power production.

6.1 Case Solver

Both models were implemented in Pyomo and solved with CPLEX 12.10 to an absolute MIP-gap of 0.0% on a 2.4 GHz Intel Core i5 machine. The continuous-time model

was solved with the use of one additional binary variable and with a higher number of variables, equations and constraints than the discrete-time UC model. This resulted in a higher computational time for the continuous-time UC model. The computational time for each model, together with the simulation results, will be presented in Chapter 7.

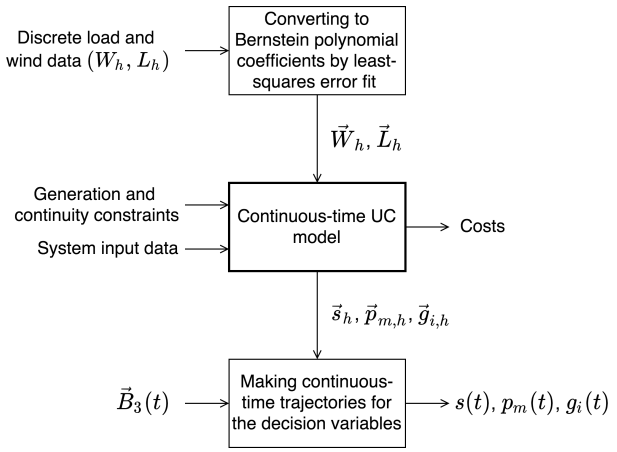

Figure 6.1: Flowchart for the continuous-time model.

A simple representation of the model structure for the continuous-time model is shown as a flowchart in **Fig. 6.1**. The flowchart contain three boxes, where each box represents one operation that needs to solved to present the solution of the continuous-time model. The first box represents the operation where the continuous-time load and wind series are calculated from the discrete data by a standard least-squares error fit to the Bernstein polynomials. The input to this box is the discrete load and wind data for all hours $h \in \mathcal{T}$, while the output is the Bernstein polynomial coefficients for the load and wind series. The second box represents the continuous-time UC model, which was implemented in Pyomo. The continuous-time UC model was formulated with generation and continuity constraints and the input to the model is the system data. The system input data includes all data for the generating units, the HVDC cables, and data for the water value cuts and coefficients. The output of the continuous-time UC model is the objective value, as well as other system operation costs, and the Bernstein polynomial coefficients for all decision variables. The Bernstein polynomial coefficients are the input to the last box, where the continuous-time trajectories are made with the use of the Bernstein polynomials of degree three. In the simple illustration, only the Bernstein polynomial coefficient vectors for offshore wind power production, hydropower production and thermal production are included, but the coefficient vectors for all other decision variables in the model are also an output of the continuous-time UC model.

The discrete-time model is presented with a simple illustration in **Fig. 6.2**. As can be seen, this flowchart is less complex than for the continuous-time model, and consist only of one box. This box represents the discrete-time UC model, which is formulated with a set of generation constraints. The input to the model is the discrete load and wind data for all hours $h \in \mathcal{T}$, as well as the system input data, which are the same as for the

continuous-time model. The output of the model is the objective value, all other system costs, and the values of all the decision variables for all hours $h \in \mathcal{T}$.

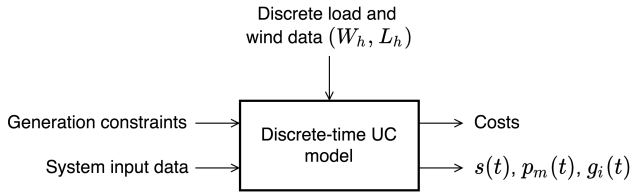

Figure 6.2: Flowchart for the discrete-time model.

6.2 Case 1: April 22nd, 2019 Load Profile

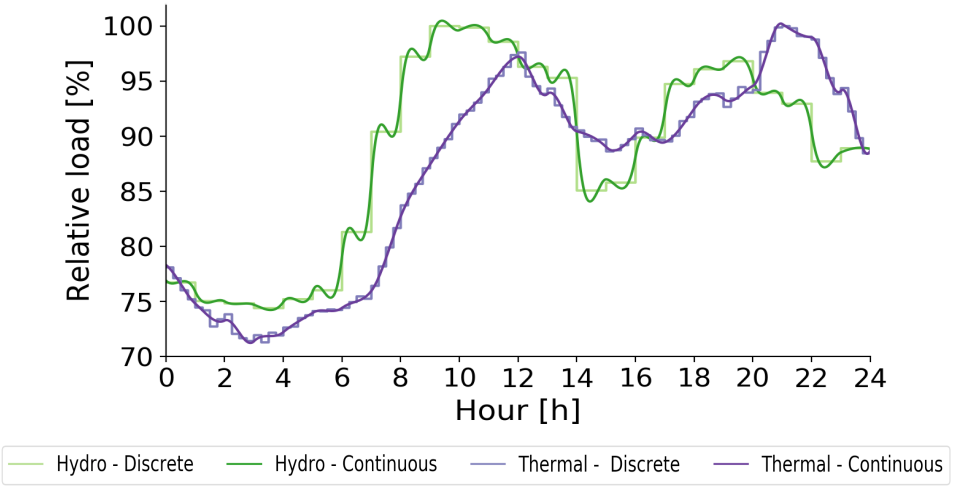

Figure 6.3: Nord Pool and ENTSO-E April 22nd, 2019 relative load profiles.

Fig. 6.3 shows the Nord Pool and the ENTSO-E April 22nd, 2019 relative load profiles for the hydro area and the thermal area [62] [61]. The hydro area load profile was scaled down by a peak load value of 400 MW, while the thermal area load profile was scaled down by a peak load value of 783 MW. For the hydro area, the discrete-time load profile is based on an hourly resolution, while the discrete-time load profile of the thermal area is based on a quarterly resolution. The approximated continuous-time load profile has moderate deviations from the discrete-time load profile for both areas, but it is seen that the deviations are more significant for the hydro area. This is because the continuous-time load profile of the hydro area was approximated with the use of fewer data points than the approximated continuous-time load profile of the thermal area. For both areas, the load is smallest in the night, around hour 0-6. In the hydro area, the load increases between hour

6 and 9, before a significant decrease occurs between hour 13 and 14. In hour 16 the load again increases, before it decreases again in the evening, around hour 20. For the thermal area, the load incremental is slower than for the hydro area. The thermal load increases between hour 7 and 12, then decreases between hour 12 and 16, before it again increases in the evening, around hour 18. For the hydro area, the peak load occurs in hour 9, while in the thermal area the peak load occurs in the first quarter of hour 21. For Case 1, the deviation between the energy demand of the two models for both areas was calculated to be lower than 0.0000%. Therefore, it was assumed that the energy demand, calculated to be 24,769.32 MWh, was equal for both models.

6.3 Case 2: October 7th, 2019 Load Profile

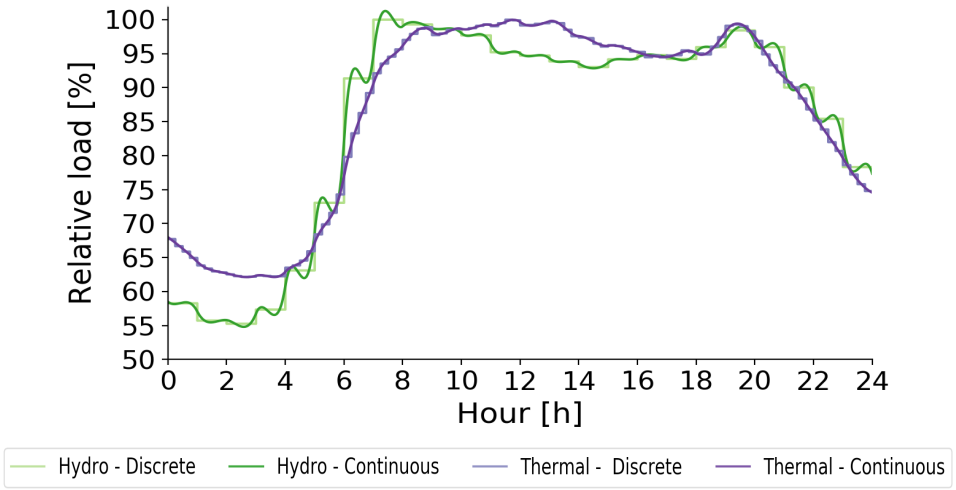

Figure 6.4: Nord Pool and ENTSO-E October 7th, 2019 relative load profiles.

Fig. 6.4 shows the Nord Pool and the ENTSO-E October 7th, 2019 relative load profiles for the hydro area and the thermal area [62] [61]. The hydro area load profile was scaled down by a peak load value of 400 MW, while the thermal area load profile was scaled down by a peak load value of 783 MW. For the hydro area, the discrete-time load profile is based on an hourly resolution, while the discrete-time load profile for the thermal area is based on a quarterly resolution. The approximated continuous-time load profile has almost no deviation from the discrete-time profile for the thermal area. The hydro area approximated continuous-time profile has moderate deviations from the discrete-time profile throughout the entire scheduling period, where the largest deviations occur in hours when the change in load between hours is significant. For both areas, the load is lowest in the morning, around hour 0-5, and then increases between hour 5 and 8. Between hour 8 and 19 the load is relatively constant, before it decreases in the evening, around hour 20, for both areas. For the hydro area, the peak load occurs in hour 7, while for the thermal area

the peak load occurs in the last part of hour 11. For Case 2, the deviation between the energy demand for the two models for both areas were calculated to be lower than 0.0000%. Therefore, it was assumed that the energy demand, calculated to be 24,510.95 MWh, was equal for both models.

6.4 Wind Series

6.4.1 Sub-case 1: January 1st, 2019 Wind Series

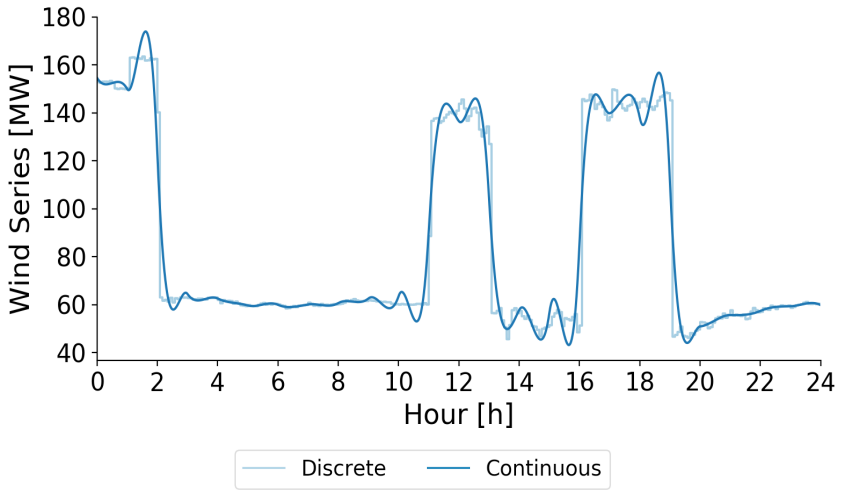

Figure 6.5: Energi Net January 1th, 2019 wind series scaled down to a maximum value of 163.54 MW for the discrete-time curve.

Fig. 6.5 shows the Energi Net Wind Series from January 1st, 2019 [58], where the discrete-time wind profile is based on a 5-min resolution. The deviation between the discrete-time profile and the approximated continuous-time profile is small in periods when the discrete-time profile is almost constant and the possible wind power production is low. Around hours when there is a fast change in the possible wind power production, the deviations between the profiles are relatively large. In hour 1, the approximated continuous-time profile will reach a peak that exceeds the maximum value of the discrete-time profile. This peak will occur due to the rapid change in the discrete-time profile between hour 1 and 2. It can be seen that such peaks also will occur in hour 10, 11, 12, 15 and 18 because of fast changes in the possible wind power production. These peaks may cause wind curtailment, which will be addressed later in Chapter 7. For Sub-Case 1, the deviation between the discrete-time wind series and approximated continuous-time wind series was calculated to be smaller than 0.0000%. Therefore, it was assumed that the total possible offshore wind power production, calculated to be 2,016.46 MWh, was equal for both models.

6.4.2 Sub-case 2: April 22nd, 2019 Wind Series

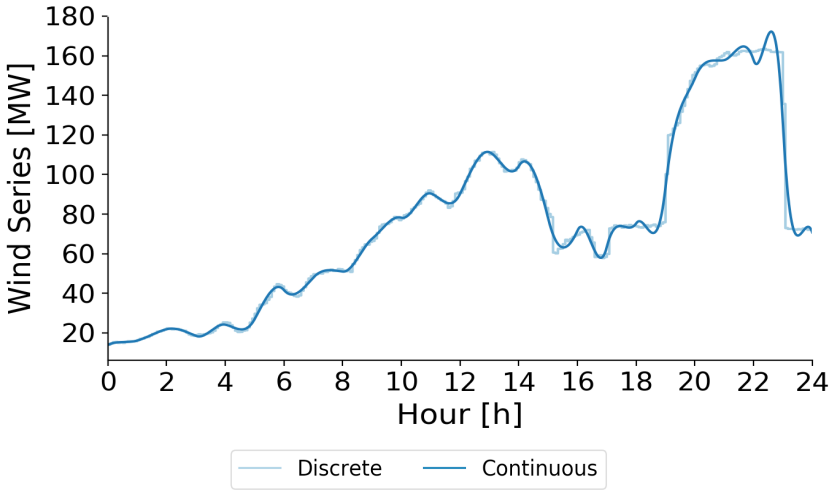

Figure 6.6: Energi Net April 22nd, 2019 wind series scaled down to a maximum value of 163.54 MW for the discrete-time curve.

Fig. 6.6 shows the Energi Net Wind Series from April 22nd, 2019 [58], where the discrete-time wind profile is based on a 5-min resolution. The deviation between the discrete-time profile and the approximated continuous-time profile is small throughout the entire scheduling interval, except for in hour 22. In hour 22 the continuous-time profile will reach a peak in order to follow the rapid change in the wind series between hour 22 and 23. The peak in the approximated continuous-time profile will exceed the maximum value of the discrete-time profile of 163.54 MW, and will cause curtailment of wind power, which will be addressed later in Chapter 7. For Sub-Case 2, the deviation between the discrete-time wind series and approximated continuous-time wind series was calculated to be smaller than 0.0000%. Therefore, it was assumed that the total possible offshore wind power production, calculated to be 1,808.29 MWh, was equal for both models.

Chapter 7

Results and Discussion

This chapter presents the results of the case study. First the results for each case are presented using plots and costs for both the discrete-time and the continuous-time model. Different aspects of the results for each case will be presented and discussed in the chapter. Then the results for the continuous-time simulator for real-time operation is presented for all cases. In the end of the chapter, a summary of the cases are presented together with an overall discussion and interpretation.

7.1 Case 1: April 22nd, 2019 Load Profile and Reservoir Volume

For Case 1.1 and Case 1.2, the load profile and reservoir volume are from April 22nd, 2019, and the initial reservoir volumes are set to 31.6% of maximum reservoir volume.

7.1.1 Case 1.1: January 1st, 2019 Wind Series

For Case 1.1, the wind series are from January 1st, 2019, to investigate the impact of rapid variations in the possible wind power production.

Scheduling results	**Discrete-time**	**Continuous-time**	**Diff.**
Computation time [sec]	144	9,532	
Total thermal related cost [€]	334,767.24	343,831.72	+2.71%
Total hydro related cost [€]	374,852.84	369,527.23	-1.42%
Total offshore wind related cost [€]	0.00	4.80	NaN
Objective value [€]	709,620.08	713,363.75	+0.53%

Table 7.1: Case 1.1: Scheduling results.

Table. 7.1 shows the total objective cost, the total operating cost for each area and the computation time for both models. In addition, the relative costs of the continuous-time model compared to the discrete-time model are shown. Both the discrete-time model and the continuous-time model were solved to optimality, meaning an absolute MIP-gap of 0.0% was reached. The discrete-time model was solved within 144 sec., while the continuous-time model used 9,532 sec. to reach a 0.0% MIP-gap. The continuous-time model forecasted a 0.53% larger total operating system cost than the discrete-time model, where the total thermal related cost was 2.71% higher and the total hydro related cost was 1.42% lower. The total thermal related cost is the operational, start and stop costs for all the operating thermal units. The total hydro related cost is the bypass cost and the future hydro system cost, while the total offshore wind related cost is the cost of curtailed wind power.

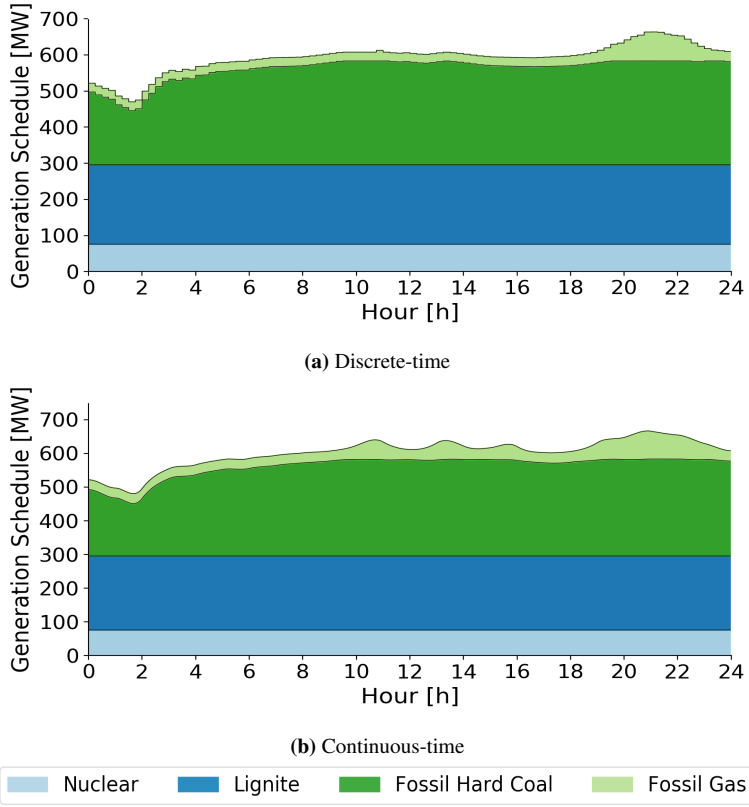

(a) Discrete-time

(b) Continuous-time

Figure 7.1: Case 1.1: Discrete-time and continuous-time thermal generation schedule.

Fig. 7.1 shows the thermal generation schedule for both the discrete-time model and the continuous-time model. From both figures it is seen that the oil-fired thermal generators were not committed during the scheduling period, and there were no startups or shutdowns of thermal generators. **Table. 7.2** shows the number of thermal generators that were

committed during the scheduling period and the costs for each primary fuel group for both models. Both nuclear and lignite generators ran at maximum capacity during the entire scheduling period for both models, while the gas-fired and the hard coal-fired generators were following the system load. All the fossil hard coal, lignite and nuclear generators in the system were operating during the entire time horizon in both models. The number of gas-fired generators committed was different in the two models, where four more gas-fired units were committed in the continuous-time model. Hence, 56 units were committed in the discrete-time model, while 60 units were committed in the continuous-time model. These results showcase that a 1.55% additional thermal production capacity lead to an additional 2.71% thermal operating cost for the continuous-time model in comparison with the discrete-time model.

	Discrete-time		Continuous-time	
Primary Fuel	**Number of units**	**Cost [€]**	**Number of units**	**Cost [€]**
Fossil Gas	8	29,465.00	12	37,963.56
Fossil Hard Coal	28	204,560.58	28	205,126.51
Lignite	16	84,437.27	16	84,437.27
Nuclear	4	16,304.39	4	16,304.39
TOTAL	**56**	**334,767.24**	**60**	**343,831.73**

Table 7.2: Case 1.1: Number of thermal units committed during the time horizon and costs.

Fig. 7.2 shows the hydropower generation schedule for both the discrete-time model and the continuous-time model. Hydropower plant 4, 5, and 7 to 10 were in operation during the entire scheduling period in both models, while the other units were turned on and off during the scheduling period to meet the system load. In the discrete-time model, 11 hydropower units were committed during the scheduling period, where startups and shutdowns occurred for units 1, 2, 3, 6 and 12 during the time horizon. The same was seen for the continuous-time model, except that one additional hydropower unit, unit 11, was committed during hour 7 to meet the rapid change in the continuous load profiles in this hour, as can be seen from **Fig. 6.3**. The number of startups and shutdowns of hydropower units were fewer in the continuous-time model than in the discrete-time model. This highlights the fact that the continuous-time model provides more flexibility to the system than the discrete-time model, and has the potential to change production fast if significant changes in offshore wind power production occur. For Case 1.1, the bypass cost was calculated to be 270.28 € in the discrete-time model, while for the continuous-time model the bypass cost was calculated to be 271.58 €. Hence, the amount of water that flows through the bypass gate was almost the same for both models. The total operating cost of the hydro system was calculated to be 374 852.84 € and 369 527.23 € for the discrete-time model and for the continuous-time model, respectively. A 1.44% higher operating hydro cost for the discrete-time model is reasonable since this model committed a 2.08% larger hydropower production than the continuous-time model.

It can be observed in **Fig. 7.2b** that the hydropower generation profiles for the continuous-

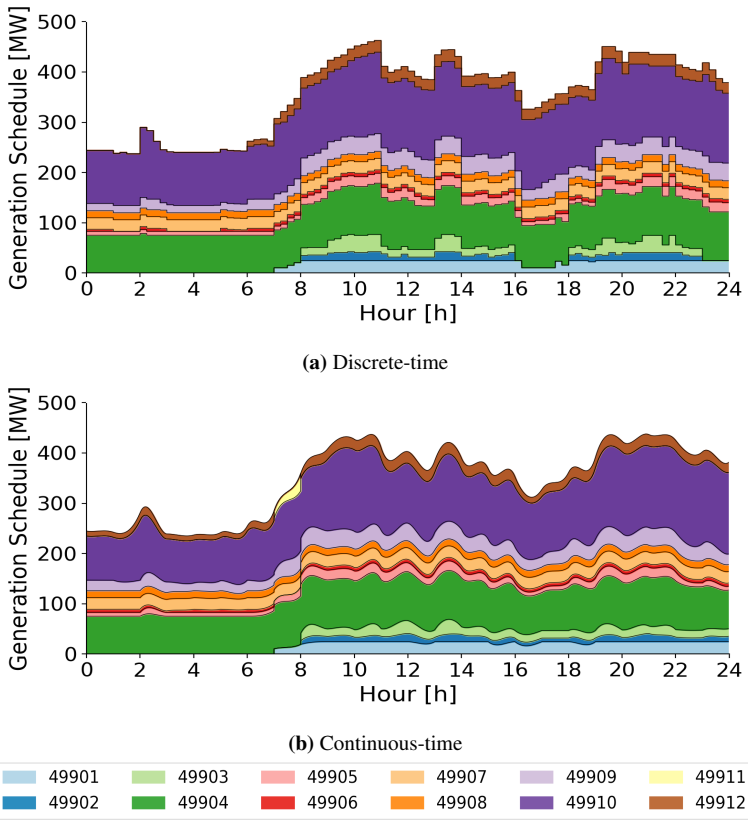

(a) Discrete-time

(b) Continuous-time

Figure 7.2: Case 1.1: Discrete-time and continuous-time hydro generation schedule.

time model have discontinuous jumps when startups or shutdowns of hydropower units occur, while the total hydropower generation trajectory is continuous. This is ensured due to the fact that the power balance constraint is C^1 continuous.

Fig. 7.3 shows the scheduled offshore wind power production and the wind curtailment for both the discrete-time model and the continuous-time model. For the discrete-time model, the amount of wind curtailment was found to be negligible, meaning that all possible wind power production was utilized. **Fig. 7.3d** shows the wind curtailment for the continuous-time model. When comparing this figure to the wind series for January 1st, 2019 in **Fig. 6.5**, it can be seen that curtailment occurs in the same hours as the approximated continuous-time wind series have peaks that exceed the discrete-time wind series. This means that the curtailment in the continuous-time model happens due to an inaccurate approximation of the continuous wind series. The total amount of wind curtailment was calculated to be 47.96 MWh, which yielded an additional cost of 4.80 € in the continuous-time model. The forecasted offshore wind power production was 2.34% higher in the discrete-time model because of the wind curtailment that occurred in the continuous-time model.

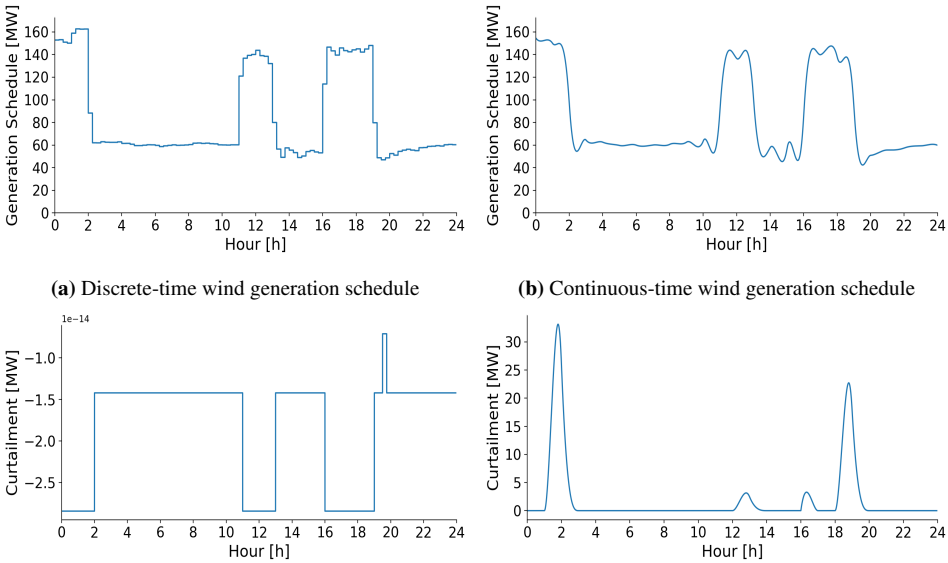

(a) Discrete-time wind generation schedule

(b) Continuous-time wind generation schedule

(c) Discrete-time wind curtailment

(d) Continuous-time wind curtailment

Figure 7.3: Case 1.1: Discrete-time and continuous-time wind generation and curtailment.

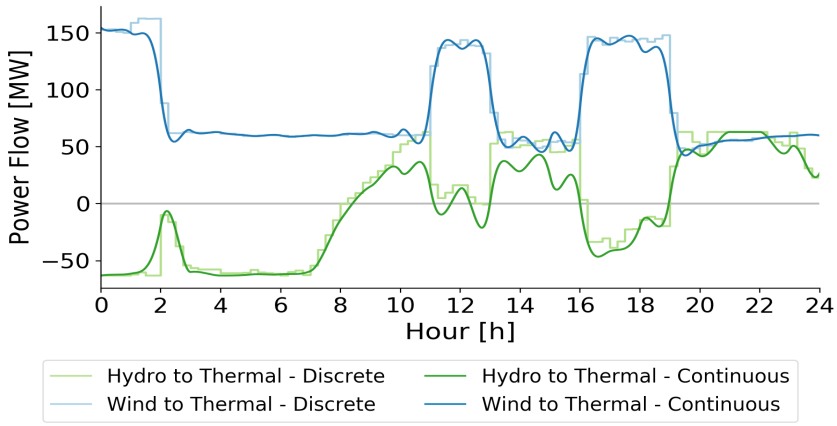

Figure 7.4: Case 1.1: Discrete-time and continuous-time power flow between areas. Negative values indicate flow in the opposite direction.

Fig. 7.4 shows the power flow between the three areas for both the discrete-time model and the continuous-time model. Negative values indicate flow in the opposite direction than labeled in the figure. The flow between the offshore wind area and the thermal area is always positive and is equal to the offshore wind power production for both models. This is reasonable since the offshore wind area has no load to cover, and all power produced will be used to cover the load in the two demand areas.

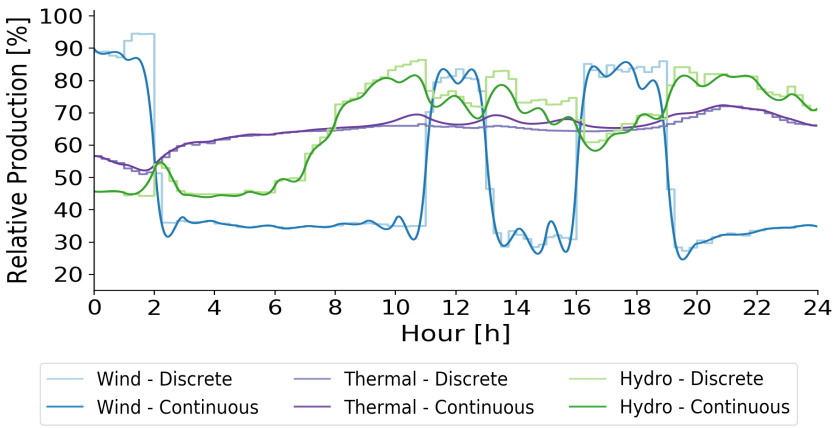

Figure 7.5: Case 1.1: Discrete-time and continuous-time relative production for each area, scaled by the respective installed capacities.

When the offshore wind power production is high or when the system load is low, it can be seen that parts of the power flow between the hydro and the thermal area are negative, which means that power is exported from the thermal area to the hydro area to cover the load in the hydropower area. It can be argued that the discrete-time model forecasted a larger flow of power than the continuous-time model during most parts of the scheduling period, where the largest deviations occurred in hour 10 and between hour 13 and 16. In these periods, more hydropower was exported to the thermal area for the discrete-time model to cover the thermal load. This result is expected, since in these periods the thermal production was lower for the discrete-time model than for the continuous-time model, hence more hydropower was needed to cover the thermal load. This can be seen from **Fig. 7.5**, which shows the relative production of each area in the test system. The generation trajectories were scaled by the installed capacity of each area.

When comparing the three generation trajectories for both models, it can be seen that the thermal production was ramped down between hour 0 and 2 because of the high offshore wind power production. When the offshore wind power production was drastically reduced between hour 1 and 2, the thermal and hydropower production were ramped up and a peak in the hydropower generation profile occurred. This result highlights the ramping limitations of the thermal generators, where it can be seen that the thermal generators do not have the ability to counteract the fast dynamics in the offshore wind power production, and the hydropower plants need to increase their production. The same pattern can also be seen in hour 13 and 19.

For both models, the thermal power production accounted for the largest share of the total production, with a share of 57.36% and 58.25% for the discrete-time model and the continuous-time model, respectively. The shares of hydropower production and offshore wind power were 34.50% and 8.14%, respectively, for the discrete-time model. For the continuous-time model, these shares were calculated to be 33.80% and 7.95%, respectively.

7.1.2 Case 1.2: April 22nd, 2019 Wind Series

For Case 1.2, the wind series are from April 22nd, 2019, to investigate the impact of a more stable possible wind power production.

Scheduling results	**Discrete-time**	**Continuous-time**	**Diff.**
Computation time [sec]	80	2,378	
Total thermal related cost [€]	324,296.66	336,241.77	+3.68%
Total hydro related cost [€]	388,795.69	380,622.96	-2.10%
Total offshore wind related cost [€]	0.00	2.28	NaN
Objective value [€]	713,092.35	716,867.02	+0.53%

Table 7.3: Case 1.2: Scheduling results.

Table 7.3 presents the total operating cost for each area and the computation time for both models. In addition, the relative costs of the continuous-time model compared to the discrete-time model are shown. Both the discrete-time model and the continuous-time model were solved to optimality. The discrete-time model was solved within 80 sec., while the continuous-time model used 2,378 sec. to reach a MIP-gap of 0.0%. The continuous-time model forecasted a 0.53% larger total system cost than the discrete-time model, where the thermal related cost was 3.68% higher and the hydro related cost was 2.10% lower than in the discrete-time model.

Fig. 7.6 shows the thermal generation trajectories for the discrete-time model and the continuous-time model. For Case 1.2, there were no oil-fired generators committed during the scheduling period, and there were no startups or shutdowns of the thermal generators. **Table 7.4** presents the number of thermal generators committed during the scheduling period together with the costs for each primary fuel group for both models.

	Discrete-time		Continuous-time	
Primary Fuel	**Number of units**	**Cost [€]**	**Number of units**	**Cost [€]**
Fossil Gas	3	7,730.99	9	22,037.05
Fossil Hard Coal	28	215,824.02	28	213,463.07
Lignite	16	84,437.27	16	84,437.27
Nuclear	4	16,304.39	4	16,304.39
TOTAL	**51**	**324,296.66**	**57**	**336,241.77**

Table 7.4: Case 1.2: Number of thermal units committed during the time horizon and costs.

All the nuclear and lignite thermal generators were in operation and will ran at maximum capacity during the entire period for both models. The production from fossil hard coal generators and fossil gas generators varied within the scheduling period, but all the fossil hard coal generators were in operation during all hours in both models. The number

of gas-fired generators committed varied between the two models, where six more gas-fired generators were in operation in the continuous-time model to cover the continuous load demand. These results showcase that an additional 2.12% thermal production capacity lead to a 3.68% additional thermal operating cost for the continuous-time model in comparison with the discrete-time model.

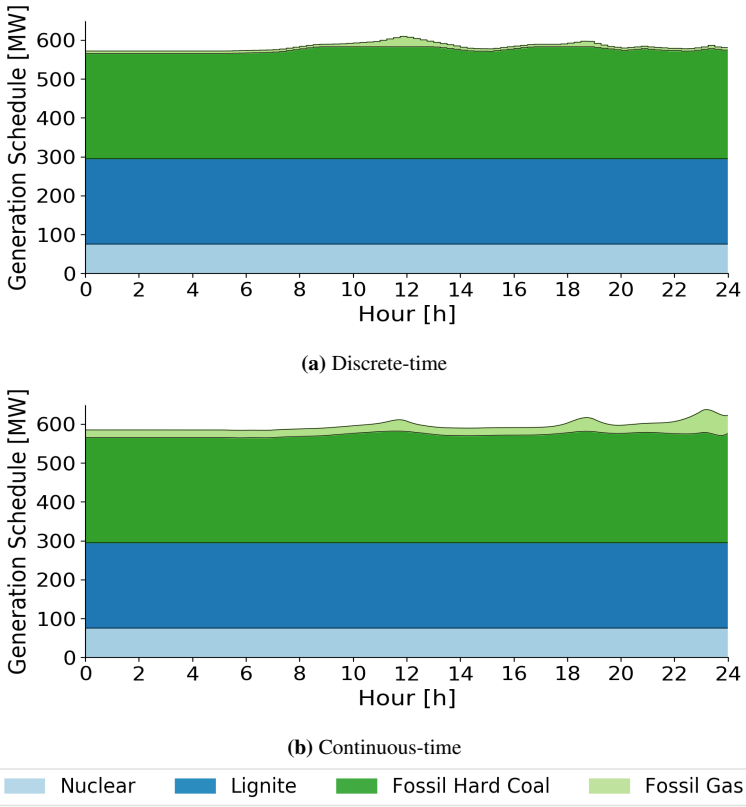

(a) Discrete-time

(b) Continuous-time

Figure 7.6: Case 1.2: Discrete-time and continuous-time thermal generation schedule.

The hydropower generation schedule for the discrete-time model and the continuous-time model are shown in **Fig. 7.7**. For the discrete-time model, hydropower plant 4 to 10 and 12 were in operation during the entire scheduling period, which can be seen in **Fig. 7.7a**. Unit 1 to 3 were committed in hour 7 and 8, due to the rapid increase in load for both areas around these hours. In hour 14 and 22, unit 2 and 3 were not in operation due to a decrease in both load profiles in these hours. In total, 11 hydropower plants were in operation during the time horizon for the discrete-time model. The continuous-time model scheduled the hydropower generation with the commitment of 12 hydropower units, where unit 11 was additionally added compared to the discrete-time model to meet the fast ramping change in the continuous load profiles in hour 6. Moreover, for this case, there were fewer startups and shutdowns of the generators in the continuous-time model.

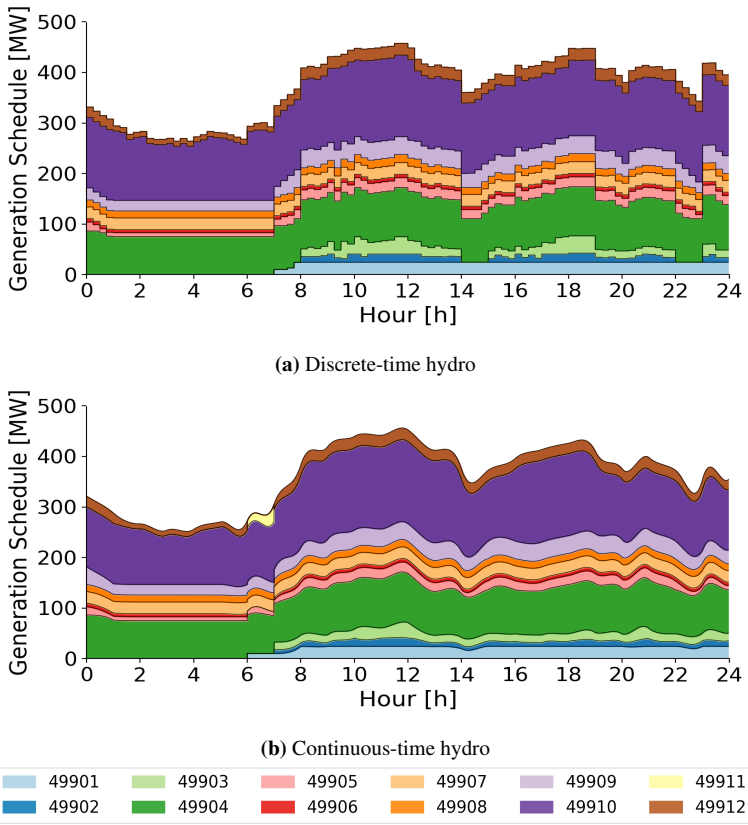

(a) Discrete-time hydro

(b) Continuous-time hydro

Figure 7.7: Case 1.2: Discrete-time and continuous-time hydro generation schedule.

For Case 1.2, the discrete-time model scheduled a 3.15% additional hydropower production in comparison with the continuous-time model. The bypass cost was calculated to be 285.07 € and 282.85 € for both the discrete-time model and the continuous-time model, respectively. The future hydro system cost was calculated to be 388 510.62 € for the discrete-time model, while in the continuous-time model this cost was calculated to be 380 340.11 €. In total, the discrete-time model scheduled a 2.15% higher hydro related cost than the continuous-time model. This is reasonable as the discrete-time model scheduled a higher hydropower production than the continuous-time model.

Fig. 7.8 shows the scheduled offshore wind power production and the wind curtailment for both models. The wind curtailment in the discrete-time model was marginal, so it can be assumed negligible. It was also seen that the curtailment became negative, which is not coherent with the implementation of curtailment. Therefore, it is safe to say that this curtailment occurred because of round-off errors in the optimization solver. This means that all possible offshore wind power was utilized in the discrete-time model. The plot of wind curtailment in the continuous-time model, in **Fig. 7.8d**, shows that the wind power was curtailed in hour 22 and 23. When comparing this plot and the continuous-time

wind generation schedule to the wind series in **Fig. 6.6**, it can be seen that the curtailment peak happens in the same hour that the approximated continuous-time wind series exceed the discrete-time wind series. So, as for Case 1.1, curtailment in the continuous-time model occurred due to an inaccurate approximation of the continuous wind series. The total amount of wind curtailment was calculated to be 22.85 MWh, which enforced an additional cost of 2.29 € in the continuous-time model. Because of the wind power curtailment in the continuous-time model, the discrete-time model scheduled a 1.28% larger offshore wind power production than the continuous-time model.

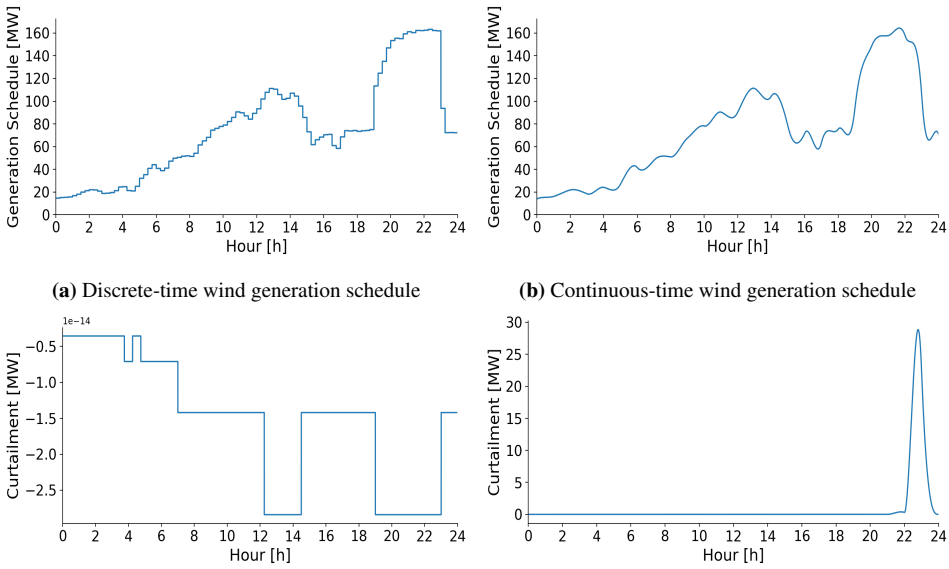

(a) Discrete-time wind generation schedule

(b) Continuous-time wind generation schedule

(c) Discrete-time wind curtailment

(d) Continuous-time wind curtailment

Figure 7.8: Case 1.2: Discrete-time and continuous-time wind generation and curtailment.

The power flow between the three areas are shown in **Fig. 7.9**, where negative values indicate a power flow in the opposite direction than labelled in the figure. As for Case 1.1, the flow of power between the offshore wind area and the thermal area was equal to the produced offshore wind power. The power flow between the hydropower area and the thermal area was higher for the discrete-time model during most parts of the scheduling period, especially at the end. This can also be seen from **Fig. 7.10**, where the relative production trajectory for each area in both models is presented. The thermal production was relatively constant during the day, except for some peaks at the end of the period in the continuous-time model. In hour 23, the wind power production decreased rapidly, which resulted in a leap in the discrete-time flow of power to the thermal area to meet the total load of the system, which can be seen in **Fig. 7.9**. When comparing this to the continuous-time model, it is evident that such an abrupt change in flow is either infeasible or very costly.

For both models, the thermal power production accounted for the largest share of the total production, with a share of 56.54% and 57.73% for the discrete-time model and the

continuous-time model, respectively. The shares of hydropower production and offshore wind power were 36.16% and 7.30%, respectively, for the discrete-time model. For the continuous-time model, these shares were calculated to be 35.06% and 7.21%, respectively.

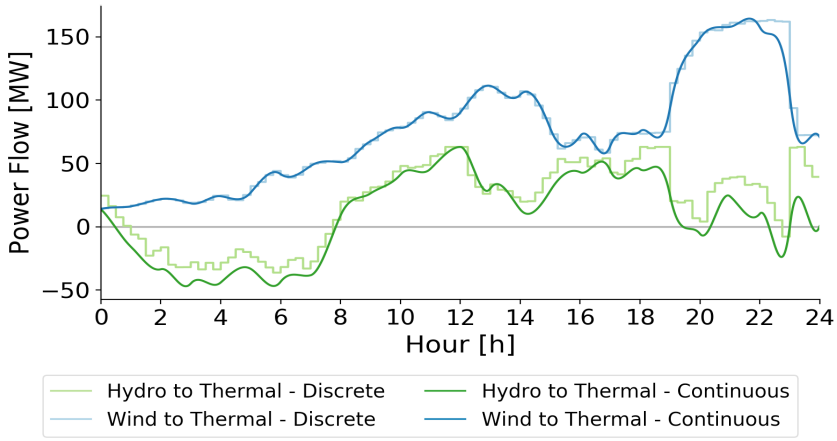

Figure 7.9: Case 1.2: Discrete-time and continuous-time power flow between areas. Negative values indicate flow in opposite direction.

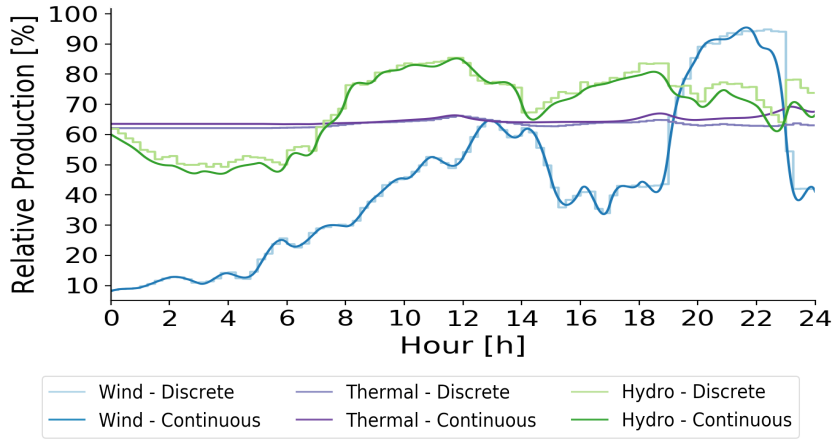

Figure 7.10: Case 1.2: Discrete-time and continuous-time relative production for each area, scaled by the respective installed capacities.

7.2 Case 2: October 7th, 2019 Load Profile and Reservoir Volume

For Case 2.1 and Case 2.2, the load profile and reservoir volume are from October 7th, 2019, and the initial reservoir volumes are set to 85.3% of maximum reservoir volume.

7.2.1 Case 2.1: January 1st, 2019 Wind Series

For Case 1.1, the wind series are from January 1st, 2019, to investigate the impact of rapid variations in the possible wind power production.

Scheduling results	Discrete-time	Continuous-time	Diff.
Computation time [sec]	32	7,414	
Total thermal related cost [€]	298,023.91	309,318.03	+3.79%
Total hydro related cost [€]	627,082.35	626,311.81	-0.12%
Total offshore wind related cost [€]	0.00	5.34	NaN
Objective cost [€]	925,106.36	935,635.18	1.14%

Table 7.5: Case 2.1: Scheduling results.

The total operating cost for each area and the computation time for both models are presented in **Table 7.5**. In addition, the relative costs of the continuous-time model compared to the discrete-time model are shown. Both the discrete-time model and the continuous-time model were solved to optimality, with a respective computation time of 32 sec. and 7,414 sec. The continuous-time model estimated a 1.14% larger operating cost than the discrete-time model, where the thermal area operating cost was 3.79% larger and the hydro area cost was 0.12% lower than in the discrete-time model.

The thermal generation trajectories in the discrete-time model and the continuous-time model are shown in **Fig. 7.11**. As for the two previous cases, there were no fossil oil generators committed during the scheduling period, and there were no startups or shutdowns of the thermal generators. The number of thermal generators in operation for each primary fuel group together with the operational cost for each group are presented in **Table 7.6**.

All nuclear, lignite and fossil hard coal generator were in operation during the entire scheduling period for both models, while the number of fossil gas generators varied between the two models. In contemporary to the two previous cases, the production from lignite generators was not at maximum capacity during the entire time horizon. Both in the discrete-time model and the continuous-time model, the production from lignite generators was ramped down at the beginning of the scheduling period when the expected offshore wind power production was high and the load of the system was low. In the continuous-time model, even some nuclear generators decreased their production in the beginning of the period. This may be because of all the other thermal generators in the system were operating at minimum production in these hours, so it was more cost-effective to ramp down some of the nuclear generators instead of shutting down other generator. The continuous-time model scheduled the thermal production with eight more fossil gas generators than

the discrete-time model, which resulted in a 1.19% higher thermal production capacity and a 3.79% higher thermal operating cost.

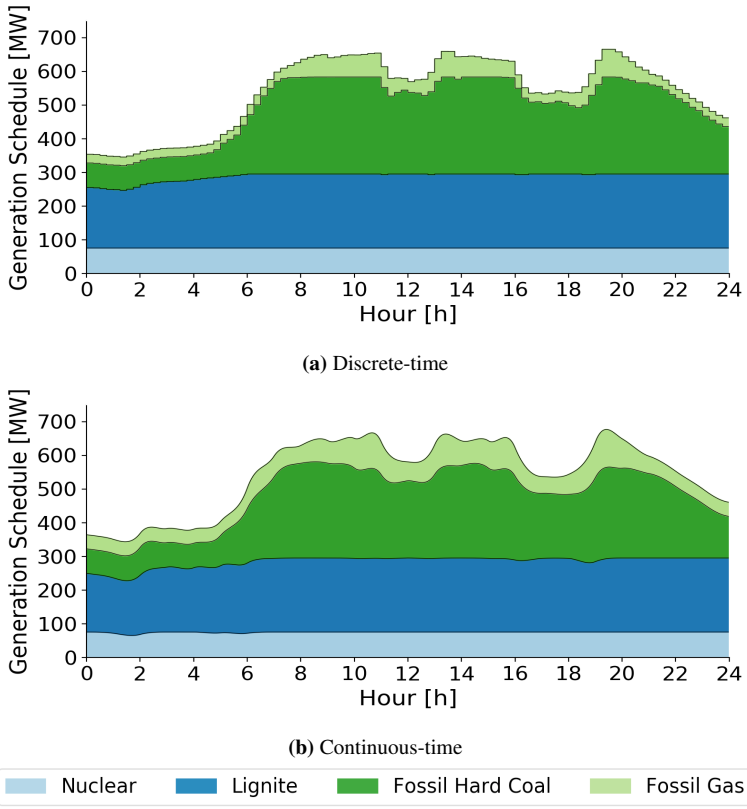

(a) Discrete-time

(b) Continuous-time

Figure 7.11: Case 2.1: Discrete-time and continuous-time thermal generation schedule.

	Discrete-time		Continuous-time	
Primary Fuel	**Number of units**	**Cost [€]**	**Number of units**	**Cost [€]**
Fossil Gas	11	39,702.61	19	60,385.78
Fossil Hard Coal	28	161,002.27	28	153,085.58
Lignite	16	81,014.64	16	79,690.40
Nuclear	4	16,304.39	4	16,156.27
TOTAL	**59**	**298,023.91**	**67**	**309,318.03**

Table 7.6: Case 2.1: Number of thermal units committed during the time horizon and costs.

Fig. 7.12 presents the discrete-time and the continuous-time hydropower schedules. There were 11 units committed during the scheduling period in both models, where hydropower plant 1, 4 and 7 to 9 were operating during the entire scheduling period. The rest of the units were turned on and off to meet the total load of the system. In both the discrete-time model and the continuous-time model, startups and shutdowns of the hydropower units mostly happened at the beginning of the scheduling period. Even though both models scheduled 11 units in operation, hydropower production was 1.09% higher in the discrete-time model than in the continuous-time model. This resulted in a future hydro system cost of 626 186.45 € for the discrete-time model. This is 0.11% higher than in the continuous-time model, which estimated the future hydro system cost to 625 517.32 €. The bypass cost was calculated to be 895.90 € and 794.49 € for the discrete-time model and the continuous-time model, respectively.

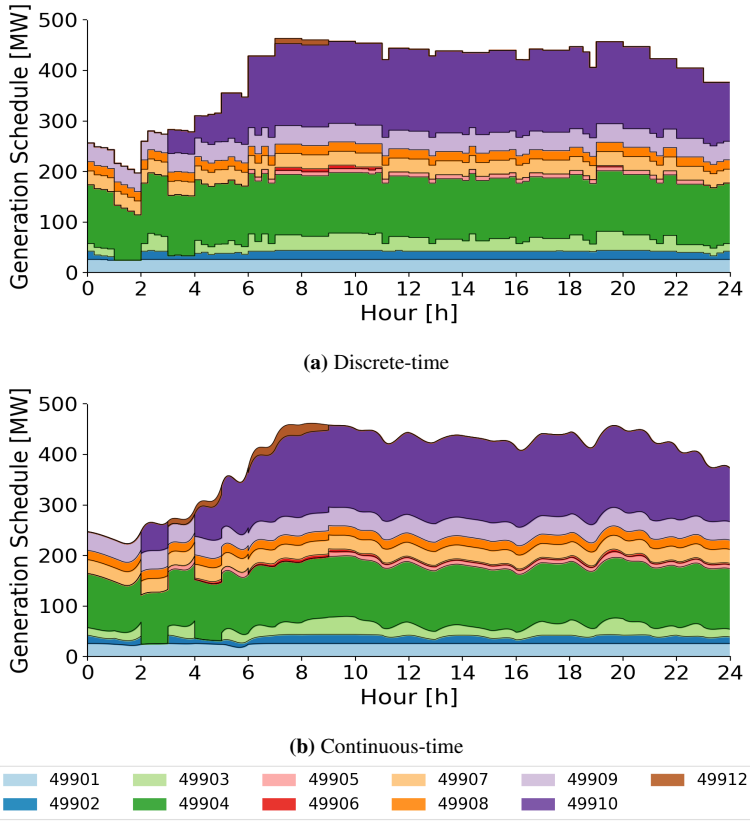

(a) Discrete-time

(b) Continuous-time

Figure 7.12: Case 2.1: Discrete-time and continuous-time hydro generation schedule.

The scheduled offshore wind power production together with curtailed wind power are presented in **Fig. 7.13**. As for the two previous cases, the discrete-time wind curtailment was assumed negligible because of the small values. The continuous-time model curtailed 53.40 MWh of offshore wind power during the day, which in turn resulted in a 2.56%

lower offshore wind power production than in the discrete-time model. As for Case 1.1, the largest peaks in the offshore wind curtailment trajectory occurred due to an approximation of the continuous wind series. In difference to Case 1.1, Case 2.1 curtailed a small amount of wind power between hour 5 and 7. For this time slot, both the load in the thermal area and the hydro area increased rapidly from around 65% to 90% of the individual maximum loads, which resulted in a rapid increase in both the hydro and thermal power production. Therefore, to meet the load of the system, some offshore wind power was curtailed. The total wind curtailment resulted in a cost of 5.34 € in the continuous-time model.

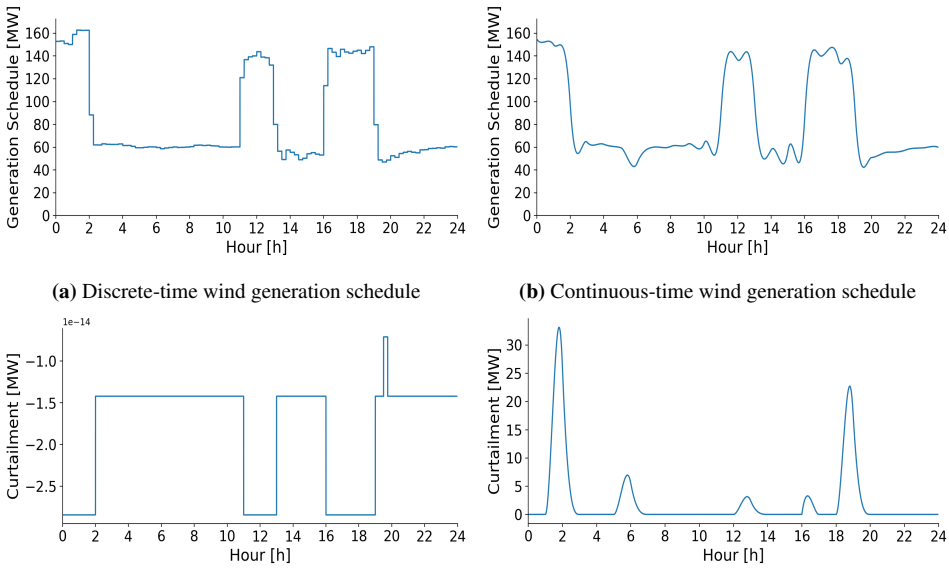

(a) Discrete-time wind generation schedule

(b) Continuous-time wind generation schedule

(c) Discrete-time wind curtailment

(d) Continuous-time wind curtailment

Figure 7.13: Case 2.1: Discrete-time and continuous-time wind generation and curtailment.

The power flow between the areas in the three-area test system for both models are shown in **Fig. 7.14**. Similar to the previous cases, the flow between the offshore wind area and the thermal area was equal to the offshore wind power production for both models. The amount of power flow from the hydro area to the thermal area was at its lowest at the beginning of the scheduling period when the offshore wind power production was high and the load was low. For the discrete-time model, the flow was in the opposite direction in some time intervals and power was exported from the thermal area to the hydro area in these periods. In the time shift between hour 1 and 2, the discrete power flow changed direction rapidly, and with a large amount of power, when the offshore wind power production was drastically reduced. When comparing the discrete power flow with the continuous power flow for this time slot, it seems like the discrete-time model overestimates the flexibility of the system to deal with fast ramping on power exchange via HVDC interconnection. From hour 5, the discrete-time model estimated a power flow at maximum capacity of the HVDC cable (63.06 MW), except in periods when there were peaks in the offshore wind power production.

From the relative production curves in **Fig. 7.15**, it is seen that thermal units ramped down their production when the offshore wind power production was high. This was done by decreasing the production from fossil gas and fossil hard coal generators, which are the most flexible thermal generators in the system. The hydropower production was also decreased in these periods, but to a smaller extent. For both models, the thermal power production accounted for the largest share of the total production, with a share of 52.84% and 53.47% for the discrete-time model and the continuous-time model, respectively. The shares of hydropower and offshore wind power production were 38.93% and 8.23%, respectively, for the discrete-time model. In the continuous-time model, these shares were calculated to be 38.51% and 8.02%, respectively.

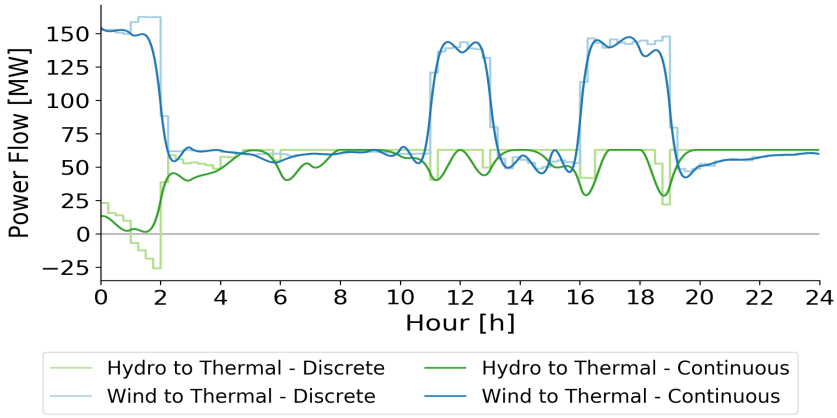

Figure 7.14: Case 2.1: Discrete-time and continuous-time power flow between areas. Negative values indicate flow in opposite direction.

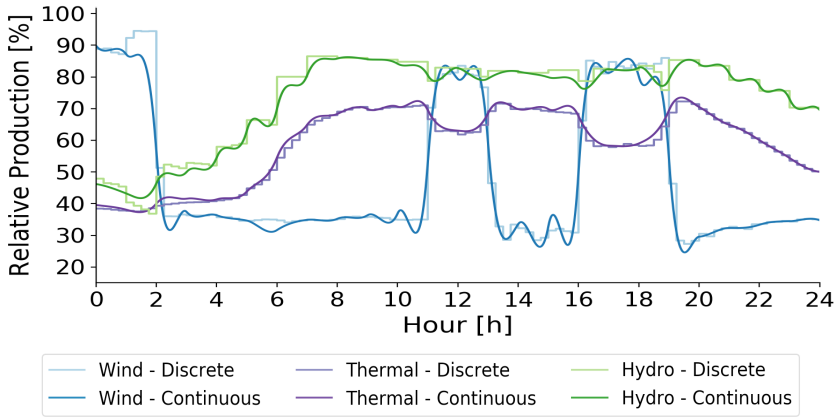

Figure 7.15: Case 2.1: Discrete-time and continuous-time relative production for each area, scaled by the respective installed capacities.

7.2.2 Case 2.2: April 22nd, 2019 Wind Series

For Case 2.2, the wind series are from April 22nd, 2019, to investigate the impact of a more stable possible wind power production.

Scheduling results	**Discrete-time**	**Continuous-time**	**Diff.**
Computation time [sec]	35	3,516	
Total thermal related cost [€]	294,807.71	298,382.98	+1.21%
Total hydro related cost [€]	630,611.25	631,083.28	+0.07%
Total offshore wind related cost [€]	0.00	3.81	NaN
Objective cost [€]	925,418.96	929,470.07	+0.44%

Table 7.7: Case 2.2: Scheduling results.

In **Table 7.7** the total operating cost for each area and the computation time for both models are presented. In addition, the relative costs of the continuous-time model compared to the discrete-time model are shown. The discrete-time model and the continuous-time model were solved to optimality, with a computation time of 35 sec. and 3,516 sec., respectively. The continuous-time model estimated an additional 0.44% total system cost in comparison with the discrete time model, where both the thermal operating area cost and the hydro area operating cost were higher than in the discrete-time model with 1.21% and 0.07%, respectively.

Fig. 7.16 shows the thermal generation trajectories for the discrete-time model and the continuous-time model. Similar to the previous cases, there were no startups or shutdowns of the thermal generators during the scheduling period, and no fossil oil generators were committed. The number of generators committed were equal in the two models, while the costs, and thereby the amount of power produced, for each primary fuel group varied, as can be seen from **Table 7.8**. In total, the continuous-time model scheduled a 0.52% higher thermal production than the discrete-time model at a 1.21% higher cost.

	Discrete-time		Continuous-time	
Primary Fuel	**Number of units**	**Cost [€]**	**Number of units**	**Cost [€]**
Fossil Gas	10	27,755.35	10	33,539.82
Fossil Hard Coal	28	166,352.64	28	164,513.25
Lignite	16	84,395.33	16	84,057.19
Nuclear	4	16,304.39	4	16,272.72
TOTAL	**58**	**294,807.71**	**58**	**298,382.98**

Table 7.8: Case 2.2: Number of thermal units committed during the time horizon and costs.

For the discrete-time model, the production from the lignite units decreased with a small amount of power in hour 5 and 22. The same happened in the continuous-time

model, where power produced from nuclear and lignite generators decreased with a small amount in hour 5 and 6. For the rest of the scheduling period, all nuclear and lignite generators were operating at the maximum capacity for both models. To ensure that the total production from the thermal units was enough to cover the load variations occurring between hour 4 and 8, and to cover the high load demand that occurred between hour 8 and 20, the fossil hard coal generators increased their production from around hour 4. In the same period, the offshore wind production increased as well. This resulted in more power in the system, and therefore nuclear and lignite generators decreased their production in hour 5 and 6 to meet the system load. This was more cost-efficient than shutting down some of the fossil gas generators, which were producing at minimum production level in this time slot. From hour 7, all nuclear and lignite generators were again operating at maximum capacity. The reduction in lignite and nuclear power production levels were higher in the continuous-time model than in the discrete-time model to maintain a continuous ramping and production trajectory for the thermal generation.

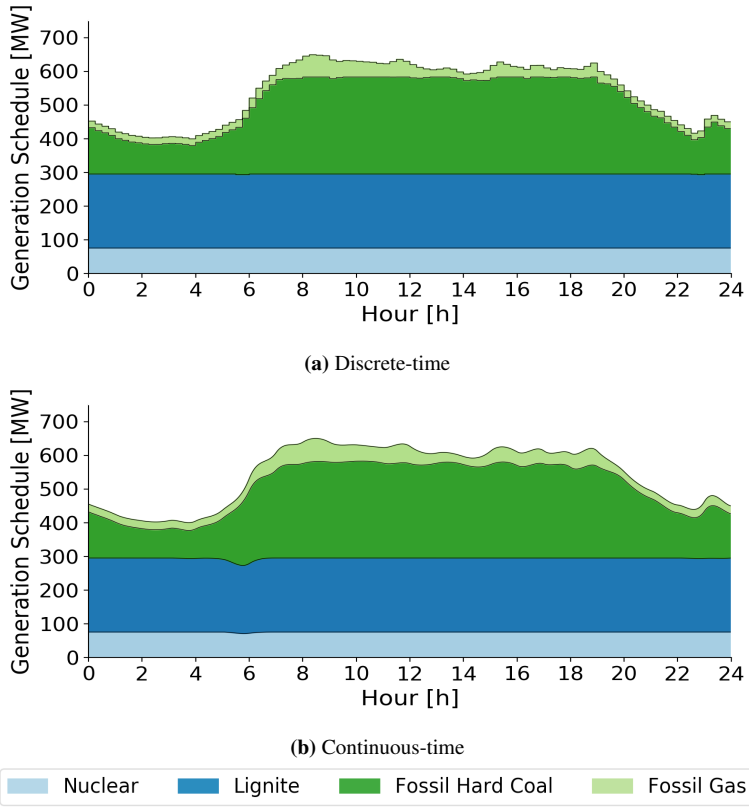

(a) Discrete-time

(b) Continuous-time

Figure 7.16: Case 2.2: Discrete-time and continuous-time thermal generation schedule.

The hydropower generation schedules for both models are presented in **Fig. 7.17**, where both models scheduled 11 hydropower units in operation during the time period.

In the discrete-time model, unit 1, 2, 4, and 7 to 9 were committed during the entire time horizon, while for the continuous-time model unit 10 was committed in addition during the entire period. The other units were turned on and off to adjust the total power produced by the hydropower units. In both models, startups and shutdowns of the hydropower units primarily happened in the beginning of the scheduling period, except for in the discrete-time model, where unit 6 was turned on at hour 17, and then turned off for the entire period. The discrete-time model estimated a hydropower production 0.30% higher than the continuous-time model. The bypass costs were calculated to be 941.56 € and 898.90 € for the discrete-time and the continuous-time models, respectively. This revealed that the amount of bypassed water was 4.75% higher for the discrete-time model. This resulted in a lower future hydro system cost for the discrete-time model compared to the continuous-time model, where the continuous-time model estimated a 0.08% higher future hydro system cost. So even though the discrete-time model scheduled a higher hydropower production, the total hydro system cost was higher in the continuous-time model.

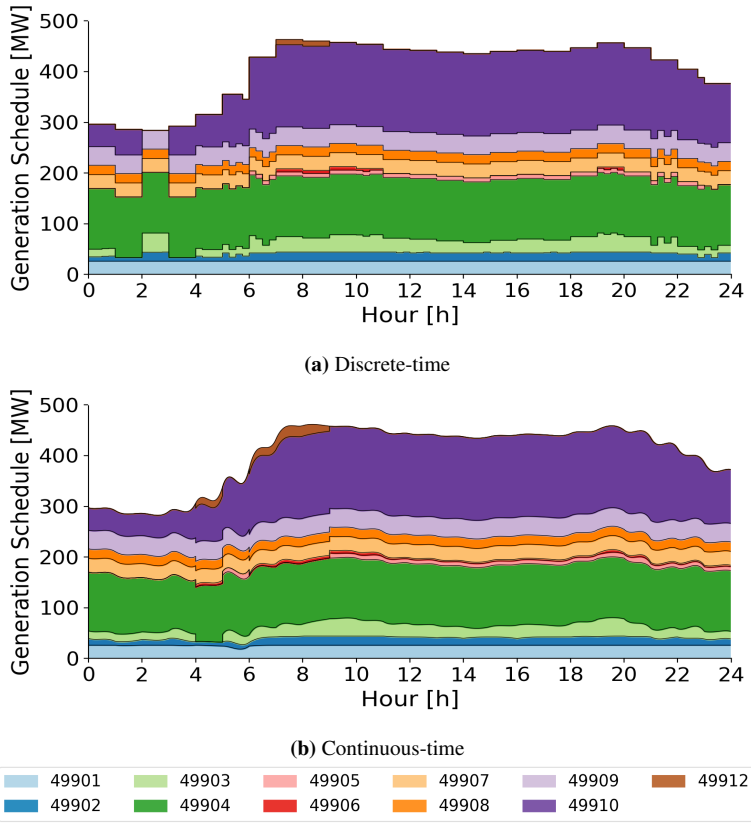

(a) Discrete-time

(b) Continuous-time

Figure 7.17: Case 2.2: Discrete-time and continuous-time hydropower generation schedule.

The offshore wind power production and wind curtailment for both models are shown in **Fig. 7.18**. As for the previous cases, the curtailed wind power in the discrete-time

model was assumed negligible, which means that all possible wind power production was utilized in the discrete-time model. Wind power curtailment for the continuous-time model occurred in hour 5 and 6, and in hour 22 and 23. The curtailment peak at the end of the scheduling period was equal to the curtailment in Case 1.2, which was caused by an inaccurate approximation of the continuous wind series. The same holds for this case. In total, 38.13 MWh of wind power was curtailed, which resulted in a cost of 3.81 € in the continuous-time model. Hence, the discrete-time model estimated a 2.15% higher offshore wind power production than the continuous-time model.

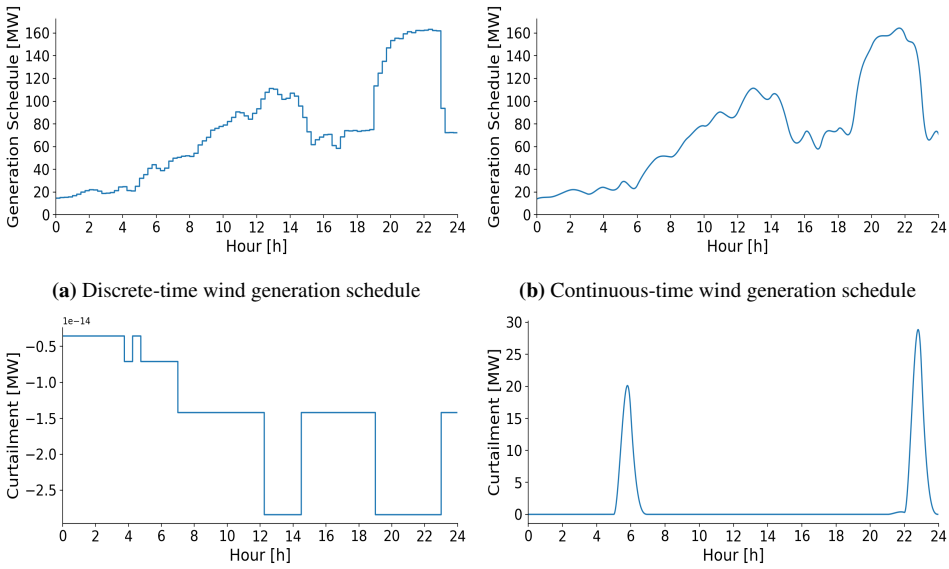

(a) Discrete-time wind generation schedule

(b) Continuous-time wind generation schedule

(c) Discrete-time wind curtailment

(d) Continuous-time wind curtailment

Figure 7.18: Case 2.2: Discrete-time and continuous-time wind generation and curtailment.

Similar to the previous cases, the flow of power between the offshore wind area and the thermal area was equal to the offshore wind power production, as can be seen from **Fig. 7.19**. The power flow between the hydro area and the thermal area was at the maximum capacity for almost the entire scheduling period for both models. For the continuous-time model, the flow of power decreased between hour 5 and 8 because of the increase in wind power and thermal power produced for these hours. The same happened in hour 22 and 23, when the load decreased.

The relative production curves for all three areas for both models are presented in **Fig. 7.20**. Overall, it was observed that the generation from hydropower and thermal power was almost the same for both models, while the offshore wind power production was different between hour 5 and 7, and in hour 22. The hydropower and the offshore wind power generation covered the peaks in the load profiles, while the thermal production increased or decreased more constantly.

For both models, the thermal power production accounted for the largest share of the total production, with a share of 52.96% and 53.24% for the discrete-time model and the

continuous-time model, respectively. The shares of hydropower and offshore wind power production were 39.66% and 7.38%, respectively, for the discrete-time model. For the continuous-time model, these shares were calculated to be 39.54% and 7.22%, respectively.

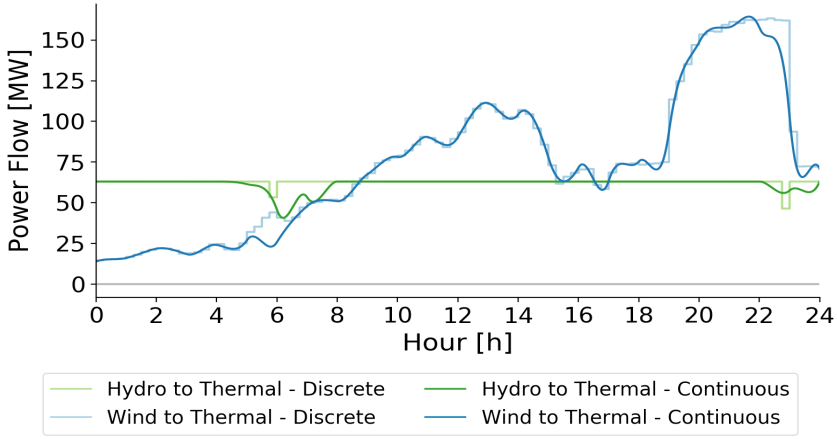

Figure 7.19: Case 2.2: Discrete-time and continuous-time power flow between areas. Negative values indicate flow in opposite direction.

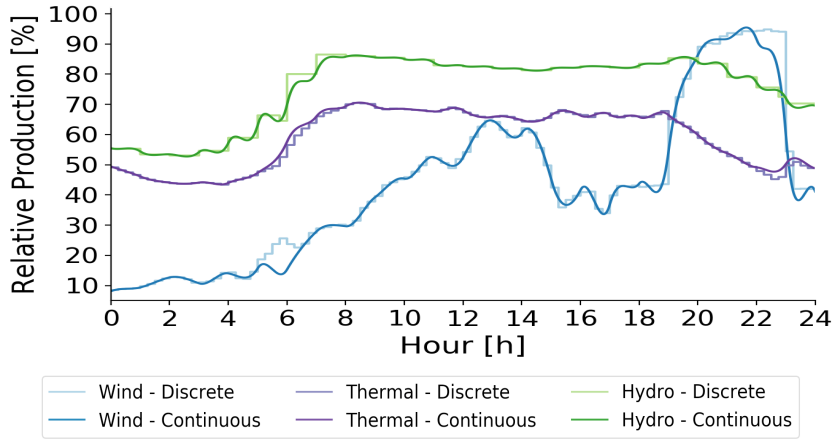

Figure 7.20: Case 2.2: Discrete-time and continuous-time relative production for each area, scaled by the respective installed capacities.

7.3 Continuous-time Model as a Simulator for Real-time Operation

From the results presented it the previous sections, it seems like the discrete-time model overestimates the flexibility of the system for some periods during the day, especially during the periods with rapid changes in production and consumption. Hence, it can be concluded that ramping scarcity in real-time balancing is the primary reason for the overestimation, which is enforced by discrete-time scheduling. To validate this conclusion, the continuous-time model was used as a simulator for real time operation. The binary commitment decisions in the continuous-time model were fixed to be equal to the commitment decisions resulting from the discrete-time solution for both the hydropower units and the thermal generators. This means that the same units were assumed to be in operation for both the discrete-time model and the continuous-time model, and at the same time intervals. This method was implemented for all cases presented in Chapter 6.

To examine the specific times where the discrete-time model underestimates the ramping capability of the system, load shedding was used as a measure of load that the system was not able to cover during fast ramping events. Hence, in time intervals where load shedding occurred, the discrete-time model underestimated the amount of power reserves needed to be in operation to cover the real-time load variations. In **Fig. 7.21** the actual load for each case are plotted versus the load that the system is capable of covering, i.e., the total produced power.

For Case 1.1, shown in **Fig. 7.21a**, a total of 33.34 MWh of load shedding took takes place during the entire scheduling period, which is 0.13% of the total load demand. The largest amount of load shedding occurred in the hydro area in periods when there were rapid changes in load. Comparing the time intervals when load shedding occurred to the hydropower generation schedule, shown in **Fig. 7.2**, it is evident that most of the load shedding occurred in time intervals when the discrete-time model shut down some hydropower units compared to the continuous-time model. Load shedding in hour 7 may be due to the fact that hydropower unit 11 was not committed in the scheduling decided by the discrete-time model. Whereas, it was committed for this hour in the continuous-time model. The same holds for hour 16, 17 and 23, where the discrete-time model shut down unit 2 and 3, while in the continuous-time model both these units were committed for these time slots. Some load shedding also occurred between hour 20 and 21 in the thermal area. In the discrete-time thermal generation schedule, all 56 generators committed in this time slot were operating at maximum capacity. This was not the case for the continuous-time model, where all of the fossil gas generators were operating below maximal capacity, and in addition four more generators were committed. Hence, the discrete-time model underestimates the number of thermal generators required to be in operation during this time slot to cover the continuous real-time load.

Fig. 7.21b shows time intervals where load shedding occurred for Case 1.2, where the total amount of load shedding was calculated to be 55.44 MWh, which is 0.22% of the total load. The majority parts of the load shedding occurred in time intervals when there were rapid changes in the load. Similar to Case 1.1, the largest amount of load shedding occurred in the hydropower area due to ramping scarcity in the real-time balancing imposed by shutdowns of generators in the discrete-time model. This happened in both

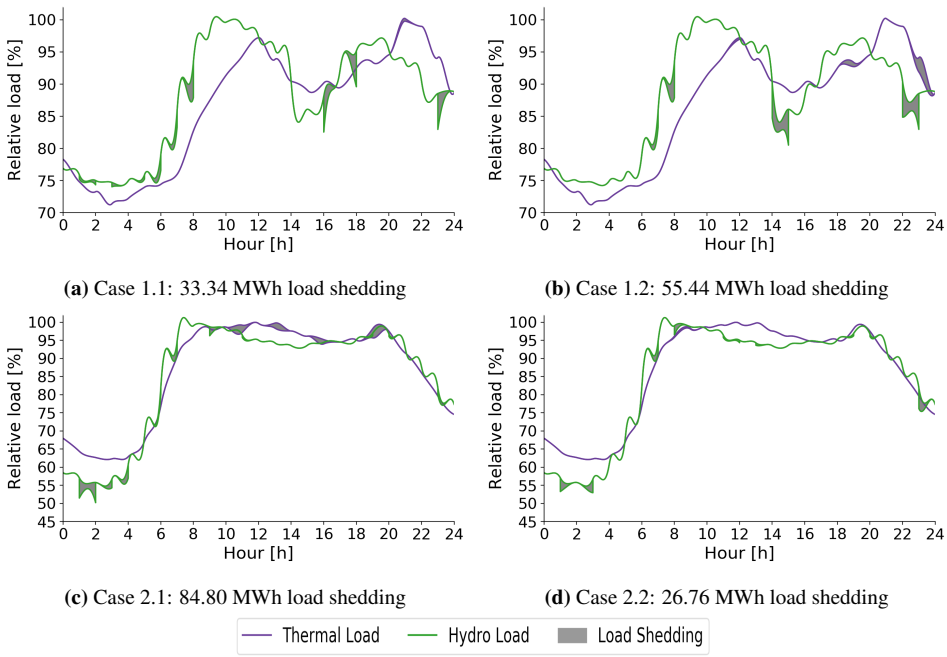

(a) Case 1.1: 33.34 MWh load shedding

(b) Case 1.2: 55.44 MWh load shedding

(c) Case 2.1: 84.80 MWh load shedding

(d) Case 2.2: 26.76 MWh load shedding

Figure 7.21: Load shedding when the continuous-time model is used as a simulator for real-time operation.

hour 14 and 22, where hydropower unit 2 and 3 were not in operation in the discrete-time model, while they were committed for these hours in the continuous-time model. The same holds for load shedding that occurred in hour 6 and 7, where the commitment decisions of unit 1, 2, 3, 6 and 11 differ in the two models. Load shedding was observed in the thermal area, mostly at the end of the scheduling period in hour 22 and 23. Here, the discrete-time model scheduled 51 generators committed, where all the generators were operating at maximum capacity, except for the three fossil gas units and three of the fossil hard coal units. Even though these generators were not producing at maximum capacity, the ramping capability of these units were not enough to cover the real-time load variations for this time slot, hence, load shedding occurred. Another contributing factor is the fact that six more generators were committed in the continuous-time model. Load shedding in the thermal area during hour 11 and 18 occurred for the same reasons.

For Case 2.1, a total of 84.80 MWh of load shedding, which is 0.35% of the total load demand, occurred during the entire scheduling period, shown in **Fig. 7.21c**. For the hydropower area, most of the load shedding occurred at the beginning of the scheduling period, in hour 1 to 4. When looking at the hydropower generation schedules in **Fig. 7.12**, this time interval represents the part of the scheduling period where the commitment of the hydropower units differ the most between the two models. The largest amount of load shedding in the hydro area occurred in hour 1, where both unit 1 and 2 were not in operation in the discrete-time model, compared to the continuous-time model. This

resulted in a large deviation between the produced hydropower in the two models for this hour, which in turn caused load shedding. For the thermal area, most of the load shedding occurred during hour 10 and 19. In these time slots, almost all generators committed in the discrete-time model were operating at maximum capacity. The total ramping of these generators were not enough to cover the continuous load, which resulted in load shedding in these hours.

For Case 2.2, shown in **Fig. 7.21d**, a total of 26.76 MWh of load shedding took place during the entire scheduling period, which is 0.11% of the total load demand. There were almost no load shedding in the thermal area, except for a small amount in hour 8. For the hydropower area, most of the load shedding occurred due to different commitment decisions for the hydropower units in the two models. In hour 1, unit 3 was not in operation, and in hour 2, unit 10 was not in operation for the discrete-time model. This differ from the continuous-time scheduling, where both of these units were committed for the respective hours. The same holds for the load shedding that occurred in hour 23, where unit 5 was not committed for the discrete-time model. There are also some load shedding in periods when there are rapid changes in the hydro area load.

7.4 Discussion and Interpretation

To assess the performance of the continuous-time UC model compared to the discrete-time UC model when large shares of offshore wind power are integrated into the power system, the results from the four different case studies will be compared and interpreted. The simulations in this thesis were based on a stylized three area-system resembling parts of Northern Europe. All the input data used for the simulations were based on real data, but adjusted to fit into the three-area test system. The economic costs were calculated based on the adjusted data, hence, the economic results do not perfectly reflect how the two different UC models perform in real-life operation of the power system. However, the results from the case study can be used as a proof of concept to highlight some important aspects of power system operation in continuous-time UC model when larges shares of IRES are integrated into the system.

Case	Model	Thermal area cost [€]	Hydro area cost [€]	Offshore wind area cost [€]	Obj. cost [€]	Diff. [€]
1.1	Discrete	334,767.24	374,852.84	0	709,620.08	
	Continuous	343,831.72	369,527.23	4.80	713,363.75	+3,743.67
1.2	Discrete	324,296.66	388,795.69	0	713,092.35	
	Continuous	336,241.77	380,622.96	2.28	716,867.02	+3,774.67
2.1	Discrete	298,023.91	627,082.35	0	925,106.36	
	Continuous	309,318.03	626,311.81	5.34	935,635.18	+10,528.82
2.2	Discrete	294,807.71	630,611.25	0	925,418.96	
	Continuous	298,382.98	631,083.28	3.81	929,470.07	+4,051.11

Table 7.9: Summary of UC costs for all cases.

The total operating cost for each of the three areas and the total system cost for each case are summarized in **Table 7.9**. The cost of covering the structural imbalances in the

system was quantified by a cost comparison to an analogous discrete-time model. For all cases simulated, the scheduling costs for the continuous-time model were higher than for the discrete-time model. This cost increase is coherent with the extra cost of balancing the sub-hourly variations in the net-load. In all cases simulated, the continuous-time model estimates a cost increase between 0.44% and 0.53% compared to the discrete-time model, except for in Case 2.1, where the cost increase was calculated to be 1.14%. For this case the thermal related cost was 3.79% higher for the continuous time model, while the hydro related cost was just 0.12% lower than in the discrete-time model. This high cost increase for Case 2.1 was due to the rapid changes in wind production series, which required fast generation ramping to balance out real-time net-load variation, especially in the thermal area.

This result can also be observed in the other cases, where the thermal related costs were higher for the continuous-time model than for the discrete-time model. In addition, the continuous-time model scheduled a higher number of gas-fired thermal generators in operation for all cases except for in Case 2.2. Even though the number of operating thermal generators were equal, the thermal related cost was higher for the continuous-time model. Hence, the simulation results demonstrated that the discrete-time model underestimated the production ramping capability of the thermal area to balance out the real-time net-load variations. In addition, it was seen that the flexible gas-fired generators were mostly used to cover peaks in the load, while the nuclear and lignite generators were operating at almost maximum capacity for all cases during the entire scheduling period. This result is coherent with the theory of the characteristics of the different thermal generators presented in Section 2.3.

There were no observed startups or shutdowns for any of the thermal units for all cases simulated. This may be due to the relatively high startup and shutdown costs for the thermal generators compared to the other costs in the system. Therefore, it was more cost-efficient to turn on or off the hydropower units to meet the total net-load of the system. From the hydropower generation schedules, it was seen that shutdowns and startups of the hydropower units will occurred during the entire scheduling period, but mostly at the beginning of the day when the load was low. The number of startups and shutdowns were higher for the discrete-time model in most cases. This means that the continuous-time model schedules more hydropower units in operation at the same time. This increases the flexibility of the hydropower scheduling in the continuous-time model compared to the discrete-time model, as an operative unit may be faster to change its production.

The initial reservoir volume was varied between the cases. Case 1.1 and Case 1.2 had an initial reservoir volume of 31.6% of maximum water level, while Case 2.1 and Case 2.2 had an initial reservoir volume of 85.3%. Hence, the two last cases had 53.7% more water available for production than the two first cases. As seen from the simulation results, this did not effect the share of total production for each area in particular. The shares of total production for each area and for each case are listed in **Table 7.10**. It could be assumed that a low initial reservoir volume would result in less hydropower production which would have to be accounted for by increasing the production from the thermal power plants. The results showed that even with low initial water levels in the reservoirs, the hydropower system was not pushed to its limit, meaning possible maximum capacity was not utilized. This result is reasonable since the theoretical total maximum load was 72.64% of installed

capacity of the overall system. If the total load peak had been adjusted to be equal to the installed capacity of the total system, it can be assumed that the overall system would have been pushed to the limit in some periods during the day, especially in periods with low reservoir volumes.

Case	Total production [MWh]	Model	Thermal area share [%]	Hydro area share [%]	Offshore wind area share [%]
1.1	24,769.32	Discrete	57.36%	34.50%	8.14%
		Continuous	58.25%	33.80%	7.95%
1.2	24,769.32	Discrete	56.54%	36.16%	7.30%
		Continuous	57.73%	35.06%	7.21%
2.1	24,510.95	Discrete	52.84%	38.93%	8.23%
		Continuous	53.47%	38.51%	8.02%
2.2	24,510.95	Discrete	52.96%	39.66%	7.38%
		Continuous	53.24%	39.54%	7.22%

Table 7.10: Summary of shares of total production for each area for all cases.

From the simulations it was also seen that the HVDC power flow for the discrete-time model was subjected to rapid flow changes in periods when the offshore wind power production either dropped or dramatically increased between time intervals. This was apparent for Case 1.2 in hour 23. This rapid flow change was not seen in the continuous-time solution, and it is evident that such an abrupt change in flow enforces structural imbalances to the system. In **Fig. 7.21**, the periods when the discrete-time model underestimated the ramping capability of the system were shown. For the variable load demand on April 22nd (Case 1.1 and Case 1.2) the discrete-time model could not schedule enough power generation ramping in periods of rapid load changes. In addition, large amounts of uncovered demand happened in periods when there were fast changes in offshore wind production. For Case 1.1, most of the load shedding occurred in the hydropower area, and it seems like the largest amounts happened in periods when the thermal area was exporting power to the hydropower area. Moreover, this was the case for some of the load shedding that occurred in Case 1.2.

For all cases, the computation time for the continuous-time model to reach optimality was much higher than for the discrete-time model. The number of decision variables and binary variables were much higher for the continuous-time model due to all decision variables were expressed with the use of four Bernstein polynomial coefficients instead of one variable for each time step. This resulted in a much more complex model, hence the computation time increased. It can be discussed how important it is to solve the models to optimality to get an impression of the differences between the two models. Allowing a MIP-gap of for example 1.0% would drastically reduce the computation time for the continuous-time model, which means that this model uses relatively much more time to go from a suitable solution to the optimal solution.

The accuracy of the approximated continuous-time curves has also been shown to have a significant impact on the scheduling results of the continuous-time model. For all cases presented, a small amount of wind power was curtailed in the continuous-time model.

From the results, it seems like this wind power curtailment occurred due to a bad approximation of the continuous-time wind series in periods when there were rapid changes in the wind power series. Even though the amount is so small that it does not effect the total costs to a great extend, this curtailment could be neglected by for example introducing bounds on the coefficients value when the continuous-time wind series were calculated from the data by a least-squares error fit to the Bernstein polynomials. In additions, a higher degree of the Bernstein polynomials would also improve the approximation, but at a cost of increased computation time.

Chapter 8

Conclusion

This master thesis has investigated the coordination of thermal and hydropower units in a power system with integration of offshore wind power. Cases of different hydrological states, wind conditions and load demand were compared and discussed. For all cases, the performance of the proposed continuous-time UC model was compared to an analogous discrete-time UC model, where the increased cost of balancing the sub-hourly variations in the net-load was found by a cost comparison between the models. All the simulations was done on a stylized three-area system resembling Northern Europe, where the total system contains a hydro dominated Norwegian area, a thermal dominated Central European area and an offshore wind area in the North Sea. The thermal area is connected to both the hydropower area and the offshore wind area through HVDC cables.

The current discrete structure of the European day-ahead electricity markets is designed for power systems with low variability in load and generation within the hours. Large-scale offshore wind power integration will challenge the current structure of the power system because of more frequent changes in the power flow and because of its variable nature. Wind power can vary quickly and unpredictably within the span of a few minutes which results in increased structural imbalances and thereby the need for more balancing reserves under real-time operation of the power system.

From the simulation results, it was seen that the discrete-time UC model scheduled fewer generators, especially thermal generators, in operation than the continuous-time model. The base load thermal power plants, i.e., nuclear and lignite power plants, was observed to run at maximal capacity during most parts of the scheduling period for both models. The number off committed flexible gas-fired generators was found to be higher for the continuous-time model to cover the peaks of the load. A higher number of flexible gas-fired generators in operation provided sufficient ramping capability to the system, and made the continuous-time model more prepared to meet unforeseen changes in net-load due to changes in offshore wind power generation.

The balancing of sub-hourly variations with the continuous-time model caused an increase in the total system cost. The cost increase is found to be between 0.44% and 1.14% of the discrete-time model system cost per day. This cost increase compensates the real-

time balancing cost in the discrete-time model. The specific periods where the discrete-time model formulation underestimated the power system ramping capability were pinpointed by fixing the binary unit commitment decisions of the continuous-time model corresponding to the optimal discrete-time commitment solution. This resulted in a total of 26.76 MWh to 84.80 MWh of load that could not be covered by the committed units from the discrete-time UC model. This issue represents an additional requirement for fast system reserves that are not procured by the discrete-time solution.

8.1 Future Work

In this master thesis it was shown that the system operating costs for the continuous-time model increased compared to the discrete-time model for a day-ahead UC schedule. In addition, it was also seen that the discrete-time UC solution does not cover all load under real-time operation, especially in periods when there were rapid changes in the net-load. This uncovered load need to be balanced under real-time operation by balancing reserves. The cost of using balancing reserves under the real-time operation of the power system was not shown in this thesis. Inclusion of this cost could however provide an improved picture of the model comparison.

Another result from the case study in this master thesis, is that the approximation of the continuous-time wind series will affect the amount of wind power that needs to be curtailed. This presents an error in the simulations that would not necessary would have been the case under real operations. So improving the approximation of the continuous-time trajectory would have made the continuous-time model more accurate.

Cascaded hydropower as a flexible energy storage technology that can be used in periods when the load is not met in real-time operation was discussed in this thesis. An energy storage technology which has gathered much attention in the field of power system research lately is battery storage. Since the need for storage capacity is increasing with the integration of IRES, it would be an interesting topic to investigate how battery storage technologies would affect the composition of the generating units in the system when a continuous-time UC formulation is used. Moreover, the transmission scarcity can impact the power system flexibility. In this thesis, internal transmission capacities were not considered in the three-area test system, which makes the system simplified and inaccurate compared to a real power systems. Imposing internal transmission capacities and divide the areas into different sub-areas would limit the exchange of power and thereby affect the imbalances in the system which need to be accounted for in real-time operation.

A summary of the proposed further work is listed below:

- Calculate the real-time operating costs for both the discrete-time model and the continuous-time model to get a better impression of the total costs of the system.
- Further improve the calculation of the approximated continuous-time trajectory of data by a least-squares error fit to the Bernstein polynomials.
- Implement ES technologies into the power system.
- Include the internal transmission capacities within each area.

Bibliography

[1] M. L. Øvstebø, "Comparison of discrete-time uc and continuous-time uc - case study," Specialization project, Norwegian University of Science and Technology (NTNU), 2019.

[2] "2030 climate & energy framework," https://ec.europa.eu/clima/policies/strategies/2030_en, accessed: 11/12-2019.

[3] H. Zsiborács, N. H. Baranyai, A. Vincze, L. Zentkó, Z. Birkner, K. Máté, and G. Pintér, "Intermittent renewable energy sources: The role of energy storage in the european power system of 2040," *Electronics (Switzerland)*, vol. 8, no. 7, jul 2019.

[4] T. Aigner, S. Jaehnert, G. Doorman, and T. Gjengedal, "The effect of large-scale wind power on system balancing in northern europe," *Sustainable Energy, IEEE Transactions on*, vol. 3, pp. 751–759, 10 2012.

[5] A. Helseth, A. Gjelsvik, B. Mo, and Ú. Linnet, "A model for optimal scheduling of hydro thermal systems including pumped-storage and wind power," *IET Gener. Transm. Distrib.*, vol. 7, no. 12, pp. 1426–1434, 2013.

[6] H. Farahmand, S. Jaehnert, T. Aigner, and D. Huertas-Hernando, "Nordic hydropower flexibility and transmission expansion to support integration of North European wind power," *Wind Energy*, vol. 18, no. 6, pp. 1075–1103, jun 2015. [Online]. Available: http://doi.wiley.com/10.1002/we.1749

[7] M. N. Hjelmeland, C. T. Larsen, M. Korpås, and A. Helseth, "Provision of rotating reserves from wind power in a hydro-dominated power system," in *2016 Int. Conf. Probabilistic Methods Appl. to Power Syst.* IEEE, oct 2016, pp. 1–7.

[8] B. P. Cotia, C. L. Borges, and A. L. Diniz, "Optimization of wind power generation to minimize operation costs in the daily scheduling of hydrothermal systems," *Int. J. Electr. Power Energy Syst.*, vol. 113, pp. 539–548, dec 2019.

[9] M. Parvania and A. Scaglione, "Unit Commitment With Continuous-Time Generation and Ramping Trajectory Models," *IEEE Trans. Power Syst.*, vol. 31,

no. 4, pp. 3169–3178, jul 2016. [Online]. Available: http://ieeexplore.ieee.org/document/7307230/

[10] R. Khatami, M. Parvania, and P. P. Khargonekar, "Scheduling and Pricing of Energy Generation and Storage in Power Systems," *IEEE Trans. Power Syst.*, vol. 33, no. 4, pp. 4308–4322, jul 2018. [Online]. Available: https://ieeexplore.ieee.org/document/8187664/

[11] K. Hreinsson, B. Analui, and A. Scaglione, "Continuous Time Multi-Stage Stochastic Reserve and Unit Commitment," in *2018 Power Syst. Comput. Conf.* IEEE, jun 2018, pp. 1–7. [Online]. Available: https://ieeexplore.ieee.org/document/8442490/

[12] R. Khatami, M. Parvania, and A. Narayan, "Flexibility Reserve in Power Systems: Definition and Stochastic Multi-Fidelity Optimization," *IEEE Trans. Smart Grid*, vol. 11, no. 1, pp. 644–654, jan 2020.

[13] C. Ø. Naversen, A. Helseth, B. Li, M. Parvania, H. Farahmand, and J. P. S. Catalão, "Hydrothermal Scheduling in the Continuous-Time Framework," dec 2019, accepted for publication in The Power Systems Computation Conference (PSCC) 2020. [Online]. Available: http://arxiv.org/abs/1912.06877

[14] M. Siemonsmeier, P. Baumanns, N. Van Bracht, M. Schönefeld, A. Schönbauer, A. Moser, O. G. Dahlhaug, and S. Heidenreich, "Hydropower Providing Flexibility for a Renewable Energy System: Three European Energy Scenarios. A HydroFlex report." https://www.h2020hydroflex.eu/wp-content/uploads/2019/01/HydroFlex-Report_Three-European-Energy-Scenarios.pdf, Tech. Rep., 2018.

[15] "What is the source of the electricity we consume?" [Online]. Available: https://ec.europa.eu/eurostat/cache/infographs/energy/bloc-3b.html

[16] A. S. Brouwer, M. Van Den Broek, A. Seebregts, and A. Faaij, "Impacts of large-scale Intermittent Renewable Energy Sources on electricity systems, and how these can be modeled," pp. 443–466, 2014.

[17] "Intermittent electricity - Energy Education." [Online]. Available: https://energyeducation.ca/encyclopedia/Intermittent{_}electricity

[18] A. report by the European Wind Energy Association, "Powering Europe: wind energy and the electricity grid," https://windeurope.org/fileadmin/ewea_documents/documents/publications/reports/Grids_Report_2010.pdf, Tech. Rep., 2010, accessed: 10/12-2019.

[19] V. Sohoni, S. C. Gupta, and R. K. Nema, "A Critical Review on Wind Turbine Power Curve Modelling Techniques and Their Applications in Wind Based Energy Systems," *Journal of Energy*, vol. 2016, p. 8519785, 2016. [Online]. Available: https://doi.org/10.1155/2016/8519785

[20] L. Ramírez, D. Fraile, and G. Brindley, "Offshore wind in Europe - key trends and statistics 2019," WindEurope, Tech. Rep., February 2020.

[21] "Offshore wind power expansion in Germany overtakes onshore for first time in 2019 — Clean Energy Wire." [Online]. Available: https://www.cleanenergywire.org/news/offshore-wind-power-expansion-germany-overtakes-onshore-first-time-2019

[22] "Offshore renewable energy industry outlook - 2030 and beyond, Interreg VB North Sea Region Programme." [Online]. Available: https://northsearegion.eu/northsee/e-energy/offshore-renewable-energy-industry-outlook-2030-and-beyond/

[23] "UK government affirms 40 GW offshore wind energy commitment — REVE News of the wind sector in Spain and in the world." [Online]. Available: https://www.evwind.es/2019/12/19/uk-government-affirms-40-gw-offshore-wind-energy-commitment/72645

[24] "Germans Agree to Increase 2030 Offshore Wind Target — Offshore Wind." [Online]. Available: https://www.offshorewind.biz/2019/09/23/germans-agree-to-increase-2030-offshore-wind-target/

[25] E. E. A. (EEA), "Development of wind farm areas in europe," https://www.eea.europa.eu/data-and-maps/figures/development-of-wind-farm-areas, accessed: 15/12-2019.

[26] J. Ambrose, "World's largest wind turbines to be built off yorkshire coast," https://www.theguardian.com/environment/2019/oct/01/worlds-largest-wind-turbines-to-be-built-off-yorkshire-coast, 1.Oct 2019, accessed: 19/12-2019.

[27] "Energy Charts." [Online]. Available: https://www.energy-charts.de/index.htm

[28] "Residual Load - energypedia.info." [Online]. Available: https://energypedia.info/wiki/Residual{_}Load

[29] P. Clerens, M. Farley, L. Jazbec, N. Kraus, and K.-D. Tigges, "THERMAL POWER IN 2030 Added Value for EU energy policy," European Power Plant Suppliers Association, Tech. Rep., 2015.

[30] M. Korpas, T. Trotscher, S. Voller, and J. O. Tande, "Balancing of wind power variations using norwegian hydro power," *Wind Engineering*, vol. 37, no. 1, pp. 79–96, feb 2013.

[31] Statkraft, "Hydropower briefly explained," https://www.statkraft.com/energy-sources/hydropower/hydropower-briefly-explained/, accessed: 17/12-2019.

[32] C. Skar, S. Jaehnert, A. Tomasgard, K. Midthun, and M. Fodstad, "Norways role as a flexibility provider in a renewable Europe," https://www.sintef.no/publikasjoner/publikasjon/?pubid=CRIStin+1721733, NTNU, SINTEF Energi AS, SINTEF Industri, Tech. Rep., 2018, accessed: 9/12-2019.

[33] "Data from the power system — Statnett." [Online]. Available: https://www.statnett.no/en/for-stakeholders-in-the-power-industry/data-from-the-power-system/{#}hydrological-data

[34] “Electricity Production,” https://energifaktanorge.no/en/norsk-energiforsyning/kraftproduksjon/#hydropower, 2019, accessed: 9/12-2019.

[35] “Vannkraft - NVE.” [Online]. Available: https://www.nve.no/energiforsyning/kraftproduksjon/vannkraft/?ref=mainmenu

[36] B. M. Barrie, “The Development of cross border interconnection and trading,” *Global Energy Interconnection*, vol. 2, no. 3, pp. 254–263, jun 2019. [Online]. Available: https://linkinghub.elsevier.com/retrieve/pii/S209651171930060X

[37] “The North Seas Countries’ Offshore Grid Initiative (NSCOGI) — European MSP Platform.” [Online]. Available: https://www.msp-platform.eu/practices/north-seas-countries-offshore-grid-initiative-nscogi

[38] A. Buatois, M. Gibescu, B. Rawn, and M. Meijden, “Analysis of north sea offshore wind power variability,” *Resources*, vol. 3, pp. 454–470, 05 2014.

[39] C. Kjaer, “The North Sea offshore grid-a distant dream or soon reality?” European Wind Energy Association (EWEA), Tech. Rep., accessed: 9/12-2020. [Online]. Available: https://www.statkraft.com/globalassets/old-contains-the-old-folder-structure/documents/kjaer-29nov10_tcm9-12386.pdf/

[40] “Royal opening of Skagerrak 4 - Nexans.” [Online]. Available: https://www.nexans.no/eservice/Norway-en/navigatepub{_}142640{_}-34274/Royal{_}opening{_}of{_}Skagerrak{_}4.html

[41] J. Skog, K. Koreman, B. Pääjärvi, and T. Andersröd, “The norned hvdc cable link–a power transmission highway between norway and the netherlands,” *ENERGEX 2006, Stavanger, Norway*, 01 2006.

[42] “Norwegian-German power cable being installed — Statnett.” [Online]. Available: https://www.statnett.no/en/about-statnett/news-and-press-releases/News-archive-2018/norwegian-german-power-cable-being-installed/

[43] “North Sea Link — Statnett.” [Online]. Available: https://www.statnett.no/en/our-projects/interconnectors/north-sea-link/

[44] “Ramping — Nord Pool.” [Online]. Available: https://www.nordpoolgroup.com/trading/Day-ahead-trading/Ramping/

[45] T. Haugland, G. Doorman, and J. Hystad, “Structural imbalances in the nordic power system — causes, future expectations and remedies,” 05 2014, pp. 1–5.

[46] “System operations and market development plan 2017-2021, executive summary,” https://www.statnett.no/contentassets/4c9e014c155f4dd98949502d65c9e6bf/executive-summary-system-operations-and-market-development-plan-2017-2021.pdf, accessed: 9/12-2019.

[47] T. C. Group, "Capacity adequacy in the Nordic electricity market – Nordic Energy Research," https://www.nordicenergy.org/publications/capacity-adequacy-in-the-nordic-electricity-market/, Nordic Energy Research, Tech. Rep., 28. Aug 2015.

[48] B. Knueven, J. Ostrowski, and J.-P. Watson, "On Mixed Integer Programming Formulations for the Unit Commitment Problem," http://www.optimization-online.org/DB_FILE/2018/11/6930.pdf, Tech. Rep., accessed: 1/6-2020.

[49] B. Zhou, G. Geng, and Q. Jiang, "Hydro-Thermal-Wind Coordination in Day-Ahead Unit Commitment," *IEEE Transactions on Power Systems*, vol. 31, no. 6, pp. 4626–4637, nov 2016.

[50] J. Wang, M. Shahidehpour, and Z. Li, "Security-constrained unit commitment with volatile wind power generation," *IEEE Transactions on Power Systems*, vol. 23, no. 3, pp. 1319–1327, 2008.

[51] F. Bouffard and F. D. Galiana, "Stochastic security for operations planning with significant wind power generation," *IEEE Transactions on Power Systems*, vol. 23, no. 2, pp. 306–316, may 2008.

[52] R. Villanueva, P. C. d. Granado, I. Oleinikova, and H. Farahmand, "A minute-to-minute unit commitment model to analyze generators performance," in *2019 16th International Conference on the European Energy Market (EEM)*, Sep. 2019, pp. 1–6.

[53] A. Helseth, B. Mo, A. L. Henden, and G. Warland, "Detailed long-term hydro-thermal scheduling for expansion planning in the Nordic power system," *IET Generation, Transmission and Distribution*, vol. 12, no. 2, pp. 441–447, jan 2018.

[54] F. Kochman, "Bernstein polynomials and Milnor algebras," *Proceedings of the National Academy of Sciences of the United States of America*, vol. 73, no. 8, p. 2546, 1976.

[55] E. H. Doha, A. H. Bhrawy, and M. A. Saker, "Integrals of Bernstein polynomials: An application for the solution of high even-order differential equations," *Applied Mathematics Letters*, vol. 24, no. 4, pp. 559–565, apr 2011.

[56] "Least Squares Method Definition," accessed: 2020-06-12. [Online]. Available: https://www.investopedia.com/terms/l/least-squares-method.asp

[57] A. Marco and J.-J. Martínez, "Polynomial least squares fitting by using the bernstein basis," 06 2015.

[58] https://www.energidataservice.dk/en/dataset/electricityprodex5minrealtime/resource_extract/06380963-b7c6-46b7-aec5-173d15e4648b, accessed: 2/3-2020.

[59] "Capacity," https://www.eex-transparency.com/power/de/production/capacity/, accessed: 10/2-2020.

[60] C. Ø. Naversen, H. Farahmand, and A. Helseth, "Accounting for reserve capacity activation when scheduling a hydropower dominated system," *Int. J. Electr. Power Energy Syst.*, vol. 119, p. 105864, jul 2020.

[61] https://transparency.entsoe.eu/load-domain/r2/totalLoadR2/show, accessed 2/2-2020.

[62] https://www.nordpoolgroup.com/Market-data1/Power-system-data/Consumption1/Consumption/NO/Hourly1/?view=table, accessed 2/2-2020.

Appendix A

Paper submitted to the EEM 2020 conference

The following paper have been submitted June 15th to the International Conference on the European Energy Market 2020 (EEM) in Sweden, Stockholm 16.-18.September 2020. Due to the restrictions imposed by SARS-CoV-2, the presentation of the paper will be held in a virtual conference taking place 16.-18.September 2020.

Continuous-time scheduling of a hydrothermal system with integration of offshore wind power

Mari Lund Øvstebø*†, Christian Øyn Naversen*, Arild Helseth‡ and Hossein Farahmand*
*Department of Electric Power Engineering, NTNU – Trondheim, Norway
‡Department of Energy Systems, SINTEF Energy Research – Trondheim, Norway
†Corresponding author: mariovs@stud.ntnu.no

***Abstract*—In this work, a continuous-time unit commitment formulation of a hydrothermal system with integration of offshore wind power is used to model the North European system operation. The cost of covering the structural imbalances in the system is quantified by a cost comparison to an analogous discrete-time model. If the discrete-time unit commitment is implemented for real-time operation, 55 MWh (0.22%) load shedding should be introduced since the demand in periods with high net-load ramping cannot be met. The simulation results demonstrate that the proposed framework reduces system balancing cost and the events of ramping scarcity in the real-time balancing.**

***Index Terms*—Continuous-time optimization, Hydrothermal scheduling, Offshore wind power, Unit commitment**

I. Introduction

A significant amount of offshore wind power is expected to be integrated into the European power system in the coming years [1]. The variable nature of wind power generation challenges the security of the power system as the flexibility of conventional generators are pushed to their limits. Cascaded hydropower is an existing flexible energy storage technology which can provide energy and flexibility on a system scale, and the Nordic countries have considerable amounts of hydropower installed in their current power systems. Several high voltage direct current (HVDC) cables between Norway and continental Europe (Netherlands and Denmark) have been constructed in recent years, and new interconnectors to Germany and Great Britain are under construction. The increased transmission capacity makes it possible to use Norwegian hydropower resources to help balance the wind power in the North European power system. Hydrothermal coordination in the presence of uncertain wind power generation has been studied in the literature, which includes both models with long time horizons [2]–[5] and short-term studies [6].

The discrete structure of the European day-ahead electricity markets cannot prevent the occurrence of a mismatch between the market cleared volumes and the actual production and consumption. These structural imbalances must be balanced in real-time by activating procured reserve capacity. As wind power can vary quickly and unpredictably within the span of a few minutes, the structural imbalances and need for balancing can be worsened by a high wind power penetration. Continuous-time optimization is a way of formulating the standard unit commitment and economic dispatch problems with continuously varying time-dependent variables and input data, originally formulated for a purely thermal system in [7]. The continuous-time framework has since been extended to incorporate energy storage technology in [8], and multi-stage stochastic unit commitment and reserve scheduling models are developed in [9] and [10]. In previous work, we have derived the formulation of the cascaded hydropower constraints in the continuous-time framework [11]. This paper extends the model presented in [11] to include wind power generation. The main contributions of the paper are:

- Quantifying the cost of structural imbalances in a test system resembling the Northern European power system by comparing the costs obtained by a continuous-time unit commitment model and an analogous discrete-time model.
- Identifying specific periods where the discrete-time model overestimates the flexibility of the system. This is done by simulating operation with a continuous-time model, setting the binary commitment decisions equal to the discrete-time solution.

Section II defines the continuous-time model in detail, while the case study and results are presented in Section III. A concluding summary is found in Section IV.

II. Model

The mathematical formulation of the continuous-time model is based on [11]. In this paper, the model is extended to include offshore wind power, hence constraints for wind power production and wind curtailment are added to the model.

A. Continuous-time optimization framework

The continuous-time optimizations framework directly models sub-hourly variations by representing all time-varying data and variables as polynomials of time, which allows ramping and other inter-temporal constraints to be enforced continuously. Several spline models can be used to approximate the continuous-time trajectory curve of a data set, where the accuracy of the spline model is dependent on the order of the basis. A convenient spline model is the Bernstein polynomials, where the time dependent decision variables will be defined by using the Bernstein polynomials of degree n, which form a basis for any polynomials of degree equal or less than n on the interval $t \in [0, 1]$. For a given time interval $h \in \mathcal{T}$ with length δ_h, a time-varying decision variable $x(t)$ can be expressed as:

$$x(t) = \mathbf{x}_h^T \cdot \mathbf{B}_n\left(\frac{t - T_h}{\delta_h}\right), \quad T_h \le t \le T_{h+1}, \tag{1}$$

where $T_h = \sum_{i<h} \delta_i$ is the start time of interval h, $\mathbf{x}_h$ is a vector of $n+1$ Bernstein polynomial coefficients and $\mathbf{B}_n(t)$ is the vector of Bernstein polynomials of degree n. This definition gives a piece-wise polynomial description of time-dependent variables where the polynomial coefficients $\mathbf{x}_h$ become the decision variables in the optimization problem. Choosing Bernstein polynomials of degree zero recovers the usual discrete-time formulation of piece-wise constant variables.

In this paper, the Bernstein polynomials of degree three will be used as a basis for each time interval h:

$$\mathbf{B}_3(t) = \left[(1-t)^3,\ 3t(1-t)^2,\ 3t^2(1-t),\ t^3\right]. \tag{2}$$

This degree of freedom allows the application of C^1 continuity constraints between time intervals without drastically increasing the number of decision variables in the model. The C^1 continuity constraints can be expressed with the use of the Bernstein coefficients of the decision vector $\mathbf{x}$, where the coefficients can be labeled as $\mathbf{x}^i$ for $i \in \{0,1,2,3\}$. With this in mind, the continuity constraints can be expressed as:

$$\mathbf{x}_h^3 = \mathbf{x}_{h+1}^0 \qquad \forall h \in \mathcal{T}\backslash\{N\} \tag{3}$$

$$\mathbf{x}_h^3 - \mathbf{x}_h^2 = \mathbf{x}_{h+1}^1 - \mathbf{x}_{h+1}^0 \qquad \forall h \in \mathcal{T}\backslash\{N\}. \tag{4}$$

The result of integrating and differentiating $\mathbf{B}_n(t)$ can be represented by Bernstein polynomials of degree $\mathbf{B}_{n+1}(t)$ and $\mathbf{B}_{n-1}(t)$, respectively. These relationships are described by the linear matrices $\mathbf{K}$ and $\mathbf{N}$ for $\mathbf{B}_3(t)$ in eqs. (5) and (6). Another useful relation is the definite integral of the polynomials over the whole interval, shown in eq. (7).

$$\dot{\mathbf{B}}_3(t) = \mathbf{K} \cdot \mathbf{B}_2(t) \tag{5}$$

$$\int \mathbf{B}_3(t)dt = \mathbf{N} \cdot \mathbf{B}_4(t) \tag{6}$$

$$\int_0^1 \mathbf{B}_3(t)dt = \frac{1}{4} \cdot \mathbf{1} \tag{7}$$

These properties, together with the convex hull property, are some of the main reasons for using Bernstein polynomials in the continuous-time optimization framework. The convex hull property makes it possible to impose inequality constraints on the decision variable $x(t)$ by directly bounding the coefficient $\mathbf{x}_h$. For a more detailed introduction to continuous-time optimization in power systems, the reader is referred to for instance [7].

B. Mathematical formulation of continuous-time UC

1) Thermal constraints: The following constraints are defined for all thermal units $i \in \mathcal{I}$ over time intervals $h \in \mathcal{T}$. $u_i(t)$, $SU_i(t)$ and $SD_i(t)$ are binary variables describing the commitment status, startup and shutdown of thermal generator i, respectively. Constraints (8) and (9) ensure that the thermal generator can ramp up the production,$g_i(t)$, from zero to above G_i^{min}, or ramp down production to zero, during time interval h. This smooth ramping of the production is necessary when the continuity constraints for the thermal production variable will be applied in II-B4. Limitations on the derivative $\dot{g}_i(t)$ are imposed in (10) and (11) such that the ramping of the thermal production stays within specified limits R_i^u and R_i^d by utilizing property (5). When there is a startup or a shutdown, the ramping limit is increased to G_i^{max}. Constraints (12) and (13) counts the number of startup and shutdown events.

$$G_i^{min}\mathbf{u}_{i,h} \le \mathbf{g}_{i,h} \le G_i^{max}\mathbf{u}_{i,h} \tag{8}$$

$$\mathbf{u}_{i,h} = [u_{i,h},\ u_{i,h},\ u_{i,h+1},\ u_{i,h+1}]^T \tag{9}$$

$$\frac{1}{\delta_h}\mathbf{g}_{i,h}^T \cdot \mathbf{K} \le (R_i^u + (G_i^{max} - R_i^u)SU_{i,h})\mathbf{1}^T \tag{10}$$

$$\frac{1}{\delta_h}\mathbf{g}_{i,h}^T \cdot \mathbf{K} \ge -(R_i^d + (G_i^{max} - R_i^d)SD_{i,h})\mathbf{1}^T \tag{11}$$

$$SU_{i,h} - SD_{i,h} = u_{i,h+1} - u_{i,h} \tag{12}$$

$$SU_{i,h} + SD_{i,h} \le 1 \tag{13}$$

$$u_{i,h}, SU_{i,h}, SD_{i,h} \in \{0,1\} \tag{14}$$

2) Hydropower constraints: The constraints from (15) to (30) are added to the optimization problem for the hydro area and are defined for all hydropower plants $m \in \mathcal{M}$ over time intervals $h \in \mathcal{T}$.

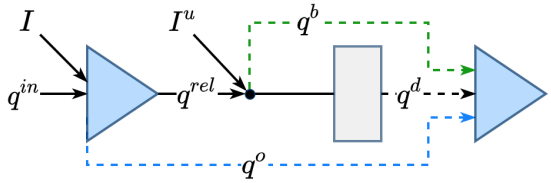

Fig. 1. A rotated illustration of the waterways between reservoirs together with regulated and unregulated natural inflow.

$$v_{m0} = V_m^0 \tag{15}$$

$$v_{m,h+1} - v_{m,h} = \frac{1}{4}\delta_h \mathbf{1}^T \cdot \mathbf{q}_{m,h}^{net} \tag{16}$$

$$\mathbf{0} \le v_{m,h}\mathbf{1} + \delta_h \mathbf{N}^T \cdot \mathbf{q}_{m,h}^{net} \le V_m \mathbf{1} \tag{17}$$

$$\mathbf{q}_{m,h}^{in} = \sum_{j \in \mathcal{J}_m^d} \sum_{n \in N_j} \mathbf{q}_{j,n,h}^d + \sum_{j \in \mathcal{J}_m^b} \mathbf{q}_{j,h}^b + \sum_{j \in \mathcal{J}_m^o} \mathbf{q}_{j,h}^o \tag{18}$$

$$\mathbf{q}_{m,h}^{net} = \mathbf{I}_{m,h} + \mathbf{q}_{m,h}^{in} - \mathbf{q}_{m,h}^{rel} - \mathbf{q}_{m,h}^o \tag{19}$$

$$\mathbf{q}_{m,h}^{rel} = \sum_{n \in N_m} \mathbf{q}_{m,n,h}^d + \mathbf{q}_{m,h}^b - \mathbf{I}_{m,h}^u \tag{20}$$

$$\mathbf{0} \le \mathbf{q}_{m,h}^b \le Q_m^b \cdot \mathbf{1} \tag{21}$$

$$\mathbf{0} \le \mathbf{q}_{m,h}^o \tag{22}$$

$$\mathbf{0} \le \mathbf{q}_{m,h}^{rel} \tag{23}$$

$$\mathbf{p}_{m,h} = \sum_{n \in N_m} \eta_{m,n} \mathbf{q}_{m,n,h}^d \tag{24}$$

$$Q^d_{m,n} w_{m,n,h} \mathbf{1} \leq \mathbf{q}^d_{m,n,h} \leq Q^d_{m,n} \mathbf{1} \quad (25)$$

$$\mathbf{q}^d_{m,n,h} \leq Q^d_{m,n} w_{m,n-1,h} \mathbf{1} \quad (26)$$

$$P^{min}_m z_{m,h} \mathbf{1} \leq \mathbf{p}_{m,h} \leq P^{max}_m z_{m,h} \mathbf{1} \quad (27)$$

$$SU_{m,h} - SD_{m,h} = z_{m,h+1} - z_{m,h} \quad (28)$$

$$SU_{m,h} - SD_{m,h} \leq 1 \quad (29)$$

$$z_{m,h}, SU_{m,h}, SD_{m,h} \in \{0,1\}. \quad (30)$$

v_{mh} is the instantaneous volume at the beginning of interval h for reservoir m, and constraint (15) sets the initial volume for each reservoir. Constraint (16) calculates the change in volume between two time intervals by integrating the net inflow, $q^{net}_m(t)$, over the entire time interval by the use of (7). Constraint (17) bounds the reservoir volume within the time interval, found by using property (6), between zero and the maximal reservoir volume V_m. Figure 1 shows that the waterways of the cascaded system is modelled by three separate routes: the spill gate, $q^o_m(t)$, the bypass gate, $q^b_m(t)$, and the discharge through each turbine segment $n \in \mathcal{N}_m$, $q^d_{m,n}(t)$. The hydropower topology constraints, expressed in (18) to (23), implement this system description. $I_m(t)$, $I^u_m(t)$ and $q^{net}_m(t)$ represents regulated and unregulated natural inflow, and net flow into the reservoir, respectively. $q^{in}_m(t)$ is the sum of the controlled flow into the reservoir from the upstream system, while $q^{rel}_m(t)$ is the total released flow out of the reservoir. Q^b_m denotes the maximal bypass flow. The constraints for hydropower production and commitment is expressed in (24) to (30), where $p_m(t)$ is the generated hydropower. The conversion from discharge through the turbine to generated power is a non-linear function depending on the plant head and the efficiency curves of the generator and the turbine. In (24), this non-linear function is approximated as a piece-wise linear curve, where each segment of the discharge variable has a constant efficiency η_n. As discussed in [11], binary variables $w_{m,n}(t)$ are necessary in the continuous-time formulation to ensure that the discharge segments are uploaded in physically correct order. Constraint (25) and (26) bound the flow through each discharge segment within an upper and lower limit with the use of the binary variable, and these two constraints are defined for all discharge segments $n \in \mathcal{N}_m$.

Constraint (27) to (30) expresses the hydropower unit commitment constraints, where $z_m(t)$, $SU_m(t)$ and $SD_m(t)$ are binary variables describing the commitment status, startup and shutdown of a hydropower unit m, respectively. From constraint (27), it can be seen that all the Bernstein coefficients in the decision variable $p_m(t)$ for a given hour are related to the commitment of the generator in that given hour. This forces the hydropower unit commitment decision to be constant during a time interval h, and will ensure that the production never is between zero and P^{min}_m. Unlike the smooth operation enforced on the thermal generators, discontinuous jumps in the hydropower production curve when there are startups and shutdowns are therefore permitted.

3) Wind Power and System constraints: Area and system wide constraints in the model are the following:

$$\mathbf{0} \leq \mathbf{s}_{a,h} \leq \mathbf{W}_{a,h} \quad (31)$$

$$\boldsymbol{\rho}^c_{a,h} = \mathbf{W}_{a,h} - \mathbf{s}_{a,h} \quad (32)$$

$$\alpha \geq \sum_{m \in \mathcal{M}} WV_{m,k} v_{m,N+1} + D_k \quad (33)$$

$$-F^{max}_l \mathbf{1} \leq \mathbf{f}_{l,h} \leq F^{max}_l \mathbf{1} \quad (34)$$

$$\sum_{m \in \mathcal{M}_a} \mathbf{p}_{m,h} + \sum_{i \in \mathcal{I}_a} \mathbf{g}_{i,h} + \mathbf{s}_{a,h} - \sum_{l \in \mathcal{L}} G_{l,a} \mathbf{f}_{l,h} = \mathbf{L}_{a,h} - \boldsymbol{\rho}^s_{a,h}. \quad (35)$$

Constraint (31) and (32) expresses the wind power generation $s_a(t)$ and the wind curtailment $\rho^c_a(t)$, respectively, where both constraints are defined over time intervals $h \in \mathcal{T}$ and areas $a \in \mathcal{A}$. Generated wind power is bound within zero and the maximal available wind power curve $W(t)$. The future expected operating cost for the system, α, which is directly added to the objective function in (37), is bounded by constraint (33), which are a set of linear Benders cuts $k \in \mathcal{K}$. The cut coefficients $WV_{m,k}$ and the cut constants D_k can be calculated by long-term hydrothermal models such as the one in [12], and the future expected system cost ultimately depends on the end volume of water in each reservoir. The power flow on the HVDC cables, $f_l(t)$, is bound by a maximal flow limit F^{max}_l in (34), defined for all lines $l \in \mathcal{L}$ over time intervals $h \in \mathcal{T}$. Constraint (35) shows the power balance, which needs to be satisfied for each area $a \in \mathcal{A}$ over time intervals $h \in \mathcal{T}$. $\mathcal{M}_a$ and $\mathcal{I}_a$ are the sets of hydropower and thermal units located in area a, and $G_{l,a}$ is the adjacency matrix of the HVDC grid. $L_a(t)$ is the area load and $\rho^s_a(t)$ is the amount of load shedding within each area.

4) Continuity constraints: One important aspect of the continuous-time optimization framework is that the value of the decision variable and its derivative can be continuous over time interval shifts. The continuity constraints in (3) and (4) are added to the optimization problem for the thermal production decision variable $\mathbf{g}_{i,h}$, the offshore wind production decision variable $\mathbf{s}_{a,h}$ and for the power flow decision variable $\mathbf{f}_{l,h}$ for all times $h \in \mathcal{T}$. This enforces C^1 continuity, meaning that the curves have continuous values and derivatives for all points in time. Less strict continuity constraints are added for the variables connected to the hydropower units $m \in \mathcal{M}$ over time intervals $h \in \mathcal{T}$, which is discussed in more detail in [11]. The C^0 continuity constraint in (3) is applied to the flow through the bypass gate and spill gate, $\mathbf{q}^b_{m,h}$ and $\mathbf{q}^o_{m,h}$. As there is need for discontinuous jumps in the hydropower production during startups and shutdowns, enforcing C^0 continuity on $\mathbf{p}_{m,h}$ will not be possible. Instead, constraint (3) is replaced with the inequality constraints in (36), which makes the hydropower production C^0 continuous over time interval changes except if a startup or shutdown occurs:

$$-P^{max}_m SU_{m,h} \leq \mathbf{p}^3_{m,h} - \mathbf{p}^0_{m,h+1} \leq P^{max}_m SD_{m,h}. \quad (36)$$

5) Objective function: The objective function for the proposed model, presented in (37), is to minimize the total cost of the system. The total cost includes the future expected cost of the hydro system, α, the cost of spilling and bypassing water, and the operational, startup and shutdown costs for the thermal generators. In addition, a negligible penalty for curtailment of wind power and a high penalty for load shedding are included in the last line. Both startup and shutdown costs for the hydropower plants and the wind farms are assumed to be negligible in this model.

$$
\begin{aligned}
Z = \alpha &+ \frac{1}{4} \sum_{m \in \mathcal{M}} \sum_{h \in \mathcal{T}} \delta_h \mathbf{1}^T \cdot \left(C^b \mathbf{q}^b_{m,h} + C^o \mathbf{q}^o_{m,h} \right) \\
&+ \sum_{i \in \mathcal{I}} \sum_{h \in \mathcal{T}} \left(\frac{1}{4} \delta_h C_i \mathbf{1}^T \cdot \mathbf{g}_{i,h} + C_i^{start} SU_{i,h} + C_i^{stop} SD_{i,h} \right) \\
&+ \frac{1}{4} \sum_{h \in \mathcal{T}} \delta_h \mathbf{1}^T \cdot \left(C^c \boldsymbol{\rho}^c_h + C^s \boldsymbol{\rho}^s_h \right) \qquad (37)
\end{aligned}
$$

III. Case Study

A case study of a stylized three-area system resembling Northern Europe is presented in this section. The continuous-time model presented in Section II and an analogous discrete-time model are both solved to compare how the different components in the system reacts when variable offshore wind power is integrated into the power system. Both models have been implemented in Pyomo and solved with CPLEX 12.10.

A. System topology and input data

The stylized three-area system contains a hydro dominated Norwegian area, a thermal dominated Central European area and an offshore wind area in the North Sea, connected through HVDC cables. The hydropower area is based on a real Norwegian cascaded system containing 12 reservoirs and plants with a total hydropower production capacity of 535 MW. A detailed description of the hydropower topology can be found in [13]. The ratio between the capacity of the cascaded system and the total installed capacity in Norway (32 257 MW at the beginning of 2019 [14]), here referred to as the system scaling rate, is used to scale the capacities for the rest of the generation units and cables in the three-area system. The installed capacity of the offshore wind area and the wind series used in the case study is based on wind data from Denmark, found in [15], and scaled to match the total offshore wind capacity provided by Denmark, Germany and the Netherlands in the North Sea. The wind farms in the offshore wind area are clustered together as one big wind farm, with a total installed capacity of 172 MW after it is scaled down with the system scaling rate. The thermal area contains 104 thermal generators, divided into five groups after the primary-fuel; fossil gas, fossil hard coal, lignite, nuclear and fossil oil generators. The ramping capabilities, installed capacity and marginal, startup, and shutdown costs are based on operating thermal generators in Germany and the Netherlands [16], [17]. The total capacity of the thermal area is 921 MW after scaling. The three-area system is connected through two HVDC cables, where the hydro and the thermal area are connected by a 63 MW cable and the offshore wind area and the thermal area are connected by a 172 MW cable. The capacity of the cable connecting the thermal and the hydro area is based on the total installed capacity of the interconnectors between Norway and mainland Europe today [18], [19], including the 1400 MW Nordlink cable, which will be installed during 2020 [20]. This results in 63 MW of transmission capacity after it is scaled down with the system scaling rate. The interconnector capacity between the thermal area and the offshore wind area is assumed to be equal to the installed capacity of the offshore wind area, to ensure no limitations on the utilization of the possible offshore wind power production. The time horizon is set to 24 hours, with hourly time intervals in the continuous-time model. The discrete-time model has quarterly time intervals but hourly commitment decisions. The case study is based on data from 22/4-2019 where the reservoir volume in Norway was at 31.6%, its lowest during 2019 [21]. Fig. 2 shows the wind series for the offshore wind area and the load profiles for the demand in the other areas. For the thermal area, it is assumed that the peak load is 85% of the installed capacity, which implies a peak load of 783 MW. The hydro area has a peak load of 400 MW which is 75% of the installed capacity. The load profiles are based on data from Nord Pool [22] and ENTSO-E [23]. The offshore wind area has a peak wind production of 163.54 MW, where the wind series is based on data from [15]. The continuous time load and wind series are calculated from the data by a least-squares error fit to the Bernstein polynomials. For the piece-wise constant load and wind series, the average quarterly values are used.

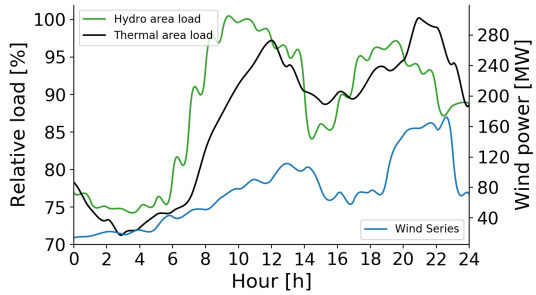

Fig. 2. The continuous-time load profiles of thermal and hydro areas scaled by the value of the peak load (left axis) together with the continuous-time wind power series for the offshore wind area (right axis).

B. Continuous-time and discrete-time model comparison

Both the discrete-time model and the continuous-time model are solved to optimality, meaning an absolute mip-gap of 0% was reached. The discrete-time model was solved within 80 sec., while the continuous-time model used 2 378 sec. to reach optimality on a single core 2.4 GHz machine. A breakdown of the objective function costs is listed in Table I.

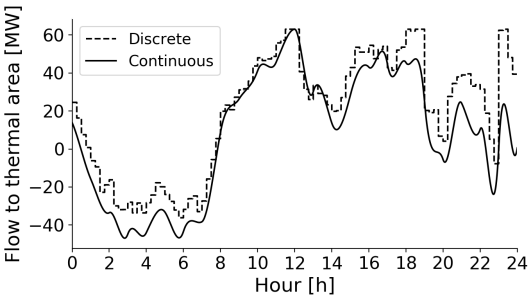

Fig. 3. Power flow on the HVDC cable from the hydro area to the thermal area.

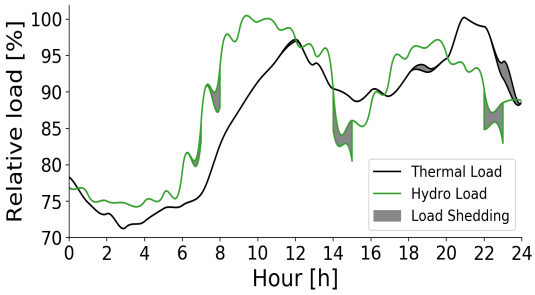

Fig. 4. Load shedding when the continuous-time model is solved with the fixed commitment solution from the discrete-time model.

For the thermal area, the discrete-time model schedules 51 generators to be committed during the whole optimization horizon. All fossil hard coal, lignite and nuclear generators are operating to cover the base load, while three fossil gas generators and zero oil-fired generators are committed. Six additional gas-fired generators are committed to meet the net-load variations in the continuous-time model. This result highlights that the continuous-time model sees the need to commit extra flexible units to cover sub-hourly net-load variations and peaks. This results in a 3.68% higher thermal cost and a 2.12% higher scheduled thermal production than in the discrete-time model. From Fig. 3 it can be seen that the power flow from the hydro area to the thermal area is higher for the discrete-time model during periods when the total load of the system is high, especially at the end of the scheduling period. This results in a 3.15% higher scheduled hydropower production and 2.15% higher hydropower related costs in the discrete-time model. Also note the rapid flow change in hour 23 in the discrete-time model caused by the drop in wind power production, which is not seen in the continuous-time solution. It is clear that such an abrupt change in flow is either infeasible or very costly when thermal generation and line flow continuity is enforced. The offshore wind power utilization is high entire scheduling period for both models, though a small amount of wind power is curtailed in the continuous-time model. Overall, the total cost of the system will be higher for the continuous-time model, with a 3 774.6 €/day (0.53%) increase compared to the discrete-time model.

TABLE I
COMPARISON OF THE TOTAL SYSTEM COSTS. ROW 3-5 REPRESENTS THE COST OF LINE 1-3 IN (37), RESPECTIVELY.

Cost	Discrete-time	Continuous-time
Objective value [€]	713 092.4	716 867.1
Hydro related costs [€]	388 795.7	380 623.0
Thermal related costs [€]	324 296.7	336 241.8
Curtailment and shedding costs [€]	0.0	2.3

C. Continuous-time simulator for real-time operation

To investigate where the discrete-time model overestimates the flexibility of the system, the continuous-time model is used as a simulator for real-time operation. The unit commitment decisions from the discrete-time model is used as input to the continuous-time model to identify in which periods the discrete-time model overestimates the system flexibility. From Fig. 4, it can be seen that the discrete-time model fails to commit enough units in periods when there are rapid changes in load and wind power. In these periods, an imbalance between the generated power and the actual load will occur, which will manifest as load shedding in the presented model. In total, 55 MWh load shedding will take place during the entire scheduling period, where the largest amount occurs in the hydropower area. This means that 0.22% of the total load will not be covered by the committed generators. In real system operations, the system operators need to activate reserves in these periods to balance the power system.

IV. Conclusion

We assess the structural imbalances in the interconnected North European power system by solving a continuous-time hydrothermal model with offshore wind power, and compare the results to an analogous discrete-time model. The increased cost of balancing the sub-hourly variations in the net-load was found to be 0.53% of the discrete-time model system costs per day. This cost increase is due to the overestimation of the system flexibility in the discrete-time model. The specific periods where the discrete-time model formulation overestimates the system flexibility were pinpointed by fixing the binary unit commitment decisions of the continuous-time model to be equal to the optimal discrete-time commitment solution. This resulted in a total of 55 MWh of load which could not be covered by the committed units and represents an additional requirement for fast system reserves that are not needed in the continuous-time solution.

V. Acknowledgments

This work was funded by the Research Council of Norway, Project No. 268014/E20.

REFERENCES

[1] "Offshore Wind Outlook 2019 – Analysis - IEA." [Online]. Available: https://www.iea.org/reports/offshore-wind-outlook-2019

[2] T. Aigner, S. Jaehnert, G. L. Doorman, and T. Gjengedal, "The effect of large-scale wind power on system balancing in Northern Europe," *IEEE Trans. Sustain. Energy*, vol. 3, no. 4, pp. 751–759, 2012.

[3] A. Helseth, A. Gjelsvik, B. Mo, and U. Linnet, "A model for optimal scheduling of hydro thermal systems including pumped-storage and wind power," *IET Gener. Transm. Distrib.*, vol. 7, no. 12, pp. 1426–1434, 2013.

[4] H. Farahmand, S. Jaehnert, T. Aigner, and D. Huertas-Hernando, "Nordic hydropower flexibility and transmission expansion to support integration of North European wind power," *Wind Energy*, vol. 18, no. 6, pp. 1075–1103, jun 2015.

[5] M. N. Hjelmeland, C. T. Larsen, M. Korpås, and A. Helseth, "Provision of rotating reserves from wind power in a hydro-dominated power system," in *2016 Int. Conf. Probabilistic Methods Appl. to Power Syst.* IEEE, oct 2016, pp. 1–7.

[6] B. P. Cotia, C. L. Borges, and A. L. Diniz, "Optimization of wind power generation to minimize operation costs in the daily scheduling of hydrothermal systems," *Int. J. Electr. Power Energy Syst.*, vol. 113, pp. 539–548, dec 2019.

[7] M. Parvania and A. Scaglione, "Unit Commitment With Continuous-Time Generation and Ramping Trajectory Models," *IEEE Trans. Power Syst.*, vol. 31, no. 4, pp. 3169–3178, jul 2016.

[8] R. Khatami, M. Parvania, and P. P. Khargonekar, "Scheduling and Pricing of Energy Generation and Storage in Power Systems," *IEEE Trans. Power Syst.*, vol. 33, no. 4, pp. 4308–4322, jul 2018.

[9] K. Hreinsson, B. Analui, and A. Scaglione, "Continuous Time Multi-Stage Stochastic Reserve and Unit Commitment," in *2018 Power Syst. Comput. Conf.* IEEE, jun 2018, pp. 1–7.

[10] R. Khatami, M. Parvania, and A. Narayan, "Flexibility Reserve in Power Systems: Definition and Stochastic Multi-Fidelity Optimization," *IEEE Trans. Smart Grid*, vol. 11, no. 1, pp. 644–654, jan 2020.

[11] C. Ø. Naversen, A. Helseth, B. Li, M. Parvania, H. Farahmand, and J. P. S. Catalão, "Hydrothermal Scheduling in the Continuous-Time Framework," dec 2019, accepted for publication in The Power Systems Computation Conference (PSCC) 2020. [Online]. Available: http://arxiv.org/abs/1912.06877

[12] A. Helseth, B. Mo, A. L. Henden, and G. Warland, "Detailed long-term hydro-thermal scheduling for expansion planning in the Nordic power system," *IET Gener. Transm. Distrib.*, vol. 12, no. 2, pp. 441–447, jan 2018.

[13] C. Ø. Naversen, H. Farahmand, and A. Helseth, "Accounting for reserve capacity activation when scheduling a hydropower dominated system," *Int. J. Electr. Power Energy Syst.*, vol. 119, p. 105864, jul 2020.

[14] Accessed 10/1-2019. [Online]. Available: https://www.nve.no/energiforsyning/kraftproduksjon/vannkraft/?ref=mainmenu

[15] Accessed 2/6-2019. [Online]. Available: https://www.energidataservice.dk/en/dataset/electricityprodex5minrealtime/resource_extract/06380963-b7c6-46b7-aec5-173d15e4648b

[16] Accessed 2/6-2019. [Online]. Available: https://www.eex-transparency.com/power/de/production/capacity/

[17] Accessed 2/6-2019. [Online]. Available: https://www.energy-charts.de/osm.htm

[18] Accessed 2/6-2019. [Online]. Available: https://www.nexans.no/eservice/Norway-en/navigatepub_142640_-34274/Royal_opening_of_Skagerrak_4.html

[19] J. Skog, K. Koreman, B. Pääjärvi, and T. Andersröd, "The NORNED HVDC cable link–a power transmission highway between norway and the netherlands," *ENERGEX 2006, Stavanger, Norway*, 01 2006.

[20] Accessed 2/6-2019. [Online]. Available: https://www.statnett.no/en/about-statnett/news-and-press-releases/News-archive-2018/norwegian-german-power-cable-being-installed/

[21] Accessed 3/3-2019. [Online]. Available: https://www.statnett.no/en/for-stakeholders-in-the-power-industry/data-from-the-power-system/#hydrological-data

[22] Accessed 2/6-2019. [Online]. Available: https://www.nordpoolgroup.com/Market-data1/Power-system-data/Consumption1/Consumption/NO/Hourly1/?view=table

[23] Accessed 2/6-2019. [Online]. Available: https://transparency.entsoe.eu/load-domain/r2/totalLoadR2/show

Appendix B

The table below presents the hydropower plant characteristics for all hydropower plants in the system. The values listed for discharge through the turbine, Q_n^d, and the energy conversion factor, η_n, are for each discharge segment, where the values are separated with a "/". Note that the different hydropower plants has different numbers of discharge segments.

Unit	$P^{max}\,[MW]$	$P^{min}\,[MW]$	$V^{max}\,[m^3]$
1	26.30	10.52	0.2
2	17.95	7.18	0.1
3	37.89	15.16	0.1
4	119.60	47.84	366.7
5	19.67	7.87	43.7
6	6.78	2.71	65.0
7	27.50	11.00	4.3
8	18.40	7.36	1.2
9	36.80	14.72	94.3
10	162.00	43.90	37.3
11	37.50	15.00	582.0
12	24.90	9.96	187.0

Unit	$Q^b\,[m^3/s]$	$Q_n^d\,[m^3/s]$	$\eta_n\,[MWs/m^3]$
1	10^4	52.0/8.0	0.47/0.21
2	10^4	72.59/8.06	0.22/0.22
3	10^4	88.79/9.86	0.39/0.37
4	10^4	40/20/10/10/10/10/5	1.26/1.24/1.12/1.07/0.98/0.9/0.74
5	10^4	11.34/1.26	1.57/1.52
6	10^4	6.97/0.77	0.88/0.86
7	10^4	42/5/3/15	0.55/0.4/0.33/0.1
8	10^4	50/10/10	0.28/0.23/0.23
9	10^4	12/8.4/1	1.76/1.69/1.5
10	10^4	13.3/12.7/10.6/8.3/6.1	3.3/3.26/3.18/2.77/3.28
11	10^4	85/7	0.42/0.24
12	10^4	24.8/3.1/3.1	0.83/0.77/0.58

Table B.1: Hydropower plants characteristics

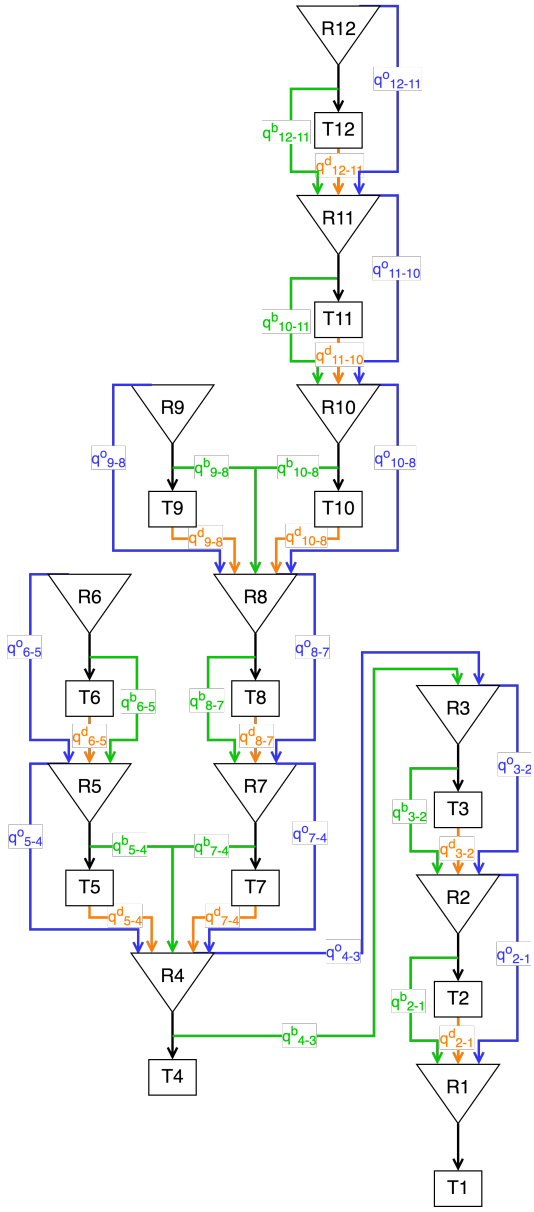

Figure B.1: Model of the cascaded hydro system with waterways between reservoirs. Blue lines are the spill gates, green lines are the bypass gates and the orange lines are discharge through the turbines.

Appendix C

The following table present the characteristics, as well as operational, start and stop costs, for all thermal generators used in the Case study. The thermal units are divided into five groups after primary fuel, where FG denotes Fossil gas, FHC denotes Fossil hard coal, L denote Lignite, N denote Nuclear and FO denote Fossil oil.

Type	Cost_start	Cost_stop	Cost	P_max	P_min	R_down	R_up
FG1	2190	2190	42.89	21.64	7.50	9.59	9.59
FG2	13370	13370	50.82	14.74	4.03	10.01	10.01
FG3	2719	2719	40.29	13.11	4.54	5.81	5.81
FG4	1773	1773	38.67	13.01	4.15	8.99	8.99
FG5	1924	1924	58.49	9.87	4.00	7.47	7.47
FG6	1708	1708	40.31	9.33	0.98	1.81	1.81
FG7	2712	2712	55.56	7.88	1.81	2.52	2.52
FG8	2190	2190	42.89	7.88	2.70	2.57	2.57
FG9	5529	5529	39.84	7.80	2.70	3.46	3.46
FG10	2190	2190	42.89	7.80	2.70	3.46	3.46
FG11	2190	2190	42.89	7.80	2.70	3.46	3.46
FG12	2190	2190	42.89	7.55	2.62	3.35	3.35
FG13	1741	1741	79.33	7.47	2.59	3.77	3.77
FG14	1652	1652	41.31	7.37	1.03	2.82	2.82
FG15	3024	3024	39.17	7.30	2.53	3.24	3.24
FG16	2190	2190	42.89	7.22	2.50	3.20	3.20
FG17	2190	2190	42.89	7.22	2.50	3.20	3.20
FG18	2190	2190	42.89	7.22	2.50	3.20	3.20
FG19	2554	2554	38.96	7.07	3.77	3.95	3.95
FG20	2190	2190	42.89	7.07	2.45	3.13	3.13
FG21	1773	1773	38.67	7.05	3.32	2.66	2.66
FG22	2190	2190	42.89	7.05	3.73	3.78	3.78
FG23	4072	4072	40.06	7.00	2.43	3.10	3.10
FG24	2190	2190	42.89	7.00	2.43	3.10	3.10
FG25	2190	2190	42.89	6.94	2.40	3.07	3.07
FG26	2167	2167	60.62	6.72	2.33	2.98	2.98
FG27	2197	2197	61.75	6.65	2.31	0.83	0.83
FG28	2182	2182	61.18	6.64	2.30	0.86	0.86
FG29	2190	2190	42.89	6.22	2.16	2.76	2.76
FG30	2190	2190	42.89	5.81	2.01	2.57	2.57
FG31	2610	2610	40.06	5.78	2.00	2.56	2.56
FG32	3607	3607	76.71	5.33	1.74	3.39	3.39
FG33	2190	2190	42.89	5.23	1.81	2.32	2.32
FG34	2190	2190	42.89	4.98	1.23	0.60	0.60
FG35	2756	2756	39.84	4.98	2.51	2.32	2.32
FG36	2190	2190	42.89	4.36	1.51	1.93	1.93
FG37	3024	3024	39.17	4.13	1.43	1.83	1.83
FG38	2190	2190	42.89	3.65	1.27	1.62	1.62
FG39	2190	2190	42.89	3.47	1.20	1.54	1.54
FG40	1633	1633	38.67	3.32	2.24	1.11	1.11
FG41	4726	4726	58.19	3.32	2.24	1.16	1.16
FG42	2190	2190	42.89	3.16	1.10	1.40	1.40
FG43	2190	2190	42.89	3.05	1.06	1.35	1.35
FG44	1368	1368	80.24	2.92	0.93	1.29	1.29
FG45	1970	1970	39.84	2.72	0.68	0.9	0.9
FG46	2190	2190	42.89	2.49	0.86	1.10	1.10
FG47	2190	2190	42.89	2.47	0.86	1.1	1.1
FG48	2190	2190	42.89	2.42	0.84	1.07	1.07
FG49	1555	1555	58.19	2.11	0.86	0.9	0.9
FG50	2190	2190	42.89	1.86	0.64	1.34	1.34
FG51	1698	1698	51.05	1.86	0.64	0.82	0.82
FG52	7572	7572	59.16	1.66	0.45	0.74	0.74
FG53	1444	1444	44.47	1.66	1.16	0.74	0.74
FHC1	9132	9132	32.45	26.22	6.14	10.60	10.60
FHC2	8302	8302	32.56	17.76	4.16	7.18	7.18
FHC3	8369	8369	32.56	17.46	4.09	7.06	7.06

FHC4	7576	7576	31.02	14.52	3.15	4.15	4.15
FHC5	9318	9318	32.67	13.28	2.99	5.99	5.99
FHC6	9318	9318	32.67	13.28	2.99	5.91	5.91
FHC7	7496	7496	31.48	13.11	2.16	6.64	6.64
FHC8	9191	9191	32.56	12.94	3.57	7.63	7.63
FHC9	7310	7310	32.34	12.56	2.85	5.06	5.06
FHC10	7849	7849	32.56	12.38	2.90	5.00	5.00
FHC11	7849	7849	32.56	12.05	2.82	2.99	2.99
FHC12	7821	7821	32.78	12.03	2.99	4.65	4.65
FHC13	7735	7735	32.46	11.87	2.41	4.65	4.65
FHC14	7868	7868	32.97	11.45	2.68	4.63	4.63
FHC15	7548	7548	35.93	11.45	3.98	4.25	4.25
FHC16	6937	6937	29.70	10.47	2.45	4.23	4.23
FHC17	6833	6833	30.80	9.36	2.19	3.78	3.78
FHC18	6864	6864	29.49	8.53	4.31	3.55	3.55
FHC19	7694	7694	34.62	7.63	1.66	1.66	1.66
FHC20	6951	6951	30.79	6.14	1.33	2.49	2.49
FHC21	7543	7543	36.07	5.81	1.99	3.32	3.32
FHC22	6641	6641	30.14	5.11	2.47	3.50	3.50
FHC23	7052	7052	32.97	4.98	1.49	2.01	2.01
FHC24	6910	6910	31.48	4.60	1.00	1.03	1.03
FHC25	6609	6609	28.69	4.51	1.94	1.01	1.01
FHC26	6810	6810	31.02	4.15	1.00	1.85	1.85
FHC27	6699	6699	31.74	2.04	0.48	0.82	0.82
FHC28	6601	6601	30.55	2.04	0.48	0.82	0.82
L1	46402	46402	25.43	35.18	15.93	7.80	7.80
L2	10690	10690	14.74	20.05	8.93	4.44	4.44
L3	12254	12254	13.95	16.59	4.65	4.69	4.69
L4	11597	11597	13.29	16.59	4.81	4.69	4.69
L5	10566	10566	12.34	15.35	6.14	3.57	3.57
L6	8651	8651	12.56	14.94	6.14	7.67	7.67
L7	9783	9783	12.42	12.53	4.31	3.50	3.50
L8	9705	9705	12.33	12.53	4.31	3.50	3.50
L9	9088	9088	16.21	10.95	4.48	2.27	2.27
L10	8985	8985	15.91	10.95	4.15	2.27	2.27
L11	7955	7955	17.57	10.65	3.15	2.21	2.21
L12	10795	10795	14.93	10.62	4.65	2.47	2.47
L13	10795	10795	14.93	10.45	4.65	2.43	2.43
L14	8963	8963	15.84	9.96	3.58	2.31	2.31
L15	8616	8616	15.13	9.69	4.60	2.15	2.15
L16	7199	7199	12.52	2.49	1.00	0.58	0.58
N1	12000	12000	9.03	23.40	2.61	4.93	4.93
N2	12000	12000	9.03	22.57	6.14	6.14	6.14
N3	12000	12000	8.64	22.17	6.64	8.13	8.13
N4	12000	12000	9.03	8.05	2.19	2.19	2.19
FO1	9022	9022	52.45	3.88	2.41	3.88	3.88
FO2	4819	4819	52.45	2.07	1.29	2.07	2.07
FO3	3323	3323	52.45	1.43	0.89	1.43	1.43

Mari Lund Øvstebø

The Impact of Offshore Wind Power Variations on Continuous-time Scheduling of a Hydrothermal System

NTNU
Norwegian University of
Science and Technology